2015

Investigating the Photorecombination Dynamics in Molecular High-Harmonic Spectra

Benjamin Parker Wilson
Louisiana State University and Agricultural and Mechanical College

INVESTIGATING THE PHOTORECOMBINATION DYNAMICS IN MOLECULAR HIGH HARMONIC SPECTRA

A Dissertation

Submitted to the Graduate Faculty of the
Louisiana State University and
Agricultural and Mechanical College
in partial fulfillment of the
requirements for the degree of
Doctor of Philosophy

in

The Department of Chemistry

by
Benjamin Parker Wilson
B.S. Abilene Christian University, 2008
May 2015

Acknowledgements

There are many people I owe thanks to for help in completing this task: firstly, Erwin Poliakoff, for his guidance and assistance in conducting this work; Carlos Trallero, our collaborator at Kansas State for his patience and instruction in the lab; my family and friends for their support and encouragement; and most of all Abby, for her love and support.

Table of Contents

Abstract

The work presented in this dissertation will relate the photorecombination dynamics to photoionization dynamics in SF_6 utilizing the self-probing mechanism, high harmonic generation (HHG). This work specifically aims to establish parameters for which the comparison is applicable and the macroscopic complications inherent in HHG do not interfere with the extraction of dynamic information. The first part of this work established the macroscopic experimental apparatus necessary for consistent spectroscopic observation. It is shown that using a gas jet that is an order of magnitude shorter than the Rayleigh length of the driving laser results in more consistent harmonic spatial profiles and location of spectroscopic features. The observation of photorecombination dynamic in HHG is extended to shape resonances in SF_6 with a focus on separating the effects of phase matching from photorecombination. This is accomplished by varying the laser parameters including the location of the focal point with respect to the center of the gas jet and altering the strength of the electric field. This process allowed us to observe two high energy shape resonances in the HHG spectrum of SF_6 and map the appropriate parameters at which our experimental results confirm theoretical calculations based on the quantitative rescattering theory conducted by collaborators at Texas A&M University. The shape resonance was then probed by adding ellipticity to the fundamental in order to determine if there was information related to the angular dependence of the shape resonance that could be extracted in a way unique to HHG.

Chapter 1: Background and Significance

This dissertation will examine the photorecombination dynamics of polyatomic molecules with high harmonic generation (HHG). Photorecombination can be described as the inverse of photoionization. Photoionization occurs when an atom or molecule absorbs enough energy from a high energy light source for an electron to be ejected:

$$\mathrm{M}+\mathrm{h}\nu \rightarrow \mathrm{M}^{+}+e^{-}$$

Photorecombination, then, is described as the ejection of a high energy photon when an electron with kinetic energy above the ionization energy of a molecule collides with the ion:

$$\mathrm{M}^{+}+e^{-} \rightarrow \mathrm{M}+\mathrm{h}\nu$$

Each process reveals information about the molecule or atom involved by measuring the energy and yield of the resulting electron or photon.

This relationship implies that the dipole matrix elements present in photoionization are shared in photorecombination and that dynamics expressed in the photoionization cross section are present in the photorecombination cross section. We utilized high harmonic generation (HHG)[1,2], the product of the recombination cross section and electron wave packet[3], as a self-probing mechanism to examine recombination dynamics and their relationship to photoionization dynamics previously studied by photoelectron spectroscopy. Much of the present work involves the decoupling of the electron wave packet from the recombination cross section.

Section 1.1 serves as an overview of the three step process responsible for HHG: tunnel ionization, electron acceleration, and recombination. Section 1.2 will address the phase

matching properties resulting from macroscopic propagation, specifically the effects of the focus position of the laser relative to the center of the gas jet and the intensity of the laser. Section 1.3 provides an overview of the theoretical background utilized for calculating HHG spectra that supports the presented results. Section 1.4 will discuss the foundation of the spectroscopic information probed in this paper including the relevant PES literature and examples of the features in HHG.

1.1 High Harmonic Generation

High harmonic generation (HHG) has received a remarkable amount of attention in the scientific community due to its unique, ultrafast timescale, and angstrom spatial resolution mapping of wavepackets and orbitals[4,5] . The result of this process is a series of energetically narrow high energy photons (shown in Figure 1.1) in a relatively small physical space, leading to

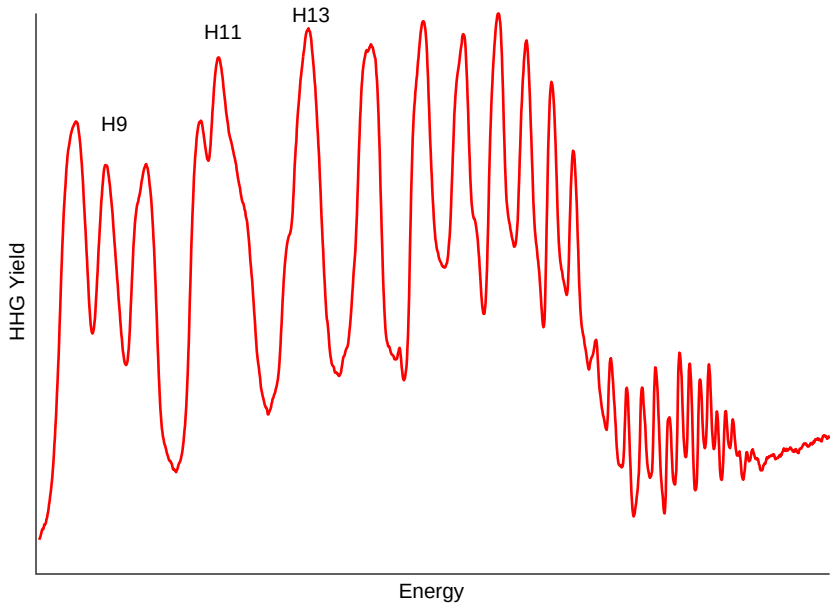

Figure 1.1: A sample HHG spectrum of Ar. The energy increases from left to right, beginning at the ninth harmonic of the fundamental.

the informal title of “table-top synchrotron.” It can be described as the following three step process: first, an atom or molecule undergoes tunnel ionization which frees an electron wave packet; second, the wave packet is accelerated away from the ion and driven back by the laser pulse; third, recollision of the electron wave packet with the parent ion results in the release of a high energy photon[1,2]. This is referred to as the semi-classical model because the motion of the electron in the electric field is considered classically. The photons produced are odd ordered harmonics of the fundamental laser used to initiate the process. The resulting mixture of harmonics spans a very broad range of radiation produced in attosecond bursts. An overview of the three step process is presented in Figure 1.2, while a detailed description of each step follows in this section.

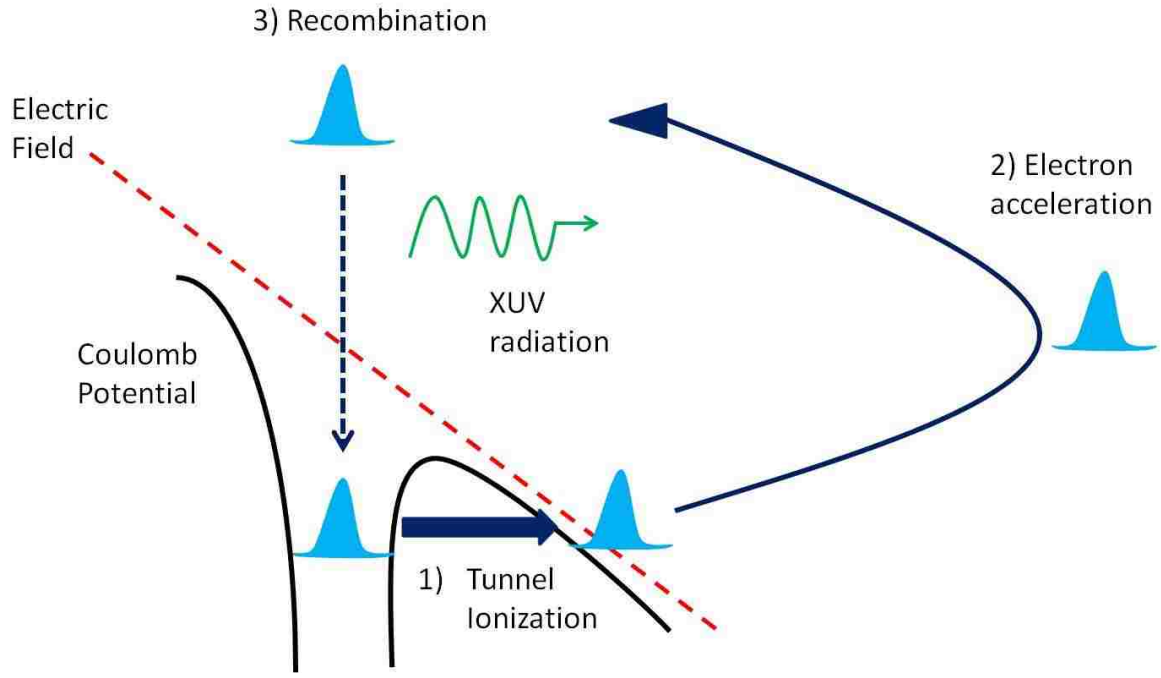

Figure 1.2: A simplistic visual representation of the three step model of HHG.

1.1.1 Tunnel ionization

The first step in HHG is strong field ionization. Strong field ionization occurs when a radiation source of sufficient energy and intensity reacts with an atom or molecule to cause the ejection of an electron. The Keldysh theory of strong field ionization describes two primary ionization processes: multiphoton ionization and tunnel ionization [6]. Multiphoton ionization depends on the sequential addition of photons to a high enough energy to overcome the ionization energy of the atom or molecule. For example, a photon from an 800 nm source has an energy of approximately 1.55 eV, and thus the ionization of argon (I_p ≈15.7 eV[7]) requires 10 photons. Tunnel ionization, by contrast, occurs when a sufficiently strong electric field distorts the coulomb potential (shown in Figure 1.2) of the atom or molecule at which point an electron is statistically likely to tunnel through the barrier. The probability of tunneling occurring opposed to multiphoton ionization is described by the Keldysh parameter[6] (1-1) , which establishes a relationship between the characteristics of the laser and the ionization energy of the target atom or molecule.

$$\gamma = \sqrt{I_p / 2U_p} \qquad (1\text{-}1)$$

In which I_p is the ionization energy of the target and U_p is the ponderomotive energy of the laser system, also referred to as the quiver energy. This value represents the average kinetic energy acquired by an electron in the electric field and is described in atomic units as:

$$U_p = \frac{I}{4\omega^2} \qquad (1\text{-}2)$$

In which I is the peak intensity of the electric field, given in units of $3.5*10^{16}$ W/cm^2, and ω is the angular frequency of the laser. When the parameter in equation (1-1) is less than 1,

tunneling ionization is preferred, while values greater than 1 are indicative of conditions favoring multiphoton ionization. A graphical depiction of the coulomb distortion at multiple electric field amplitudes is presented in Figure 1.3. It is apparent from the figure that at high enough electric field amplitudes, the potential is distorted to the extent that over the barrier ionization is favored in lieu of tunneling.

The instantaneous intensity of the laser, $I = E/(\tau \cdot r)$, is dependent on the energy of the laser, E, the pulse duration, τ, and the spot size r. Thus if the duration of the pulse is too long the ponderomotive energy will be too high to favor tunneling and multiphoton ionization will be favored. Likewise, if the wavelength is too short, multiphoton ionization will become more favorable. A laser system that has a sufficiently long wavelength, usually in the infrared, with very short, intense, laser pulses is needed to ensure the prevalence of tunnel ionization. In

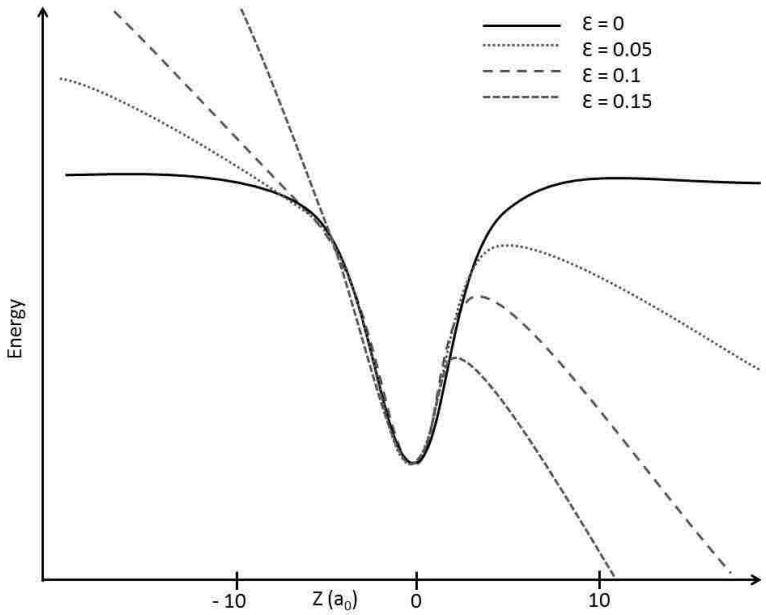

Figure 1.3: A visual representation of the effect of a strong electric field of the coulomb potential of the ground state atom or molecule. The Ɛ values represent the strength of the electric field in atomic units. Adapted from [8]

order for this to be achieved, Ti:Sapphire lasers that have a central wavelength near 800 nm with approximately 30 fs pulse durations are typically used.

1.1.2 Electron acceleration

After the electron tunnels through the barrier, it is steered by the electric field of the laser and initially has zero kinetic energy in the direction of the oscillating electric field. At this point, classical approximations are utilized in determining the path of the electron. This discussion of the electron acceleration in HHG is based on information contained in[1,2], with supplemental information from [9]. The electron is initially swept away from the ion by the field, and then at the turning point driven back in the direction of the ion. The maximum kinetic energy that can be obtained in this process is defined by the ponderomotive energy of the laser (1-2), which can be better expressed as a function of the electron charge, e, mass, m, and the amplitude of the electric field, E_0 as:

$$U_p = \frac{e^2 E_0^{\,2}}{4m\omega^2} \quad (1\text{-}3)$$

This represents the maximum oscillation of an electron in the electric field, $E = E_0 \cos(\omega t)$. The following discussion is simplified by using atomic units such that e, m and $\hbar$ are equal to one. The real acceleration in the field will depend on the temporal period during which the electron is affected by the electric field. Determining the final velocity of the electron begins by describing the position equation of an electron in an electric field as:

$$x(t) = \left[v_0 + \frac{E_0}{\omega}\sin(\phi_0) \right] \frac{(\phi_f - \phi_0)}{\omega} + \frac{E_0}{\omega^2}\left[\cos(\phi_f) - \cos(\phi_0) \right] \quad (1\text{-}4)$$

This equation introduces a new term, ϕ, that represents the phase of the laser as it oscillates. The electron is assumed to have zero kinetic energy in the direction of acceleration after tunneling through the barrier, eliminating v_0 from the proceeding equation. The equation for the final velocity then becomes:

$$v(t) = \frac{E_0}{\omega}[\sin(\phi_0) - \sin(\phi_f)] \quad (1\text{-}5)$$

From this, the maximum velocity experienced by the electron can be expressed as:

$$v_{\max} = 2\frac{E_0}{\omega} \quad (1\text{-}6)$$

This value results in a maximum kinetic energy, in atomic units, of $2\frac{E_0^2}{\omega^2}$. This is closely related to the atomic unit value of the ponderomotive energy given in (1-2) such that the maximum energy can be expressed simply as $8U_p$. This maximum energy requires an initial phase of $\pi/2$, a condition only met when the amplitude of the electric field is 0, eliminating the possibility of tunnel ionization. Thus, the maximum kinetic energy of the electron is closer to $3U_p$.

The electron can only recombine if it returns to a region spatially close to the ion it departed from. Thus, in order to determine the possible recombination trajectories for HHG, the position equation for an electron in a strong electric field is solved for “saddle points”, or zero point solutions. The nature of the equation results in an infinite number of solutions that differ by an integer of π. Due to quantum diffusion, only the first two solutions are considered probable and are labeled as short and long trajectories, respectively. An approximation of their paths in the electric field is shown in Figure 1.4. It is important to note that the two solutions result in identical electron kinetic energies and contribute to the same harmonic emission.

It is possible to differentiate the long and short trajectories based on the observable properties, a reflection of the differing phases each trajectory acquires during the acceleration step. This acquired phase is related to the transition dipole matrix that relates the continuum state in the electric field and the ground state of the atom or molecule and is termed the dipole phase [10]. The phase difference between the trajectories was initially described by Bellini *et al.*[11] The dipole phase of long trajectories varies significantly with laser intensity and impacts the phase front of the electron wave packet. This is especially applicable since the gas medium will experience fluctuations in laser intensity within an optical cycle, a fact referenced earlier by the presence of varying ionization times within the laser cycle. This variation of the dipole phase results in a "chirped" harmonic emission that has a small coherence time and a divergent angular emission[12], giving rise to the stretched and distorted appearance of the harmonics on the position sensitive detector. The dipole phase of short trajectories is independent of laser

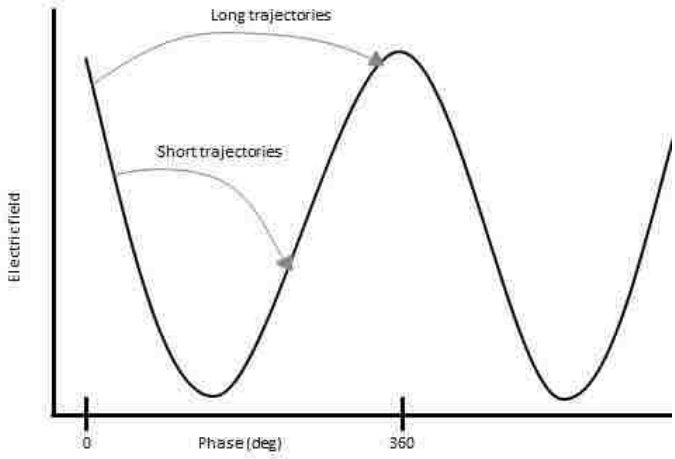

Figure 1.4: A figure displaying the two electron trajectories that contribute to HHG. They each begin in the first quarter of the laser cycle; however, their respective paths depend on the specific time the tunneling occurs. This process repeats every half-cycle of the laser. This figure is adapted from [10].

intensity because these paths are shorter than half of an optical cycle. This results in the resulting harmonics from this contribution having a large coherence time and an annular spatial profile.

1.1.3 Recombination

The final step in HHG refers to the recombination of the electron with the parent ion, which results in the release of a high energy photon equivalent to the sum of the ionization energy of the ground state of the ion and the kinetic energy gained by the electron in the electric field. Due to the limits on electron acceleration explained in the previous section, the maximum energy of the emitted photon is approximately $I_p + 3U_p$, in which I_p is the ionization energy of the orbital the electron originated in and recombines to. The quantization of energy dictates that the only permitted energies emitted are multiples, or harmonics, of the fundamental. Due to inversion symmetry in the target atom or molecule and the symmetry in the optical cycle, the even ordered harmonics are cancelled out leaving just odd ordered harmonics. The symmetry of the laser can be broken by overlapping two different wavelengths [13-15] and the inversion symmetry can be broken by orienting the molecule[16]. Either of these processes results in even and odd ordered harmonics.

The development of the harmonic spectra proceeds such that the intensity of the harmonics reaches a maximum near the ionization energy of the target atom or molecule before a sharp decline to a “plateau” region. In this region, the intensities of the individual harmonics decay slowly, appearing almost level when plotted on a log scale. The final few harmonics before the cutoff is reached are referred to as “cutoff” harmonics and feature a very sharp decline in intensity from the plateau region. The first two regions of the spectrum contain

both long and short trajectory contributions while complications related to the cutoff harmonics preclude contributions from the short trajectories in the third region.

This effect can be explained by considering the ionization times of the differing trajectories. Long contributions begin when the electric field is near is peak, whereas short trajectories begin closer to the minimum. When the electric field is near its peak, the coulomb potential is suppressed to a greater extent than when it is low. The strength of the potential barrier is thus inversely proportional to the strength of the electric field when tunneling begins. Thus for long trajectories, which begin early in the optical cycle, the imaginary part of the contribution is small. As the harmonic order increases into the cutoff region, there are no real saddle point solutions and the imaginary part becomes positive[17], this results in contributions to this harmonic region coming exclusively from the long trajectories due to the decreased influence of tunneling time. Trajectory contributions in this third region are sometimes referred to as extreme trajectories because neither of the typical profiles associated with long and short trajectories adequately describe the cutoff harmonics in a full quantum mechanical treatment [18].

1.2 Macroscopic Propagation Effects

1.2.1 Phase matching overview

HHG does not occur as the result of XUV dipole radiation from a single target, but is rather a collimation of signal from many atoms or molecules in the medium. The measured XUV radiation is then the result of constructive interference as the fundamental beam propagates through the medium. In order for this coherent process to occur, the phase of a generated harmonic at some point in the medium must match the phase of the harmonic generated at an

earlier linear point in the medium. The generated phase, however, is dependent on the phase of the source which changes rapidly as the laser is focused and then defocused. For this reason, an understanding of the atomic or molecular response in HHG, as outlined in section 1.1, is insufficient to describe the resultant HHG spectrum. A thorough understanding of the phase matching effects is necessary to interpret the results of HHG.

There are two phases that need to be addressed: the focusing phase of the laser and the dipole phase of the XUV radiation. The dipole phase of each harmonic changes as a function of the semiclassical movement of the electron that contributes to its generation. It is important to note that this is separate from the dipole recombination matrix that is responsible for the relative intensity of the third step in the HHG process. The phase can thus be described as function of the electron trajectory[19,20]:

$$\phi(t_i, t_f) = -\int_{t_i}^{t_f} S(t)dt\,, \qquad (1\text{-}7)$$

in which

$$S(t) = KE(t) - V(t) \qquad (1\text{-}8)$$

Or the difference between the kinetic energy and the potential energy of the electron as it is accelerated. The kinetic energy of the electron is approximately equal to the quotient of the ponderomotive energy to the return energy with the phase of each specific trajectory factored in as a proportionality constant, α.

Multiple saddle point solutions exist for each kinetic energy value contributing to the harmonic sum that are differentiated by their respective phase. Gaarde *et al.* [20] plotted this value versus ponderomotive energy using saddle point solutions, an adapted version of their published findings is presented in Figure 1.5. These solutions demonstrate that the highest

energy photons have the most similar phase between the two quantum paths and the phase increases as the path duration increases.

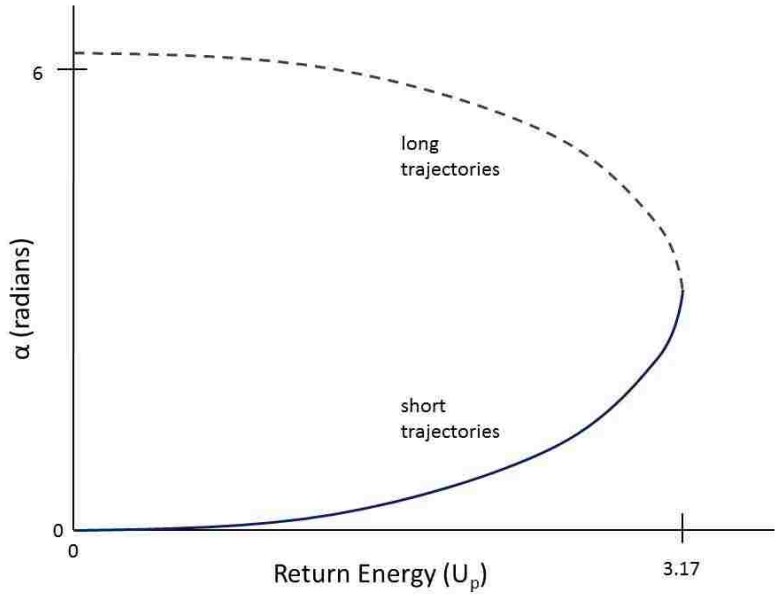

Figure 1.5: A plot of the atomic dipole phase as a function of the return energy. This plot was reproduced from results in [20].

The phase of XUV field contributions at different points in the medium for the same harmonic must match in order for constructive interference to occur. In addition to this phase matching requirement, the phase of the XUV electric field needs to match the phase of the source electric field. A necessary condition for this process is the conservation of momentum, expressed in terms of the wavevector of the emitted harmonic, $\vec{k}_q$, the wavevector of the fundamental, $\vec{k}_1$, and effective wavevector from the dipole phase, $\vec{K}$, as[21]:

$$\vec{k}_q = q\vec{k}_1 + \vec{K} \quad (1\text{-}9)$$

The source phase changes rapidly as it approaches the focus point, a condition necessary for the intensities required in HHG. This phase, known as the Gouy phase in the on-axis region, is a

function of the distance from the axis of polarization, r , the distance from the focus, z , the confocal parameter of the beam, b , and the length of the wavevector, k :

$$\phi_{focus}(r,z) = -\tan^{-1}\left(\frac{2z}{b}\right) + \frac{2kr^2 z}{b^2 + 4z^2} \quad \text{(1-10)}$$

Thus for small changes in the parameter of the laser, the Gouy phase can change rapidly and alter the phase matching with the resultant harmonics. The condition described in (1-9) is thus more accurately expressed as the change in phase:

$$\Delta\vec{k} = \vec{k}_q - (q\vec{k}_1 + \vec{K}) \approx 0 \qquad \text{(1-11)}$$

The remainder of this dissertation will describe conditions under which the previous equation is approximately true as good phase matching. The following two sections will examine two variables with respect to the laser that impact HHG: focus position and intensity.

1.2.2 Focus position dependence

The overall harmonic yield changes as a function of lens position due to the constructive interference between the Gouy phase of the fundamental and the dipole phase of the resultant harmonics[12]. While the ionization rate changes in proportion to the change in gas density as the focus of the laser moves through the gas jet, peaking when the focus is centered in the medium, the HHG yield has two distinct humps on either side of the gas jet[12]. Early studies used a supersonic pulsed gas jet and determined that the phase matching complications resulted in two peaks in HHG to occur when the focus is positioned 3 mm before the center of the gas jet and 1 mm after, with the former having the optimal phase matching and highest overall harmonic yield.

The axial phase of the fundamental varies rapidly as the beam goes into and out of focus such that the Gouy phase is very different on either side of the focus, even at equal distances. This variance affects the direction at which harmonics are emitted at different positions of the focus with respect to the medium[19]. When the focus is placed in the center of the medium, the variances from the converging and diverging parts of the beam are essentially cancelled out and even though poor phase matching prevents intense harmonic output, the harmonics that are emitted are typically emitted on-axis with the principle beam[19,22]. Studies determining the contributions from other positions of the focus point have been limited to positions from (-) 3 mm to (+) 3 mm, and some contradiction in results exists. Away from the center of the jet, some groups have found that off-axis contributions are favored at (-) positions while on-axis contributions are favored in the center of the jet and at (+) positions[19], while others have come to the opposite conclusion[23].

The off-axis contributions are more divergent than the on-axis contributions due to changing emission directions which results in a scattered far field profile while the on-axis contributions result in a bright annular ring[19]. This description is remarkably similar to the description of long and short quantum paths by Bellini *et al.*[11], and thus it is common to assume that the long trajectories result from off-axis contributions and short trajectories derive from on-axis contributions[22,24] This is not a definitive assignment, however, as one study suggests that both on and off-axis contributions at (-) 0.5 mm result in similar far field profiles[24]. However, long trajectories remain primarily associated with off-axis emission and allow for polarization gating to emphasize one trajectory over the other. In addition to polarization gating, the phase matching conditions can be altered to favor one trajectory over

another. The two paths have differing harmonic phases and as such react differently to the laser as the focus point is moved with respect to the gas jet. This selection rule has been utilized previously by several groups to filter out long trajectories by placing the focus point 2 mm in front of the medium[25-27].

1.2.3 Intensity dependence

The second variable that impacts the phase matching properties of harmonic generation is the peak intensity of the laser. Changes in this intensity not only alter the tunnel ionization step in HHG, but the phase of the laser is also affected. Thus the phase of the emitted radiation is inversely proportional to the intensity of the laser such that for the two contributing quantum paths, $i=1,2$, the phase of the harmonic from a specific trajectory can be described as [28]:

$$\phi_i(r,z,t) = -\alpha_i I(r,z,t) \qquad (1\text{-}12)$$

The α_i term is the slope of the phase. The summation of the phases from $i=1,2$ is representative of the total phase of the specific harmonic.

The harmonic phase and the intensity are each a function of a spatial and temporal component, each of which add a complication to the harmonic output. The time dependence of the laser intensity results in a slight change in the instantaneous frequency, defined as a chirp in the pulse[28], which due to phase differences, impacts the long and short trajectories differently. The spectral widths of long trajectories are mainly determined by the spreading of the wave packet in the electric field, termed the dipole chirp, while the contributions from τ_1 are independent of the chirp. This dependence corresponds to a rapid linear phase variation

with intensity from long trajectories and a slow linear phase variation with intensity from short trajectories.

The radial variation of the intensity, $I(r)$, induces a curvature of the phase front that results in a strong angular divergence of the emitted harmonics for contributions with large α or large I [29]. This angular divergence is the source of the spatial divergence evident in the long trajectories that it utilized to visually separate them from the short trajectories, a difference that becomes more important to the total phase as the intensity is increased. The optical intensity for harmonic generation changes slightly as the position of the focus point is moved with respect to the medium, but is always approximately equal to the transition of the dipole plateau harmonics to the cutoff harmonics.

The phase of the laser changes faster in close proximity to the focus; as a result, the dipole phase varies slower with intensity when the focus is outside of the range of (-) 3 to (+) 3 mm[29]. Determining the intensity dependence of the phase becomes complicated when considering the influence of the lens position. The intensity dependence can be approximated by determining the slope of the mean phase when both quantum paths contribute to the overall harmonic yield; however, since the slope of the phase resulting from the shorter quantum path is much weaker than the total phase, the slope of the phase at lens positions where the short contribution is highly favored is not representative of the total phase slope. In contrast, the slope of the phase relative to the long trajectories matches the trend of the total phase, thus the intensity dependence of harmonics can be determined at positions favoring long trajectories.

The different response to changes in intensity by different trajectories implies that portions of the harmonic spectrum that are comprised mainly of one trajectory or another will respond differently to those changes. Cutoff harmonics, for example, are comprised solely of long trajectories and thus have a strong intensity dependent phase. Likewise, plateau harmonics, though comprised of both long and short trajectories, have stronger total contributions from the longer path and also have an intensity dependent phase. Below threshold harmonics, however, are a result of multiphoton process due to the necessary negative return energy of their origin[30], and thus have a phase independent of intensity.

1.3 Theoretical Background

1.3.1 Single active electron approximation

In order to solve the time dependent Schrödinger equation (TDSE) for an atom or molecule in a strong electric field, approximations to simplify the calculation are made. The first of these is commonly referred to as the single active electron approximation (SAE) [31]. In this model, the electron ejected from the parent atom or molecule is treated as the only electron in the ion perturbed by the electric field.

This approximation results in a linear Schrödinger equation and neglects the effects of possible electron-hole dynamics and multiple excitations. The TDSE for an atom in the strong electric field is given by:

$$i\left|\Psi(\mathrm{x},t)\right\rangle = \left[-\frac{1}{2}\nabla^2 + V(\mathrm{x}) - E\cos(t)x\right]\left|\Psi(\mathrm{x},t)\right\rangle \qquad (1\text{-}13)$$

Integration of (1-13) results in the time dependent dipole moment that can be numerically solved. This has been expanded to include the quantum treatment of HHG[1] because the dipole moment is related to the intensity of the HHG emission. In this application, the harmonic generation from an atom or molecule is assumed to be the result of a single excited electron within the target. This is, essentially, the basis for the three step model of HHG. A further example of the use of this with respect to HHG is the calculation of the intensity dependent dipole moment.

1.3.2 Strong field approximation

The significant drawback to the numerical calculations of the TDSE is the computational cost for the full integration. This is partially corrected by the introduction of another fully quantum treatment of HHG, referred to as the Lewenstein model, or the strong field approximation (SFA)[32]. As an expansion on the SAE, the SFA approximates that the only relevant contribution to HHG is the ground state, the depletion of the ground state can be neglected, and the electron behaves as a free particle in the electric field with no effect from the coulomb potential. The last assumption is only true with a sufficiently strong electric field, which is the source of the name for this theoretical model. Now that the discussion is a full quantum treatment of HHG, the description of an electron being accelerated in the electric field will shift in terminology to an electron wavepacket that undergoes dipole acceleration in a continuum state with a calculable probability of recombination.

Within the SFA, the momentum and time dependent continuum wavefunction can be expressed as:

$$\Psi_c(\vec{k},t') = \int d^3k \int_{-\infty}^{t} dt' e^{-i\Phi(\vec{k},t')} e^{-i\vec{k}\vec{r}} \chi(\vec{k},t') \qquad (1\text{-}14)$$

which contains a momentum and time dependent phase, $\Phi(\vec{k},t')$, and a release wavefunction, $\chi(\vec{k},t')$. The release wavefunction accurately describes the trajectory of the electron in the electric field and is a function of the momentum, which is dependent on the ionization energy of the target relative to the strength of the electric field. The time dependent dipole moment, assuming the continuum-continuum contributions are negligible, is:

$$d_{SFA}(t) = 2\,\mathrm{Re}\left\langle \Psi_c \left| \vec{r} \right| \Psi_0 \right\rangle \qquad (1\text{-}15)$$

The calculations based on these assumptions is somewhat clarified in [33], which is used as an additional reference for the remainder of the discussion of the SFA.

The expanded version of the time dependent dipole, with all of the relevant terms, is:

$$d(t) = -i\int_0^{t_f} dt_i \int d^3p\, d_{\mathrm{rec}}[k] \exp[iS(k,t_i,t_f)] \times d_{\mathrm{ion}}[k,t_i] + \mathrm{c.c.} \quad (1\text{-}16)$$

This introduce four new terms: the drift momentum, p, the dipole recombination amplitude, $d_{\mathrm{rec}}[k]$, the dipole ionization amplitude, $d_{\mathrm{ion}}[k,t_i]$, and a function of the classical motion of the electron wavepacket in the electric field, $S(k,t_i,t_f)$. The last of which can be expressed as a function of the ionization energy and electron wave packet momentum:

$$S(k,t_i,t_f) = -\int_{t_i}^{t_f} dt'' \left[\frac{k^2}{2} + I_p \right] \qquad (1\text{-}17)$$

The harmonic spectrum is then calculated by taking the Fourier transform of the time dependent dipole moment for each harmonic contribution. The power spectrum, then, takes the form:

$$P(\omega) = -i\int dt \int_0^{t_f} dt_i \int d^3p\, d_{\mathrm{rec}}[k] \times \exp[i\omega t + iS(k,t_i,t_f)] d_{\mathrm{ion}}[k,t_i] \quad (1\text{-}18)$$

This method successfully reproduces harmonic spectra for atoms and small molecules in the upper plateau and cutoff energy regions, while it is less accurate in the lower plateau region. Equation (1-18) still requires the use of costly saddle-point calculations and neglects the effect of macroscopic properties on the total harmonic spectrum.

1.3.3 Quantitative rescattering theory

This section will provide an overview of the theoretical support for the present work. Specifically, the connection between recombination dynamics and the high harmonic spectra must be established within the context of the phase matching properties described in the previous section. The computational details are outside the scope of this paper and will not be discussed; rather, this section will focus on the core of the theory and several important results from its implementation.

Within the quantitative rescattering theory (QRS)[3], the power spectrum of HHG is defined as the product of the photon energy, Ω, and induced dipole moment:

$$P\ (\Omega) \approx \Omega^4 \left| D(\Omega) \right|^2 \qquad (1\text{-}19)$$

and the induced dipole moment is defined as:

$$D(\Omega) = d(\Omega,\theta) W(E,\theta) \qquad (1\text{-}20)$$

In this equation, $d(\Omega,\theta)$ is the energy dependent atomic or molecular photoionization dipole moment and $W(E,\theta)$ is the wave packet amplitude. In this case, E and Ω represent the electron and photon energy, respectively, and θ is the angle between the propagating harmonic and the fundamental beam. The first important result of the QRS is defining the induced dipole as the

product of these two factors that can be calculated independently. The wave packet amplitude, defined as:

$$\left|W(E,\theta)\right|^2 = N(\theta,\ldots)\left|\tilde{W}(E)\right|^2 \quad (1\text{-}21)$$

depends on the ionization rate $N(\theta,\ldots)$ which includes information relative to the phase matching properties outlined in the previous section and is thus dependent on the laser parameters, while the dipole moment is dependent on the medium. The separation of these two parameters is essential in simplifying the calculation of the HHG spectrum.

There are two primary methods of calculating HHG spectra based on the QRS, hereinafter referred to as QRS1 and QRS2. Each method can be viewed as a way of calculating the wavepacket as a means to describe the HHG spectrum, since information regarding the calculation of the dipole moment is readily available with other theoretical tools. The first utilizes the photorecombination cross section to correct for the discrepancies between the resultant HHG yield from the SFA and the observed experimental yield. Calculating the wave packet from the SFA, then, results in a straightforward relationship between the HHG yield from the SFA and the QRS1:

$$P^{QRS1}(\Omega,\theta) = \left|\frac{d(\Omega,\theta)}{d^{PWA}(\Omega,\theta)}\right|^2 P^{SFA}(\Omega,\theta) = \frac{\sigma(\Omega,\theta)}{\sigma^{PWA}(\Omega,\theta)} P^{SFA}(\Omega,\theta) \qquad (1\text{-}22)$$

where $\sigma(\Omega,\theta)$ is the differential photorecombination cross section and $d(\Omega,\theta)$ is calculated separately, typically by using the static-exchange method, which in this case is normalized to the cross section calculated based on the plane-wave approximation (PWA). This provides a closer approximation to the experimental spectrum than the SFA alone.

The second application of this theory, QRS2, follows a slightly different method of calculation that is independent of the PWA and the SFA. This method relies on the calculation of the wave packet of a representative reference atom, defined as a simple model with an identical ionization energy as the target and whose wavepacket can be solved by integration of the TDSE. This method, however, introduces an energy independent phase difference between the two returning wave packets, expressed in the following equation:

$$W^{QRS2}(E,\theta)=\left(\frac{N(\theta)}{N^{ref}}\right)^{1/2}W^{ref}(E)e^{i\Delta\eta}=\left(\frac{N(\theta)}{N^{ref}}\right)^{1/2}\frac{D(\Omega)}{d^{ref}(\Omega)}e^{i\Delta\eta} \quad (1\text{-}23)$$

By calculating the wave packet exactly based on a model with a straightforward dipole moment without an angular dependence, a precise description of the wavepacket for the target atom or molecule can be reached because the wavepacket is assumed to be independent of the atom or molecule used in the HHG process. Based on this calculation, the HHG spectrum from QRS2 is defined as:

$$P^{QRS2}(\Omega,\theta)=\frac{N(\theta)}{N^{ref}}\frac{\sigma(\Omega,\theta)}{\sigma^{ref}(\Omega)}P^{ref} \quad (1\text{-}24)$$

1.4 High Harmonic Spectroscopy

1.4.1 Photoionization dynamics

The purpose of this dissertation is to extend the study of photoionization dynamics to the photorecombination dynamics in HHG, and thus the background photoionization work conducted with respect to the dynamical processes probed in this work is summarized briefly in this section to explain how the processes present in the shared dipole matrix elements. Cooper minima and shape resonances have been shown, in varying degrees, to impact the

photorecombination process in HHG. However, the first full description of these processes and the majority of subsequent studies have come from photoionization studies and an understanding of the impact the dynamical processes have on measurements in photoionization is necessary for a complete discussion of their impact on HHG.

Cooper minima are interference features that result in a minimum in the photoionization cross section of atoms and molecules. Early observations of these minima stemmed from broad minima associated with the photoionization cross section in alkali metals which were later interpreted by Cooper as being the result of interference between positive and negative portions of the radial dipole matrix [34]. As the photon energy increases, the matrix value can have a change of signs reflective of the nodal structure of the orbital and the resultant competing r-weighted contributions from positive and negative lobes. This opposing contribution to the dipole matrix results in a zero or near-zero value in the photoionization cross section.

In order to understand the effect, the radial portion of the outer valence orbitals and continuum *d* waves for Ne and Ar at zero energy are shown in Figure 1.6. Rare gases have *p* valence shells and thus ionization is limited by dipole selection rules to *d* and *s* continuum wave functions. In the case of Ne and Ar, specifically, the amplitude of the dipole matrix element to the *d* wave is several orders of magnitude greater than that of the *s* wave. The *d* wave node is drawn closer to the core as the photon energy is increased, resulting in overlap with the radial wave of Ar at lower energies than that of Ne. Thus, there is contribution from the negative lobe of the *d* wave in Ar at certain energies, while all contributions to the *d* continuum wave are positive from the Ne valence shell. The sign change results in a minimum in the photoionization

cross section of Ar that is not present in Ne. Molecules with lone-pair orbitals similar to those in the noble gases, i.e. halogens, can experience a similar effect[35].

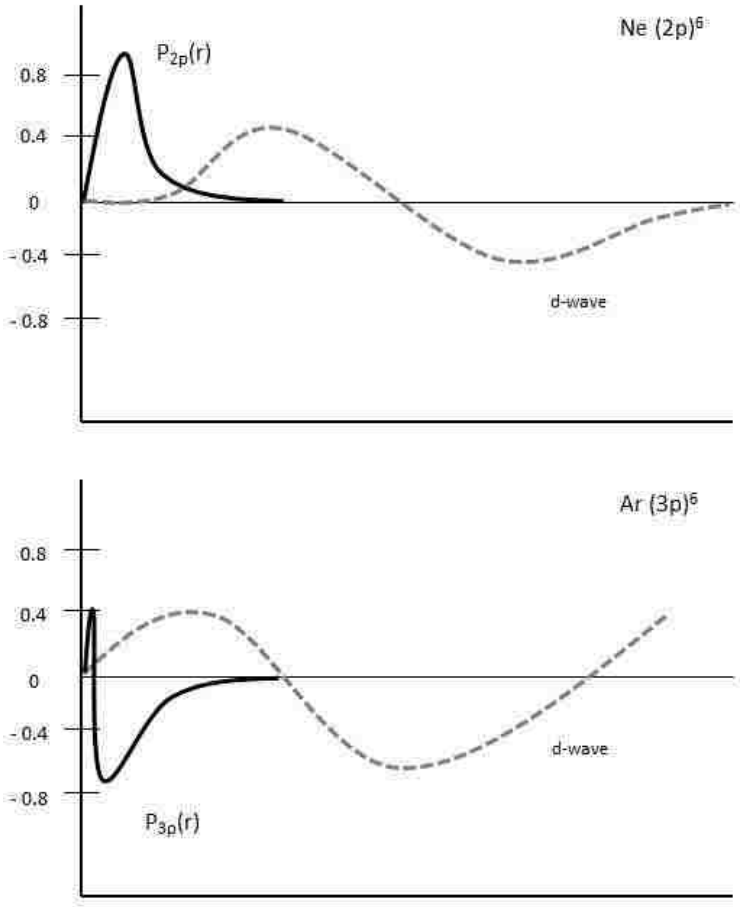

Figure 1.6: A plot of the radial wavefunction (solid lines) of the valence shell for Ne and Ar and associated d-waves (dashed lines), adapted from [34]. The defining deference in this instance is the presence of a node in the Ar wavefunction.

Molecular shape resonances are a ubiquitous single-electron phenomena that occur as a result of the temporary trapping of the photoelectron by a quasi-bound state at resonant energies[36]. The title of “shape” resonance derives from the dependence of the resonant effect on the potential responsible for the temporary trapping of the electron and is observed

through enhancements in the partial photoionization cross section and fluctuations in the energy-dependent photoelectron asymmetry parameter. This effect is manifested in HHG due to the shared dipole matrix elements between photoionization and photorecombination.

A diagram of the basic principle of shape resonances is presented in Figure 1.7. Briefly, the energy diagram is described by two potentials: the first is the effective potential of the photoelectron (thick gray lines) and the second is the potential of the quasi-bound state (thin black lines). The molecular potential can be characterized by the three barriers present. As the electron nears the molecular core, the inner barrier is created by the interaction between the repulsive centrifugal forces and the attractive electrostatic forces, while the two outer barriers form the classically forbidden tunneling region. At electron energies above and below the resonance energy, the wavefunction of the resonance potential has much larger amplitude outside of the photoelectron potential than inside and can be described as an eigenfunction of the outer well. Conversely at energies matching the energy of the resonance, this wavefunction is supported by the inner well in which the initial state of the electron overlaps with the antinode structure displayed in the middle part of Figure 1.7. This energetic and spatial overlap with the initial state results in a centrifugal barrier which temporarily traps the photoelectron during the ionization process. After a time related to the energy width by the uncertainty principle, $\Delta E \Delta t > \hbar / 2$, the photoelectron will tunnel through the supported barrier and emerge outside of the molecular potential.

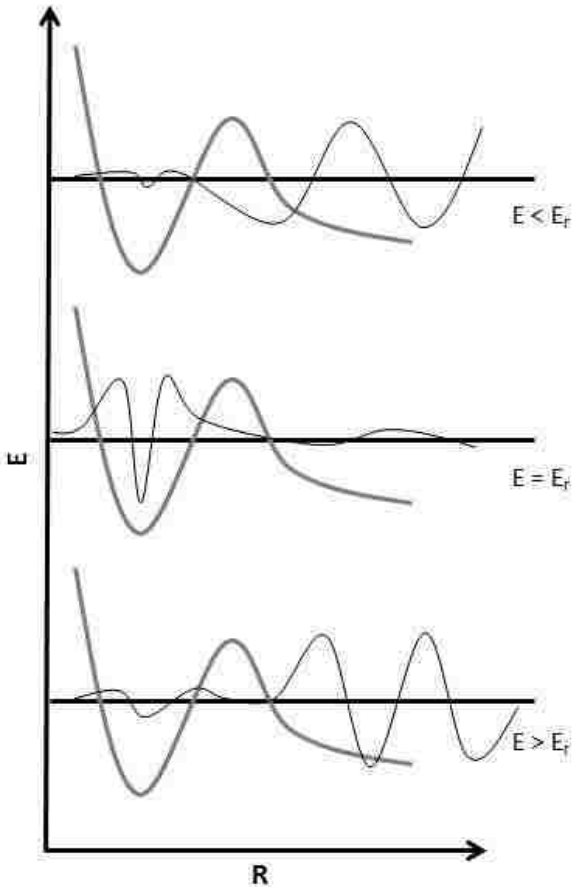

Figure 1.7: A diagram of the basic principle of the shape resonance phenomena. The middle potential diagram demonstrates the situation whereby an internal barrier region is supported by the photoelectron potential. The vertical axis represents the relative energy of the respective potentials and the x axis represents the photoelectron's distance from the molecular core. Adapted from [37].

Shape resonances are most easily identified by measuring the partial photoionization cross section. Specific photoionization channels with embedded shape resonances experience an increase in the dipole transition matrix in the energy range of the resonance [36,38] which in turn increases the amplitude of the partial cross section. These effects are often channel specific, as is the case with N_2, such that the ionization from the HOMO displays a resonance feature while ionization from the HOMO-1 does not[39,40].

In addition to enhancements in the cross section, shape resonances impact the energy-dependent photoelectron asymmetry parameter. The asymmetry parameter, β, relates the total ionization cross section to its angle dependent, differential cross section by [41]:

$$\left(\frac{d\sigma}{d\Omega}\right) = \frac{\sigma_I}{4\pi}\left[1 + \beta P_2(\cos\theta)\right] \qquad (1\text{-}25)$$

in which the second order Legendre polynomial is defined as, $P_2(\cos\theta) \equiv \frac{1}{2}(3\cos^2\theta - 1)$. The θ in this equation is the angle between the emitted photoelectron and the polarization of the photon source. The requirement that the cross section be positive limits valid values of β to the range of -1 to 2. In this way, the angular distribution of photoelectrons is determined by the asymmetry parameter and the differential cross section depends solely on the asymmetry parameter and the total ionization cross section[42]. It can be seen that the differential cross section is independent of the angular distribution at photon energies such that β = 0.

This angular dependence is impacted by the presence of a shape resonance since the tunneling process of the electron through the supported antinode structure results in an asymptotical phase shift of approximately π due to the high angular momentum states responsible for the quasi-binding of the electron[38]. This rapid phase shift is then observable in the asymmetry parameter. An example of this is the e_g shape resonance in the photoionization of SF_6[43]. The C and D channels in SF_6 show little structure in the relevant energy range of the partial ionization cross section, but large shifts in the photoelectron asymmetry parameter are used to confirm the presence of a shape resonance.

1.4.2 Structureless harmonic spectra

In order to effectively observe the impact of photorecombination dynamics on the HHG spectrum, a clear understanding of the structureless HHG spectrum must be established. The earliest theoretical papers [1,2,44] on the subject attempted to provide an explanation for the high-order harmonic emission from noble gases observed in experiments as the duration of laser pulsed breached the picosecond barrier and the instantaneous intensities of the focused lasers increased. Specifically, the onset of a "plateau" region of high order harmonics could not be explained through the typical comparison to above threshold ionization (ATI).

The earliest relevant experiments utilized excimer or Yd based laser systems at sufficiently high intensities to observe harmonic generation [45-51]. These studies examined the harmonic generation from He, Ne, Ar, Kr, and Xe with the highest order harmonics originating from the lighter He and Ne[45,51], with the lone exception being a study at which the intensity was too low to induce tunnel ionization for these atoms[47]. The profile of the harmonics takes a similar pattern, regardless of the generating medium. The odd ordered harmonics reach a maximum near the ionization potential of the target and then slowly decay over many orders. The slow decay, compared to the rapid decay of electron signals measured in ATI experiments, resembles a plateau effect. Following the plateau, an intensity decrease of an order of magnitude signifies the harmonic cutoff. The behavior was first theoretically explained by Krause *et al.* [44], matching experimental results by Crane *et al.*[49] which, taken together, quantified the relationship between the ponderomotive energy of the radiation source and the harmonic cutoff. Deviations from this typical pattern, including local minima and maxima, are taken to be representative of photorecombination dynamics or phase matching anomalies.

1.4.3 Photorecombination dynamics

This section will discuss the observation of the photoionization dynamics outlined in section 1.4.1 in HHG studies. The presence of a Cooper minimum in the generating medium results in a minimum in the HHG signal. This result is best understood in the case of Ar[22,52,53], an atom with a well-defined Cooper minimum in the total photoionization cross section[7], and previous studies have provided insight into the effect of phase matching on the interference phenomena. For an example of the effect of the Cooper minimum in Ar, see Figure 1.1. Wörner *et al.*[53] demonstrated that the energetic position of the Cooper minimum was independent of laser intensity in HHG, while Farrell *et al.*[22] showed the position of the gas jet with respect to the laser focal point determines whether or not the Cooper minimum will be observed at all in HHG. The latter study will now be addressed in more detail as it pertains closely to the current work. By utilizing results from calculation of time dependent Schrödinger equation (TDSE), in conjunction with Maxwell-wave equation (MWE) calculations to account for phase matching, this group was able to calculate the HHG contributions from these two channels independently. The *s* and *d* contributions have an associated phase between them that experiences a change of ~π at the energy of the Cooper minimum in the total photoionization cross section. The result is that the minimum does not appear in the HHG spectrum where it is observed for either independent channel, but rather at the energy where the two channels have equal magnitude. This coherence requirement shifts the location of the minimum to approximately 51 eV. The influence of the phase matching on the location of the minimum is shown by altering the location of the focal position with respect to the gas jet. As a

result, the location, width, and depth of the minimum are shown to change with a change in phase matching conditions.

The observation of the Cooper minima in HHG has been extended to include the high energy (-80 eV) minimum in Kr[25] as well as molecular Cooper minima in : N_2[54], CS_2[55], and CCl_4[55]. The case of N_2 is complicated by multiple orbital contributions, specifically the alignment dependence of the multiple orbitals. The nodal origin of a Cooper minimum results in localized spatial extent of this spectroscopic feature, necessitating a high degree of alignment for its observation. The well understood nature of Cooper minima in HHG, specifically the influence of phase matching conditions on the effect, provides a template for studying additional photoionization dynamics in HHG.

As stated previously, molecular shape resonances occur as a result of the temporary trapping of the photoelectron and are extremely sensitive to the potential responsible for the quasi-binding of the photoelectron resulting in a less obvious effect on the harmonic signal than other spectroscopic features. Resonant enhancements have been observed in HHG from atoms[25], and shape resonances have been shown in HHG for the specific example of N_2[56,57]. In previous HHG molecular studies, the energy range in the harmonic spectra corresponding to the energy range in photoionization studies is enhanced, though the specific conditions for this enhancement are not well understood and the studies do not provide a systematic procedure that would allow one to extract quantitative photoionization parameters (e.g., cross section curves) from HHG spectra.

Theoretical predictions concerning HHG in the presence of a resonance with an autoionizing state suggested an additional step to the classical three step model during which

the wave packet is temporarily trapped before recombination can complete[58]. This temporary trapping results in an energy dependent population buildup and was later extended in theory to shape resonances[59]. This is, essentially, the reverse process of the population buildup familiar in the photoionization cross section. This relationship is evident based on the QRS theory of HHG which equates the HHG spectrum to a product of ionization effects and the photorecombination cross section. Since recombination is the inverse of photoionization, resonant effects in photoionization should manifest in an inverse manner in photorecombination. The similarities between the harmonic envelope and the photoionization cross section appear to be most prevalent theoretically in long trajectories while short recombination trajectories do not contribute significantly to the resonant enhancement[58,59]. This selectivity is based on the lifetime of the shape resonance relative to the temporal duration of long and short trajectories. The long trajectory contributions are more complex due to the higher phase acquired in the electric field and specific experimental conditions are often utilized to select the short trajectory contributions, effectively washing out any potential resonant enhancement of higher order harmonics. Furthermore, the mixture of contributing states in molecular HHG due to the presence of a strong field can wash out features prominent in one channel but absent in another[27].

1.4.4 Nuclear dynamics

The first application of high harmonic spectroscopy was the observation of nuclear dynamics by tracing the harmonic signal as a function of rotational and vibrational excitation through pump-probe techniques. The background of these developments is discussed to provide context for the current work in a developing field. The experiments that follow the

work presented here will likely combine the information probed in section 1.4.3 with the nuclear dynamics principles previously studied in the HHG community.

Rotational revivals were initially probed in HHG due to the desire to align linear molecules prior to the HHG process [60,61]. An initial, weaker pulse is focused into a cold gas jet in order to excite a rotational wave packet and a delayed pulse is used to produce HHG radiation. Since the pulse durations in laser systems used in HHG are necessarily shorter than the rotational period of the target molecule, this alignment occurs after the pulse and is thus referred to as "field-free" alignment. When the HHG intensity is measured as a function of the temporal delay between these pulses, harmonic enhancements occur in the form of beats at four intervals within the rotational period.

This process, specifically, occurs when a linearly polarized laser tuned to the resonance, or near the resonance, of a rotationally excited state of a molecule interacts with a linear molecule in a rotationally cold gas jet[62]. As confirmation of this excitation, the rotational stage propagates long after the duration of the pulse, as seen in Figure 1.8. This figure displays the total harmonic intensity of N_2 versus the pump-probe delay time in picoseconds. A large peak can be observed near 8.5 ps, the time corresponding to the full rotational revival. The full rotational revival is defined by: $T_{\text{rev}} = 1/(2Bc)$, in which c is the speed of light and B is the rotational constant, a unique value for each molecule based on the equilibrium bond length. At this point, the molecular phase is tuned such that the molecule is strongly aligned with the pump field. This results in increased phase matching and enhanced harmonic generation[63].

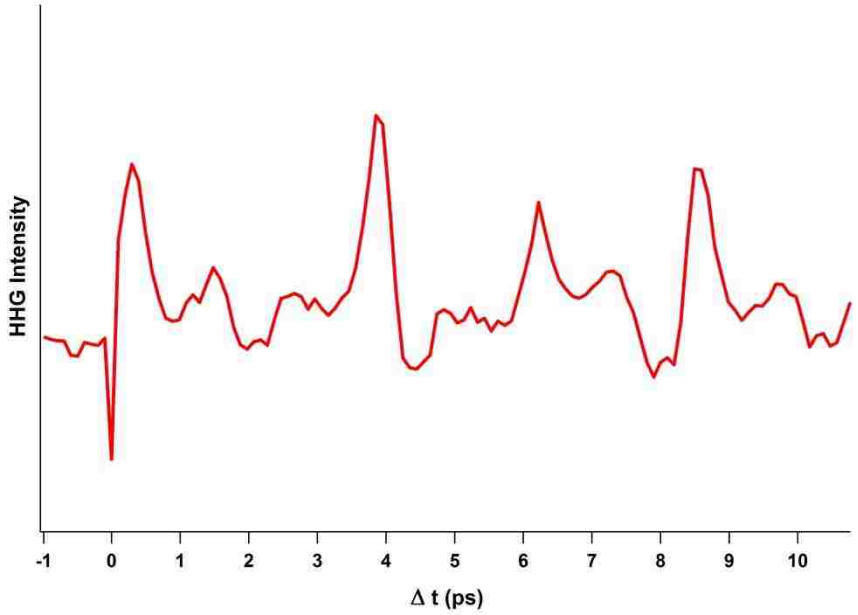

Figure 1.8: Total harmonic intensity versus delay time for N_2. These results were taken from our current work in the lab in order to demonstrate the rotational revivals. A peak at approx. 8.5 ps confirms the literature value for the full revival[63].

There are three other peaks observable in Figure 1.5 that correspond to the ¼, ½, and ¾ revival times. The half revival time is the mirror image of the full revival and, in the case of N_2, results in a higher harmonic enhancement. At each of these positions, the wave packet is rephased such that the molecule is also aligned with the pump field[64]. The peak located at $\Delta t = 1/4Bc$ is negative with respect to the harmonic intensity because it is 180^o out of phase.

The ability to observe these rotational revivals as a function of harmonic intensity directly led to the observation of molecular vibrations with a similar pump-probe scheme. Li *et al.* [65] used an 800 nm laser to impulsively excite the vibrational state in N_2O_4, an NO_2 dimer with a Raman active ground vibrational state localized on the N-N bond. The oscillation in harmonic intensity as a function of pump-probe delay confirmed the vibrational excitation while the favorability of HHG from internuclear separations at the outer turning point demonstrates the interference from a competing electronic channel in the recombination

process at the inner turning point, even though the ionization rate remains constant. In this way, the recombination dynamics expressed in HHG reveal characteristics not accessible in other spectroscopic methods. These results were further supported by strong field ionization calculations[66].

The ultrafast timescale of HHG and the broad applications of the low intensity IR pump have resulted in a robust spectroscopic method. This technique has been further utilized to observe dynamics related to multiple Raman modes in SF_6[67,68], probe conical intersection dynamics in NO_2[69], track the photodissociation of Br_2[26], and develop orbital reconstruction methods for small molecules[70-72].

Chapter 2: Experimental

This chapter will discuss the experimental setup, shown as a general block diagram in Figure 2.1. Each section will focus on a major component of the experiment and the technical and theoretical details of each respective component.

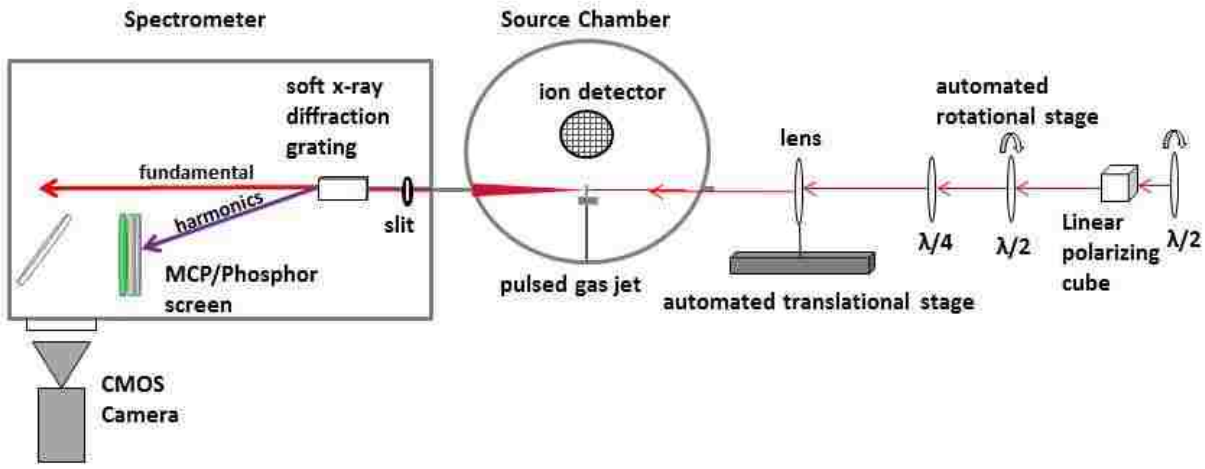

Figure 2.1**:** Block diagram of the single beam optics and the source chamber and spectrometer for all harmonic experiments.

2.1 Radiation Source

2.1.1 Laser systems

The two sources of radiation used in this experiment are described in this section. Preliminary data was acquired using the Kansas Light Source (KLS)[73], a chirped Ti:Sapphire system with 25 fs FWHM pulses, a repetition rate of 2 kHz, a center wavelength of 790 nm, and an average of 2 mJ of energy per pulse. These laser characteristics are necessary for this experiment because sufficient per pulse energy at long wavelengths is necessary for tunnel ionization while short pulses make multiphoton ionization statistically less prevalent. The

chirped pulse amplification (CPA) system for acquiring ultrashort pulses with high intensity will be briefly explained in this section and consists of four main components: a seed laser, a stretcher, an amplifier, and a compressor.

The seed laser for this system consists of a frequency doubled Nd:YAG laser. This source produces a broad wavelength spectrum with nanojoule intensity and 10 fs pulses. This source is then stretched out by a series of gratings to a temporally extended range of approximately 200 ps with the per pulse energy reduced by the same factor. The stretching process has variant impacts on radiation at differing wavelengths resulting in shorter wavelengths being delayed more so than the longer wavelengths. Thereby the longer wavelengths typically exit the stretcher before the short wavelengths and the pulse is chirped. The longer, chirped pulse is then sent through an amplifying medium, in this case a sapphire crystal doped with titanium ions, resulting in a gain of 10^3. The stretcher is necessary for this process because the lower intensity beam prevents damage to the amplifying medium. The pulse is sent through two amplifiers in the KLS, resulting in final output of a 30 ps pulse with 5 mJ of energy and a central wavelength of 790 nm. Following amplification, the laser is sent though another pair of gratings that acts on the radiation in a manner opposite that of the stretcher, referred to as the compressor. Thus the longer wavelengths are delayed more so than the shorter wavelengths and the shorter wavelengths exit the compressor at approximately the same time as the longer wavelengths. This process effectively removes the chirp induced by the stretcher and compresses the pulse to 25 fs at 2.5 mJ.

The second laser system utilized in this experiment follows the same method of output of the KLS, but has a significantly higher total power. Referred to as the high intensity tunable

source, the HITS laser is a commercially available, KMLabs Red Dragon 20 mJ system. The system achieves a total pulse energy of 18 mJ at a 1 kHz repetition rate with a central wavelength of 800 nm. Similar to the KLS, this system is also a CPA laser with an additional amplifier, each with Cryo-cooled amplification Ti:Sapphire crystals that eliminate the need for continuous liquid-nitrogen cooling. This allows the laser to run for weeks, rather than hours and expedites the data collection process.

2.1.2 Optical parametric amplifier

An optical parametric amplifier (OPA) is used in conjunction with the HITS laser in order to produce radiation at wavelengths longer than the fundamental 800 nm. An OPA is a nonlinear optical device that separates a pump beam into two, lower energy beams such that[74]:

$$\omega_p = \omega_s + \omega_i \quad (2\text{-}1)$$

In which *p, s,* and *i* refer to the pump, signal, and idler beams, respectively. The idler beam is labeled as the lower energy beam out of convention. Depending on the design of the system, these values are highly tunable, in our case the signal and idler beams have nm precision.

The principles of this process will now be briefly discussed. The fundamental of the HITS is initially split into three, lower energy, beams. The first of these, termed the seed beam, is then focused through a thin piece of fused sapphire and a white light continuum is generated. This continuum has a broad spectral range, from the visible to near-IR, but loses an order of magnitude pulse energy.

Following white light generation, the seed is overlapped temporally and spatially with a portion of the fundamental. The two beams are then focused onto a beta Barium borate (BBO)

crystal with type II phase matching to amplify the intensity of the desired wavelength. The portion of the white light amplified depends entirely on the angle of the white light to the crystal. This amplification process is repeated with the third portion of the fundamental and an additional BBO crystal. The resulting signal and idler beams are orthogonal to each other and can be separated based on their polarity.

2.1.3 Single beam optics

The first step in the optical setup is to reduce the per pulse energy of the fundamental to reduce multiphoton ionization and damage to the optics. This is accomplished in two steps: the first step reduces the beam by utilizing a beam splitter while the second step uses a half wave plate in conjunction with a linear polarizer. We begin be using a 50/50 beam splitter to reduce the average power of the beam from 4 W to approximately 2 W when using the KLS and several additional beam splitters are used to reduce the power from the HITS. The beam splitter operates by reflecting half of the beam while transmitting the remaining half.

Following the beam splitters, we further control the per pulse energy of the beam by employing a rotatable half wave plate and linear polarizer. The polarization of an electromagnetic wave can be described by the following equations[75]:

$$E_x = A_x e^{i\omega t} \qquad (2\text{-}2)$$

$$E_y = A_y e^{i(\omega t+\phi)} \qquad (2\text{-}3)$$

In which A is the amplitude of the electric field, ω is the frequency, and Φ is the phase between the two components. When Φ is equal to zero, the two components are in phase and the wave is plane-polarized.

A linearly polarized laser can be described as the summation of perpendicular and parallel electric components that are in phase with each other. A half wave plate is a spherical mirror coated such that at a certain wavelength, the parallel component will propagate through the mirror slower than the perpendicular component, adjusting the phase between the two by π. The degree to which the parallel component will slow depends on the angle of the half wave plate with respect to the normal polarization of the laser. The parts of the beam affected by the half wave plate will then be filtered in our experiment by the linear polarizer. We utilize a Glan-Thompson prism for this purpose. This polarizing component consists of two right angle prisms stacked such that their "long" sides are nearly in contact with each other. As the non-plane polarized light enters the prism, the electric component that is normal to the optical axis of the prism emerges parallel to the interface between the two components while the electric component that is not normal is reflected. The final energy of the beam is then given by Snell's law as:

$$E = E_{\max} \sin^2(2\theta) \qquad (2\text{-}4)$$

This equation shows that when the half wave plate is normal to the polarization of the incident light (e.g. θ=45^o), the output energy will be equal to the input. With an automated half wave plate capable of 0.5 degree accuracy, a very precise variation in per pulse amplitude can be achieved.

Some experiments outlined in this document refer to HHG from elliptically polarized fields, further optics are required to induce this polarization. While half wave plates alter the phase of the perpendicular and parallel components by π, a quarter wave plate alters the phase by π/2. Thus with the angle of the linear laser off by 45^o with respect to the orientation of the

quarter wave plate, the light will become circularly polarized, whereas the light will continue as an unobstructed linearly polarized if the laser is normal to the quarter wave plate. Any angle between 0^o and 45^o will result in an elliptically polarized beam. In order to achieve this, the angle of the quarter wave plate needs to be rotated, or the axis of the linearly polarized beam needs to be rotated before it hits the quarter wave plate. The latter option is chosen in order to ensure the axis of polarization remains unchanged with a change in ellipticity. We place a rotatable half wave plate in front of the quarter wave plate on axis with the center of the source chamber such that at 0^o the light is unchanged and remains linear. With each degree of rotation of the half wave plate, the overall ellipticity is changed by two degrees, reaching circular polarization when the half wave plate is at 22.5^o.

The laser is focused into the source chamber using a spherical lens. Varying focal lengths are used in order to increase or decrease the peak intensity. With the KLS, we used a 50 cm focal length lens to achieve a peak laser intensity of 3.4×10^{14} W/cm^2, with an average power of 1.85 W and with the HITS, we used a 1 m lens to achieve a peak laser intensity of ~5.0×10^{14} W/cm^2. The lens is mounted on automated rotational and translational stages in order to vary the phase matching conditions and the location of the center of the gas jet is determined by measuring the ionization rate versus lens position.

2.2 Source Chamber

2.2.1 Gas jet

The rise of ultrafast laser systems necessitated the development of gas valves with equivocally high repetition rates. We use three such valves in this experiment: a high-repetition rate cantilever piezoelectric valve, the more common Even-Lavie valve, and a cw effusive jet.

The selection of which is dependent on the gas in use. The source chamber has an approximate base pressure of 10^{-7} Torr, which is raised to maximum of 10^{-4} Torr with the operation of the gas valve. The differential tubing between the source chamber and spectrometer keeps the pressure in the spectrometer down near 20^{-6} Torr in order to protect the sensitive microchannel plates that can be damaged with a large applied potential at higher pressures. Both valves are triggered off the source oscillator and optimized independently to achieve maximum harmonic signal with respect to the pulse duration, repetition rate, and delay following the trigger.

For SF_6, we utilized the cantilever piezoelectric pulsed gas valve[76]. Pressurized SF_6 is a liquid in the gas cylinder that supplies gas phase SF_6 by the built up vapor pressure in the bottles. For this reason, the highest backing pressure we can reasonably obtain with this gas is 50 psi preventing us from using the Even-Lavie valve. The valve was also used for Ar when conducting experiments intended to compare the harmonic spectra of the two gases to ensure comparative phase matching conditions based on the shape of the molecular or atomic beam. The piezoelectric valve operates by using a 6 mm cantilever covering the small aperture with a default open setting with no applied electric field. The cantilever is forced shut with a 1000 V/mm field strength that equates to 1.5 N of force, sufficient to create a vacuum seal even with a high pressure differential. The opening time of this valve is steady as low as 6 µs at repetition rates up to 5 kHz.

For N_2 and CO_2, a much higher backing pressure was possible (~1000 psi), allowing us to use the Even-Lavie valve[77]. This was especially important in alignment experiments that require rotational cooling in the gas jet. This valve was sufficient for the purposes of our

experiments at high backing pressures, but was unstable at lower pressures. We attempted, for instance, to use this valve in conjunction with the molecular targets SF_6, CF_4, and $SiCl_4$ which have a maximum backing pressure of 50, 75, and 30 psi, respectively. The pressure in the source chamber fluctuated as much as a half order of magnitude even with a steady repetition rate and opening time due to the lower backing pressures.

The gas jet in later experiments was provided by a soda-lime glass nozzle with an aperture of 0.15 mm. The backing pressure behind the nozzle is held near 100 Torr with a needle valve resulting in a source chamber pressure of approximately 10^{-5} Torr pumped by a Leybold Turbovac Mag W/2200 DN 250 CF that has an 1800 L/s pumping speed. This greatly simplifies the experiment by eliminating the timing aspect and is far more stable than the pulsed gas valve. However, the resulting beam is effusive rather than supersonic and thus has a lower gas density and broader angular momentum distribution[78]. For this reason, results obtained using the effusive jet are not directly comparable to results obtained using the pulsed valve.

2.2.2 Ion detector

The center of the gas jet is determined by measuring the ion signal as a function of lens position with a simple ion detector in the source chamber. We applied 800V to a fine mesh mounted to the chamber, the ion peak from this detector was initially monitored on an oscilloscope to find harmonic signal and later connected to the PicoScope application in LabView to constantly measure the ion signal. We found it necessary to place the ion detector off axis and several inches away from the gas jet. If the detector was too close to the gas jet,

the voltage from the grid could arc and turn off the gas jet at random times within the experiment.

A more accurate measure of the ionization rate was desired for the calibration of the laser intensity and a channeltron with 1 kV applied potential was used instead of the mesh grid in later experiments. Communication problems between the PicoScope and LabView eventually led us to use direct input of the Tektronix oscilloscope in LabView in lieu of the PicoScope. This change added up to half second in acquisition time per data point, but was a net positive on the experiment due to increased reliability and ease of use.

2.3 Spectrometer

2.3.1 Slit and diffraction grating

The differential pumping tube connecting the source chamber and the spectrometer has a diameter of approximately 10 mm, which significantly clips the fundamental IR beam as it loses coherence following the focus. The remaining mixture of IR and harmonics passes through a Newport M-SV-0.5 slit to partially filter out the bulk of the fundamental beam and reduce the spatial component of the mixture to a rough point source for optimal grating efficiency. The slit has an operational width of 0 – 5 mm and 12.7 mm height.

The separation of harmonics into single wavelength components is accomplished by using a Shimadzu 30-002 soft x-ray laminar diffraction grating with a groove density of 1200 grooves/mm and a length of 25.3 mm. The grooves are approximately 15 nm deep and follow a rectangular well pattern. The diffraction equation determines the angle at which they are separated[75]:

$$\sin\alpha + \sin\beta = Nm\lambda \quad (2\text{-}5)$$

In which α is the angle between the normal to the gratings and the polychromatic light, β is the angle between the normal to the grating and the diffracted light, *N* is the groove density, *m* is the order of diffraction, and λ *is* the wavelength. For light with a zero-order diffraction, it is easy to see that the two angles are equal with opposite signs. In our setup, 800 nm light hits the grating at approximately 1^{o} and reflected at -1^{o}, missing the detector and exiting the spectrometer. It is also clear in the diffraction equation that light with differing wavelengths will have different angles of diffraction, allowing us to calibrate the position sensitive detector by carefully measuring the distance and angle between the grating and the detector.

2.3.2 MCP detector

The separated beams of harmonics are projected onto a space sensitive detector consisting of a stack of microchannel plates and a phosphor screen. A microchannel plate[79] is an array of fused electron multipliers which have a diameter of approximately 10 microns. The plate has a charge across it that determines the effective multiplier potential of each channel. When a photon strikes the end of the channel, a cascade of electrons is released that multiply with every contact with the channel walls. The channels are set at a bias angle of 5 degrees to insure an initial contact near the surface of the plate.

A typical microchannel plate (MCP) detector utilizes more than one plate in a stacked formation to increase the multiplication of each impact. In our experiments, we used two multi plate configurations. The first is known as the “chevron” configuration and consists of two microchannel plates. The angles of the channels are set opposite of each to maximize the total gain. The second configuration is a “z-stack’ that uses the same principle of the first configuration, but adds a third plate to the stack with angles opposite of the second plate.

Looking at a cross section of the stack would reveal “z” shape multi-plate channels. The chevron detector was used to collect preliminary data, was circular in shape, had a diameter of 8 cm, and a channel diameter of 10 microns. Each plate had an applied potential of 900 V, while the z-stack detector consisted of rectangular plates with a width of 10 cm and a height of 4 cm and an applied potential of 800 V per plate. This is only slightly larger than the vertical profile of harmonics projected onto the detector, making this a more efficient system than the circular MCP. The increased gain from the z-stack configuration is necessary for the lower conversion efficiency we expect with longer wavelength sources. The channel diameter on this system, however, is 25 microns, which results in slightly blurred images compared to the plates with smaller channels.

Electrons released from the last microchannel plate are projected onto a phosphor screen with a 3.6 kV applied potential. The phosphor screen consists of a clear, conductive material coated with a phosphor substrate. A potential, typically much higher than the potential on the MCPs, results in a phosphorescent effect when the electrons hit the surface[80]. As a result, the spot on the screen where the electron makes contact will glow in proportion to the amount of electrons striking it, indicative of the intensity of the diffracted light. With a high repetition rate, this results in a constant measurable impact on the screen in the location of a photon beam making contact.

2.3.3 CMOS camera

The raw data taken in these experiments is in the form of images of the phosphor screen. Images are record with a Hamamatsu C11440 Orca-flash 2.8 complementary meta-oxide-semiconductor (CMOS) camera that actively records the intensity value of each pixel of

the detector. The camera exposure time is set in individual experiments to prevent overexposure and optimize the time of data collection. The exposure time most often used is 0.3 s. The images stored as data points are summations of 8 or 16 of the 0.3 s exposure images, depending on the intensity of the signal. For example, the additional time required to double the images taken is valuable if we are measuring the elliptical dependence of the harmonic generation due to the rapid cutoff decline with an increase in ellipticity. For this reason, however, the intensities reported for each harmonic have little quantitative meaning as too many variables impact the actual numbers reported.

For each laser intensity, angle of ellipticity, and angle of the pump beam in our alignment studies, a background image was taken under the same conditions outlined in the previous paragraph (i.e. 8 images at 0.3 s exposure) with the gas jet turned off. This was done to correct the detector for its sensitivity to ambient light that may enter the spectrometer from the room, or scattered light from the fundamental in either the source chamber or spectrometer. By taking background images at every experimental condition related to the fundamental, we can be assured that the signal on the detector we report is related to harmonic generation instead of experimental flaws.

2.4 Data Collection and Analysis

2.4.1 LabView

All automated features of the experiment are controlled with a LabView data acquisition program. The position of the lens is controlled by a Newport ESP series 3 axis controller in conjunction with a motorized translational stage with micrometer precision. The same setup is

used to control the delay stage in the pump-probe setup. We used a PI-miCos DT-80 rotation stage in order to precisely control the laser intensity and polarization angle. This stage has a typical precision of 0.004^{o} with a bi-directional repeatability of ±0.2^{o}. An important note regarding the rotational stage is the need to limit its motion to one direction during data acquisition to insure precise angle repeatability.

The LabView code is written such that the controls of the camera and the stages are automated within the same program. The motion of the translational stage is the slowest part of the experiment, thus the program collects data at all relevant angles, (e.g. intensities, elliptical polarizations, and molecular alignment angles) at each lens position before moving to the next. Once all desired data has been taken, the translational stage returns to the first position and the experiment is repeated such that multiple averages of the same data are acquired non-sequentially. At each set of experimental conditions, LabView stores an image and related XML file with all experimental details including ion signal provided by the PicoScope 5203, a device that functions as a USB oscilloscope or a digitized screenshot of the Tektronix oscilloscope.

2.4.2 IgorPro

All data processing and figure creation was done with IgorPro. This program has both a convenient graphical user interface for figures as well as the ability to program more complex data analysis procedures. For the purpose of the results presented in this document, several user programs were written to expedite the analysis of large data sets.

A data set which contains any number of images and averages is processed in the following way: first the background images for the respective laser intensities are loaded into

the program. For data involving elliptically polarized light, this includes a background image at every angle of ellipticity. Similarly, for data involving multiple angles of molecular alignment, a background image corresponding to each angle is loaded within Igor. Following the acquisition of the relevant background data, images are loaded, analyzed, and discarded individually to avoid overloading the computer memory. Each image is subtracted by the corresponding background image and the vertical pixels are integrated to create a typical harmonic "lineout" that displays the relative intensity of harmonics and their Gaussian nature. The program then averages the value of the maximum and two points on either side of the peak from each harmonic and these values are saved as a harmonic envelope, used to present data in this paper and corresponding publications. The envelope (hereon referred to as the harmonic spectrum) is typically divided by its sum for experimental deviations, such as pressure fluctuations and changing laser intensities, which are independent of the effects being studied. In order to prevent arbitrary spikes in the spectra following this normalization, harmonics that are less than 4% of the maximum are set to zero so they do not contribute to the sum used in the normalization process. The process of envelope extraction is further outlined in Figure 2.2. Following the harmonic spectrum extraction, the image is deleted and the process is repeated for each following image for all averages. Each image, or data point, is then averaged over all analogous images with the standard deviation calculated automatically, which is in turn presented as error bars in the spectra.

There is some uncertainty in the position of the harmonics on the detector due to a non-perfect alignment of the diffraction grating and source laser. This results in the XUV pulse hitting the grating at slightly differing angles depending on the position of the focal point with

respect to the center of the gas jet. This in turn could create error in the pixel “windows” selected to extract the highest value of the harmonic intensity. This source of error can be neglected given the results presented in Figure 2.3. After extraction of the lineout from images

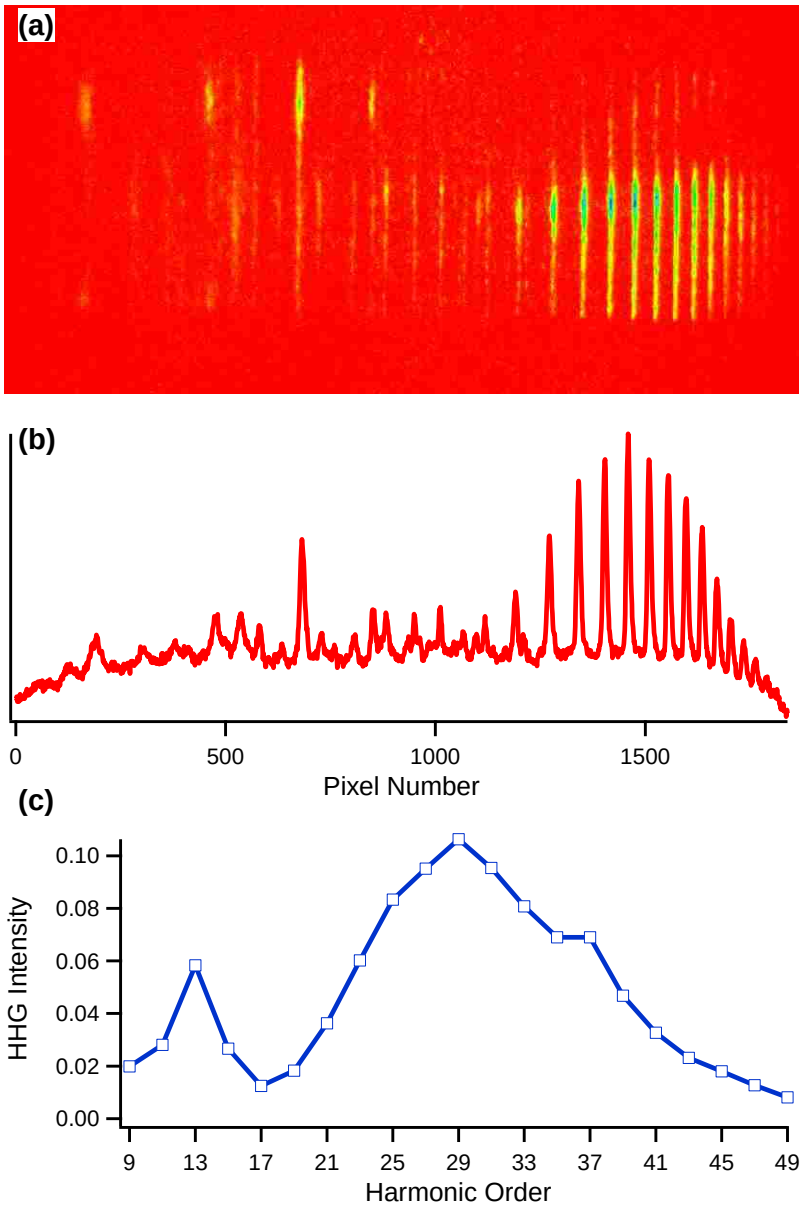

Figure 2.2**:** An example of the basic data processing used in this paper. Each data point begins as a raw image (a). The rows are the summed to create a harmonic lineout (b). The peaks are then extracted to create a harmonic envelope (c), referred to in this dissertation as the harmonic spectrum.

taken every 0.25 mm from (-) 5 mm to (+) 5 mm at 11 different pulse energies over 10 averages (a total of 4400 images), the peak within each of the windows for harmonics within the cutoff at all present pulse energies for Ar is tallied (blue lines) and presented within the extraction windows for each respective harmonic (black lines). The error is most present in the lower ordered harmonics, while the peak tends to narrow as the harmonic order increases. There are no harmonics orders at which a significant portion of the peaks is close to the border of the window and thus the approximation made in the data processing is acceptable.

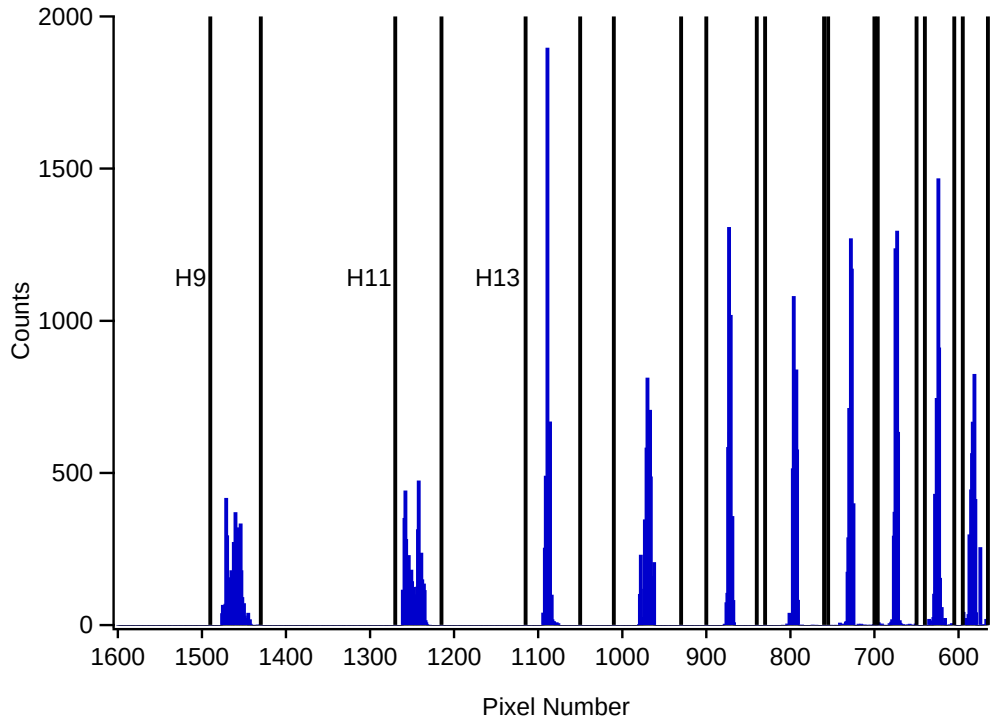

Figure 2.3: Tallied harmonic peaks from each harmonic window from 4400 images of the HHG from Ar. While the error is significant at H9 and H11, the window is large enough to encapsulate all possible peak pixel positions. The error decreases somewhat with increasing harmonic order and the approximation appears valid.

For data sets that are strictly linear and unaligned, this is the end of the process. For elliptically polarized data, the harmonic spectra for all angles at each phase matching condition are normalized to the spectrum with zero ellipticity, e.g. linearly polarized light. At this point the waves for each phase matching condition, in this case this refers to lens position, are added to a matrix to produce the contour plots presented later in this document. In addition to the normalized ratios, the elliptical dependence of each harmonic is fitted to the Gaussian function for the exponential decay of harmonic intensity with an increase in ellipticity in order to extract the related β coefficient.

Chapter 3: Impact of the Gas Medium Width on the Harmonic Generation from Ar

3.1 Introduction

This chapter will address the most favorable experimental apparatus needed to examine photorecombination dynamics in HHG. This is achieved by examining the effect of large changes in the phase matching conditions for multiple experimental conditions. Photorecombination dynamics occur as variations in the dipole matrix elements connecting the ground state of the parent ion to the recombining continuum and may be sensitive to the duration of the electron in the continuum[81], a possibility that would be affected by contributions from the different temporal contributions in HHG. Since the change in phase matching conditions can impact the selection of trajectory contributions[17,20,23,33,82-86], a systematic study of the changes in long and short trajectory contributions over a broad range of focal positions is necessary with the various utilized experimental apparatuses in order to define the most reproducible setup.

A key measure in any HHG experiment that impacts the phase matching and trajectory contributions is the length of the Rayleigh range in relation to the width of the generating medium. To this extent, the results of using two different laser systems and gas jets (outlined in sections 2.1.1 and 2.2.1, respectively) are discussed in this chapter with a detailed discussion concerning the impact the components have on the detection of long and short trajectory contributions. The results from the different systems are comparable due to a constant Rayleigh length and ponderomotive energy, allowing overarching conclusions regarding the influence of the specific gas jet on the harmonic output.

The use of a pulsed gas jet has been necessary in the production of HHG from many systems because a high density gas region is needed to drive the HHG process. An alternative to this used more recently is the finite or semi-infinite gas cell, which avoids timing complications from using the pulsed gas jet and pulsed laser. The use of a gas cell effectively increases the interaction region consisting of the gaseous medium and the source laser, which in turn has been shown to significantly increase the overall harmonic yield. The effect of changes in the phase matching conditions with this gas cell, including the presence and intensity of the long trajectory contributions, however, has been shown to be different than previously reported results from pulsed gas jets. This suggests that new sources necessitate further systematic studies of phase matching effects.

This study examines the harmonic spectra of Ar with two different gas jets and laser systems in order to determine zeroth order experimental procedures for the extraction of photorecombination dynamics. The results section focuses on the characterization of harmonics generated from the two sources, including the impact of multiple quantum paths on the harmonic yield from differing apparatuses. Argon has a well-studied Cooper minimum in the total photoionization cross section that results in a minimum in the HHG spectrum, an effect that has previously been shown to depend on phase matching conditions[22]. The discussion section demonstrates the sensitivity of this spectroscopic feature to changing focal point positions with the pulsed jet and the stability of the feature with a change in focal point positions with the cw jet. A set of experimental conditions with consistent results with regards to the Cooper minimum in Ar should simplify the process of studying additional dynamics in polyatomic molecules.

3.2 Results

The characterization of the two gas jets is done by recording harmonic spectra over a wide set of focal positions and measuring the total ionic and harmonic yield at each focal position. The results of scanning the lens across a wide set of focal positions is outlined macroscopically in Figure 3.1. The ion yield as a function of focal position is shown for the cw gas jet and HITS laser system (solid black line) and the pulse gas jet and KLS system (dashed blued line). The positions are labeled (-) or (+) depending on the location of the focal point with respect to the center of the gas jet. If the focal point is on the side opposite the detector, the positions are labeled (-) and the positions are labeled (+) when the focal point is on the same side of the gas jet as the detector. From a casual observation, the two curves appear to be nearly identical. This is due to the long Rayleigh length of the two focusing lasers that results in a nearly homogenous intensity region over the span of a few centimeters of focal positions. Examining the ion yield curves closer by fitting each ion yield curve to a Gaussian distribution results in a FWHM of 9 mm for the cw gas jet and a FWHM of 22 mm for the pulsed jet. At first glance, this may be counterintuitive since an effusive jet expands in vacuum much faster than a supersonic jet. However, the focal point is positioned close enough to the aperture to negate the variable expansion rates. Thus, the relative width of the aperture is reflected in the FWHM of the ion signal when comparing the two systems and the narrower gas jet peak width is approximately equal to the confocal parameter of the focusing laser. The FWHM of the ion signal from the wider, pulsed gas jet is directly influence by the width of the aperture.

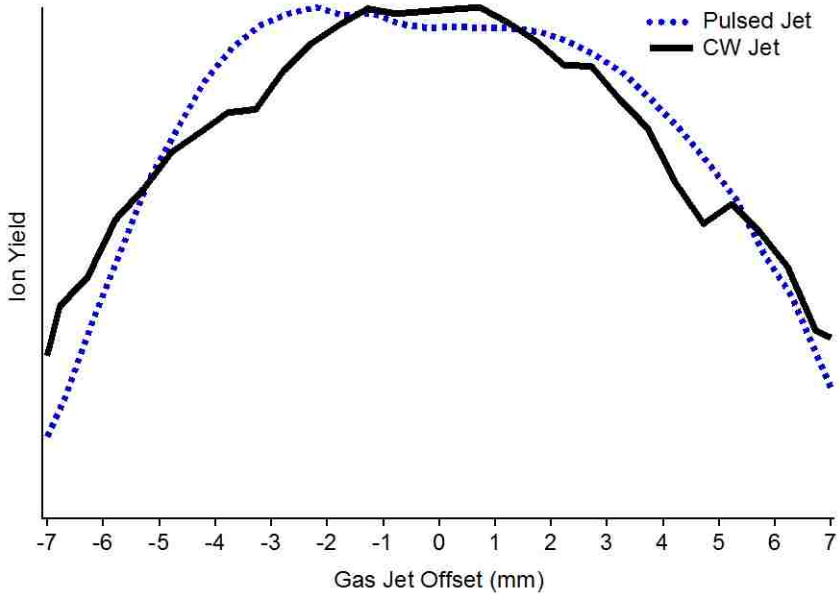

Figure 3.1: Ion yields as a function of focal positions for the pulsed and cw jets.

Figure 3.2 outlines the focal position dependence of four individual harmonics and the total harmonic yield for the two apparatuses. This effect was first studied theoretically by Salieres *et al.*[12]and certain aspects of their results are comparable to the current work. In the cited work, the yield of H45 was measured as a function of the focal position with respect to the gas jet. The phase variation inherent in the movement of the focal point results in two peaks at which either the on-axis or off-axis contributions are optimally phase matched. These peaks are centered at (-) 3 and (+1) mm, respectively. We observe similar behavior in Figure 3.2 (a) in the HHG yield versus focal position for the supersonic, pulsed jet and KLS system. Our peaks are further apart than the previous study (at (-) 5 and (+) 2 mm) with a much larger dip in the middle. The theoretical study does not take into account ionization of the medium, and thus the ionization effects we observe near the center of the gas jet in the current work result in an interfering process that partially cancels out the HHG yield in addition to the poor phase

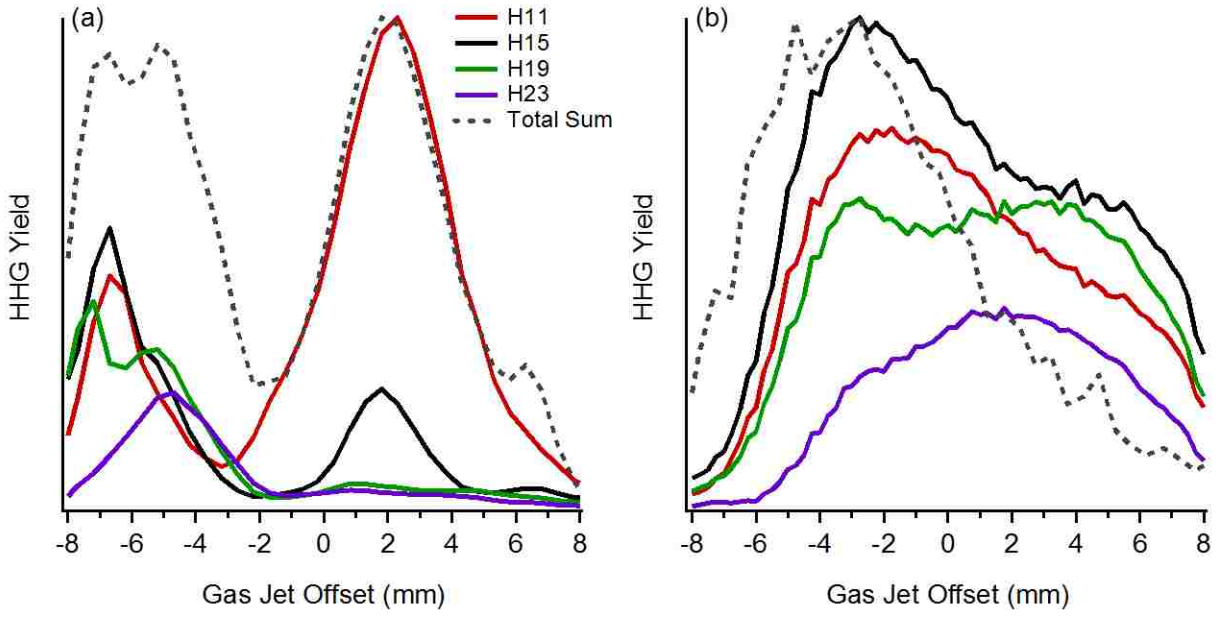

Figure 3.2: Intensity of 4 individual harmonics along with the total harmonic yield as a function of lens position for the pulsed gas jet apparatus (a) and the cw apparatus (b).

matching conditions. This may also explain why our HHG yield peaks are further from the center of the gas jet. It should be noted that the peak on the (-) side of the gas jet appears to move closer to the center with an increase in harmonic order. This can be seen in the line for the total harmonic sum in the distinct two peaks on the (-) side. This is then reflected by the location of the H11 and H15 peaks at (-) 7mm and the H19 and H23 peaks at (-) 5 mm. The higher order harmonics shown in Figure 3.2 have a less intense second peak, but it is located at (+) 1 mm, matching the previously cited theoretical result. This suggests that harmonics closer to the middle of the plateau that experience equal contributions from long and short trajectories over a range of focal positions are more likely to follow the theoretical model.

A similar pattern is found in Figure 3.2 (b) for the second set of experimental conditions utilizing the cw jet and HITS system. In this instance, the HHG peak is moved closer to the center, likely owing to the narrower distribution of the medium. This HHG peak is at (-) 3 mm,

matching the aforementioned theoretical study [12], but there is no peak on the opposing side. This can partially be explained by the quantum path contributions discussed later in this section, but the clear result is that the differing experimental parameters result in significantly different HHG yield patterns as a function of lens position. The lack of a second peak for the individual harmonics and the overall harmonic yield is closer to the results for the focal position dependence of harmonics generated in a gas cell [50]. The overall harmonic spectrum and the response to changes in the phase matching conditions may mirror the results for a gas cell more closely than a pulsed gas jet.

In examining the effect of the phase matching properties on the contributions of different quantum paths, long and short trajectories are differentiated based on the appearance in the raw images following the criteria proposed by Bellini *et al*[11]. Briefly, the bright annular part of the harmonics is assumed to be the on axis contribution from the short trajectories, while the spatially distorted portions of the photon beams are resultant from off axis contributions, or long trajectories. The difference between the long and short trajectories is shown in Figures 3.3 and 3.4. Figure 3.3 shows raw images from the pulsed jet and KLS system, which most closely resemble previously reported results. At large (-) values, or positions where the focal point is far in front of the gas jet, the annular part of the photon beam is missing entirely, indicating primarily long trajectory contributions. The center part of the photon beam becomes visible near (-) 3.5 mm indicating a mixture of quantum path trajectories, while the short trajectories become dominant near -2→ -1 mm and at all (+) focal positions, which confirms the location of (-2) mm many groups employ to ensure primarily short trajectory

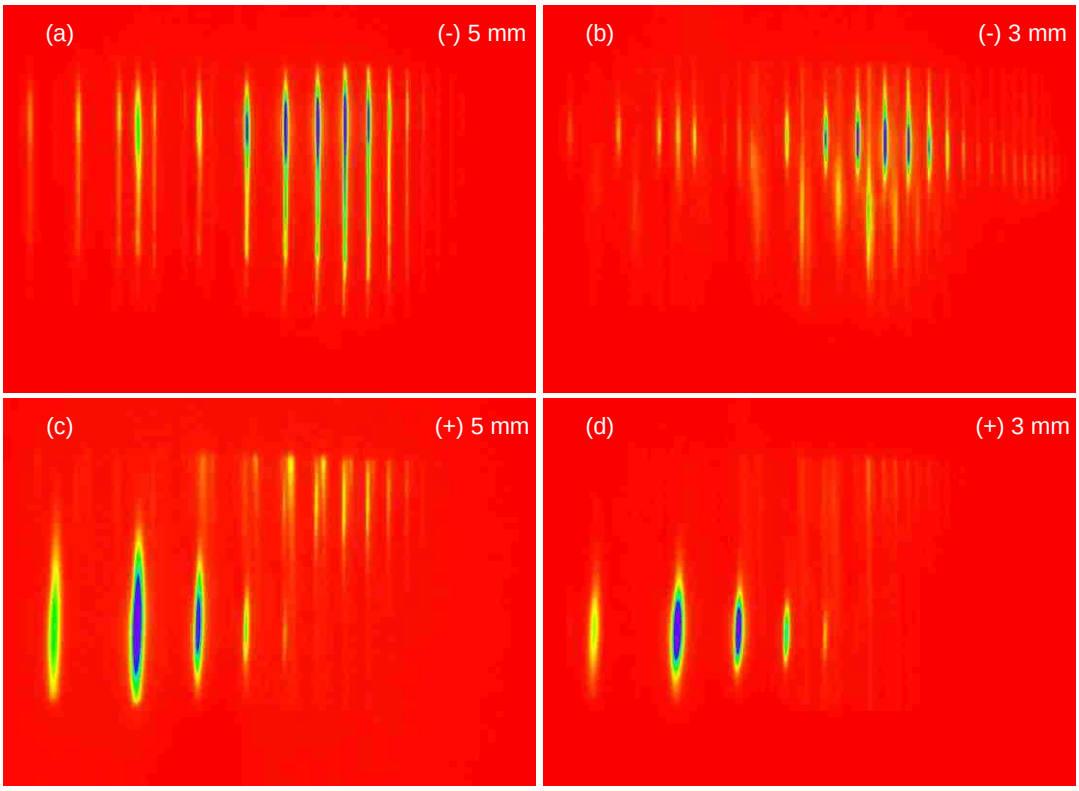

Figure 3.3: Raw HHG images from the KLS system and pulsed gas jet for Ar at four different lens positions. Each panel represents the average of 10 data points with the high color set to 50% of the highest pixel value to clearly show the long trajectory contributions. The ponderomotive energy for the KLS system for these images is ca. 19 eV using a 50 cm lens. The Rayleigh range for the focal condition is 4.5 mm.

contributions [25-27]. The top portion of the long trajectories is significantly brighter than the bottom portion due to a slight tilt in the source laser that is amplified in the HHG process. This is also partially responsible for the small energetic shift between short and long trajectories observed in Figure 3.3 (b). This is approximately the position at which the contributions are the most equal in intensity, and interference between the quantum paths can lead to spectral splitting [84], though the discrepancy observed in this figure is likely to do more general problems in the experimental setup. The long trajectories are also observable in the (+) positions in Figure 3.3, though their contribution to the overall harmonic yield is much less intense than the short trajectories and the top portion of the spatial profile is again more

intense than the bottom portion. Although our results concerning which side of the gas jet feature primarily contributions from the long trajectories contradict the results for similar criteria in the literature [12,24,33], the observation of long trajectories on both sides of the jet indicates the current results are not altogether different from those previously reported.

Raw HHG images from the cw gas jet and HITS laser system with the same positions as the image in Figure 3.3 are presented in Figure 3.4. The major difference between trajectory contributions in this figure compared to the Figure 3.3 is the lack of significant long trajectory

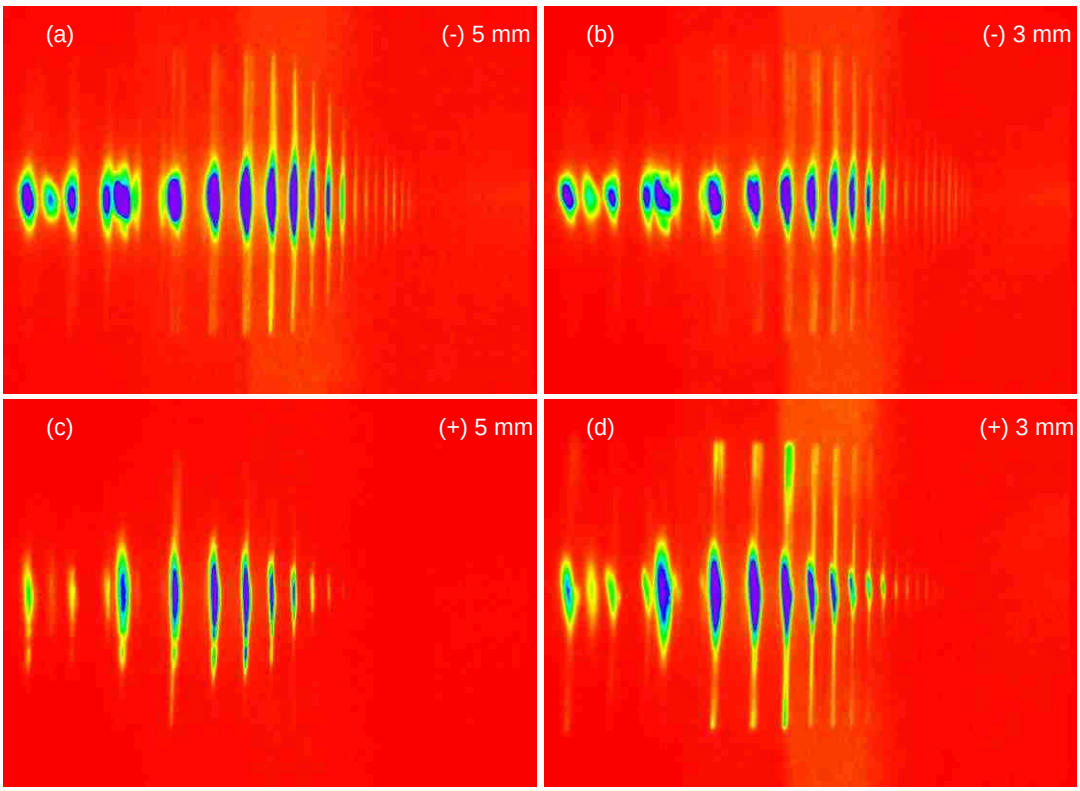

Figure 3.4: Raw HHG image from four focal positions with the CW jet and HITS laser system. The highest color is set to 50% of the highest pixel value to clearly show the long trajectory contributions. The Raleigh range is 4.5 mm, using a 100 cm lens with a beam diameter of 3 cm and the ponderomotive energy is ca. 19 eV.

contributions at any focal position, as indicated by the intensity being concentrated in the center of the image, rather than off-axis. The longer quantum path is observable at all (-) positions and up to (+) 4.5 mm, but there is no location at which the long trajectories are brighter than the short trajectories. A better degree of symmetry between the upper and lower part of the harmonics was able to be achieved with this setup, potentially because the longer focal length simplified the alignment of the fundamental as it defocused. The deviation from our results utilizing the pulsed jet concerning the observation of long and short trajectories may be explained by comparing the results to the macroscopic results associated with gas cells. It has been previously observed that as the length of a gas cell, and in turn the laser and medium interaction region increases, the harmonic spatial distribution increases owing to the increase in contributions from long trajectories[86]. This implies that the contributions from long trajectories would be more intense with the wider pulsed jet than the cw jet, an observable result in Figures 3.3 and 3.4.

3.3 Discussion

The stability of the trajectory contributions with respect to a wide range of phase matching conditions further impacts the ability to observe and potentially extract photorecombination dynamics in the harmonic spectra. In the energy range covered in the harmonic spectra in this chapter, the Cooper minimum in Ar is a spectroscopic feature evident in the harmonic spectrum. Cooper minima in atoms occur due to interference between continuum waves, an effect that results in a phase change of π in the energy range of the minimum[34]. The effect of Cooper minimum in HHG from Ar has been studied extensively [52,87,88] and the effect of changing lens positions has been studied experimentally and

theoretically [22]. However, no studies have been conducted to compare the dependence of Cooper minima on HHG from varying phase matching conditions from multiple sources. This section evaluates the differences observed between the pulsed and cw jet as the harmonic spectrum goes through the Cooper minimum in Ar.

To characterize the effect of changes in the position of the focal point with respect to the observation of the spectroscopic feature, the location of the center of the minimum along with the ratio of H29 to the harmonic where the minimum is centered is presented as a function of lens position for the two experimental apparatuses used in this study in Figure 3.5. Only positions at which the minimum was observed for both experimental conditions were used, but the differences at these positions are enough for a qualitative comparison. These are also the lens positions that can generally described as good phase matching conditions for both apparatuses. The most obvious deviation between the two sets of data is the location of the center of the minimum. In the case of the cw jet, the center of the minimum is consistent even with a large change in the position of the focal point, always located at H33. The pulsed jet results, however, indicate a variation in the minimum location from H35 to H31, depending on the location of the focal point. This energetic shift is consistent with aforementioned results[22] while the cw jet results indicate a harmonic spectrum that is far more resistant to changes in phase matching conditions, a feature previously shown in harmonic spectra of Ar with a gas cell source [52] .

The difference in consistency of the spectra can be further observed by considering the ratio of H29 (generally the beginning of the dip in the harmonic spectrum) with the intensity of the center of the minimum with respect to focal position, shown in Figure 3.5 as green squares.

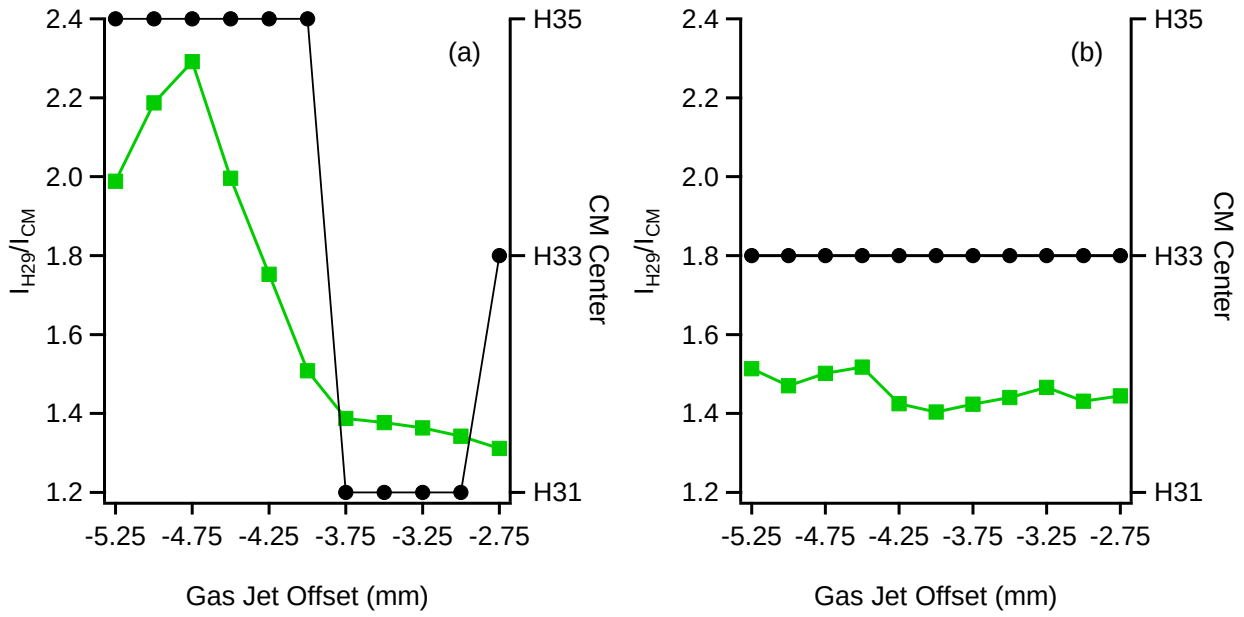

Figure 3.5: The ratio of H29 to the center of the Cooper minimum (green squares) and the location of the Cooper minimum (black circles) as a function of lens position for the KLS and pulsed gas jet apparatus (a) and the HITS and CW jet apparatus (b).

Over the focal point span of 2.5 mm, the ratio of harmonics generation by the pulsed jet ratio has a variance of 54.4% and reaches a maximum at (-) 4.75 mm. Conversely, over the same span, the cw jet has a variance of just 7.8% and reaches a maximum at (-) 4.5 mm. Given the consistency of the location of the minimum combined with the consistency of the depth of the minimum, it is apparent that the HITS laser combined with the CW jet is the experimental apparatus best used for the study of photorecombination dynamics.

Chapter 4: HHG from SF_6: Dissociation of Macroscopic Effects

4.1 Introduction

This chapter examines the effect of shape resonances on HHG from SF_6 and the impact changes in macroscopic properties have on the resonant effect. Recently, a quantitative rescattering theory (QRS) has been developed that has demonstrated theoretically the harmonic signal is approximately equivalent to the product of the electron wave packet amplitude and the photorecombination cross section [3]. Since the photorecombination step is related to the conjugate of the time dependent dipole moment in photoionization, energy dependent spectroscopic features observed in photoionization cross sections are present in the harmonic signal [57,87,89]. Taking this a step further, it should be possible to extract information related to the photorecombination cross section from experimental HHG data. However, we need to know which experimental conditions to use for performing this extraction, which is the crux of this dissertation. While such extractions have been attempted previously [25,57], there are no established procedures under which the direct extraction of photorecombination dynamics from HHG spectra for the purpose of comparison to photoionization cross sections is valid. There are two primary reasons this extraction has not been realized. First, the harmonic envelope can be changed dramatically depending on the macroscopic conditions [23,28,90]. Secondly, it is possible for electrons from more than a single orbital to participate in the HHG process, particularly from molecules which are typically characterized by relatively closely spaced outermost orbitals [27].

This chapter discusses the results from an experimental (supported by theory from collaborators) study of HHG from SF_6, with the goal of understanding how molecular scattering

effects are manifested in the HHG spectra of complex molecules. SF_6 was chosen as the initial sample to investigate the relationship between the photoionization cross section with the photorecombination cross because it is a molecule with intense shape resonances and whose photoionization dynamics have been investigated extensively [43,91-97]. The specific aim is to ascertain the conditions and procedures necessary to extract photorecombination data directly from HHG spectra. This resonant trapping is extremely sensitive to the potential responsible for the quasi-binding of the photoelectron[36], which may be impacted by the strong field responsible for tunnel ionization. As noted in Chapter 1, shape resonances [56,57] and Cooper minima [22,25,53-55] have been previously shown as photoionization features that will emerge in HHG spectra. However, these previous studies do not provide a systematic procedure that would allow one to extract quantitative photorecombination parameters (e.g., cross section curves) from HHG spectra nor the conditions under which a direct comparison to cross sections is valid. A systematic study on the HHG from SF_6 is presented here and includes the observation of features in the harmonic spectra that are attributed to shape resonances.

Calculations utilizing the QRS were conducted by collaborators in order to confirm the effect of shape resonances The QRS method [3] is a variant of the strong-field approximation (SFA), and has proven to be an excellent tool for analyzing HHG from atoms and molecules. Some of the recent studies employing the QRS model include analysis of HHG from N_2 [57], O_2 [3], CO_2 [3], CS_2 [55], and CCl_4 [55]. By introducing newly available scattering states for the photoelectron wavefunction [98], a superposition of molecular states is the most plausible explanation for the harmonic spectrum measured.

The main goal of this chapter is to show that despite the intricate details of the measured harmonic spectrum and the photoionization dipole element in SF_6, the experimentally observed features are extremely resilient to a very broad range of macroscopic conditions. A direct comparison with the theory allows the study of how shape resonances in SF_6 are manifested in HHG, how they respond to macroscopic effects, and how this influences the energy dependence of the recombination matrix element.

4.2 Results

The section will discuss the results of measuring the HHG spectrum as a function of focal position and laser intensity. All results in this chapter were collected using the cw gas jet and HITS laser system outlined in Chapter 2. The influence of the position of the gas jet on the observation of long and short trajectories is considered first and a brief review of the results in Chapter 3 will highlight the differences observed between the spatial profile of harmonics generated from Ar and SF_6. Figure 4.1 displays raw harmonic images taken at focal point position of (-) 3 mm and peak intensity of 3.3×10^{14} W/cm^2. In the case of Ar, we see a combination of long and short trajectories at all (-) positions with purely short trajectories at positions 5.5 mm on the (+) side and beyond, a result that does not necessarily contradict previous results [12,24,33], but a key difference being there is no set of experimental conditions at which purely long trajectories are observed and the short trajectories are always more intense than the long. In the case of SF_6, we observe purely short trajectories at all lens positions. This can be attributed to the use of a gas jet with a length (0.15 mm) an order of magnitude smaller than the Rayleigh length which alters the effect of phase matching changes

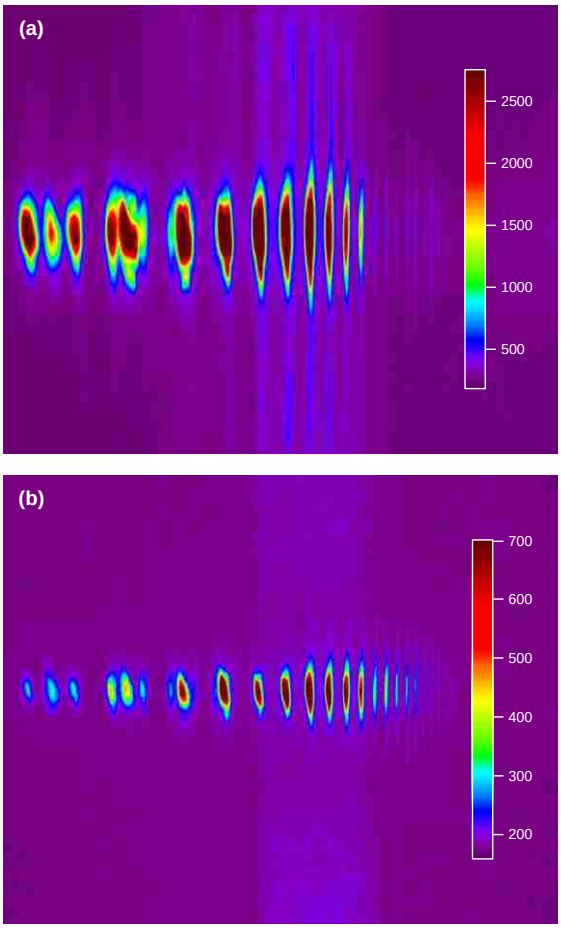

Figure 4.1: Raw HHG images from Ar (a) and SF_6 (b) at (-) 3 mm and 3.3×10^{14} W/cm^2. The x and y axis are pixels and the harmonic order increases from left to right. The color scale reflects the difference in harmonic conversion efficiency between the two gases.

such that the long trajectories do not contribute substantially to the harmonic signal. The lack of long trajectories from SF_6 compared to their presence in Ar can be explained by the significantly lower harmonic conversion efficiency as evident in the color scale of Figure 4.1.

One source of error in the collected date evident in Figure 4.1 is the broad scattering effects in the center of the image. This noise is likely scatter from the deteriorating slit in the spectrometer and can be significant at high intensities. Since the scatter is the result of the fundamental beam and the harmonics hitting the slit and diffracting onto the detector, this effect cannot be eliminated in the background subtraction process. The lack of long trajectory

contributions in the SF_6 spectra, however, renders the majority of the vertical pixels irrelevant to the determination of the overall harmonic spectrum. Thus, every image in this report is cut from five hundred to one hundred vertical pixels prior to vertical pixel integration. This effectively removes any contributions from long trajectories in Ar and the scattering in both samples. This allows the discussion of the recombination dynamics to focus on short trajectory contributions and neglect contributions from the more complex long trajectories.

Figure 4.2 shows HHG spectra for SF_6 (panels (a) and (b)) and Ar (panels (c) and (d)) at different focal point positions with a constant peak intensity of 4.0×10^{14} W/cm^2. Both the Ar and SF_6 spectra were obtained under identical macroscopic conditions. For SF_6, there are three salient features: a minimum at H17 and maxima at H15 and H21. The key spectroscopic feature in the Ar spectra is the broad minimum, centered on H33, and spanning from H29 to H37. In the case of Ar, the broad minimum has been previously identified as a Cooper minimum [22,52,87], though its presence in the current work is far less dependent on phase matching conditions than previously reported with a gas jet [22]. At this intensity, we are able to observe this broad minimum at all (-) lens positions and up to (+) 3.5 mm, though it narrows at ca. (+) 3.00 mm to H35. The minimum at H17 and the maximum at H15 in the SF_6 data are present in every combination of laser intensity and lens position, while the maximum at H21 is only present in the (-) positions at this intensity. In both SF_6 and Ar, the lack of certain spectroscopic features at large (+) values may be a result of poor phase matching resulting in a decreased harmonic cutoff and may or may not be due to complication in the recombination process.

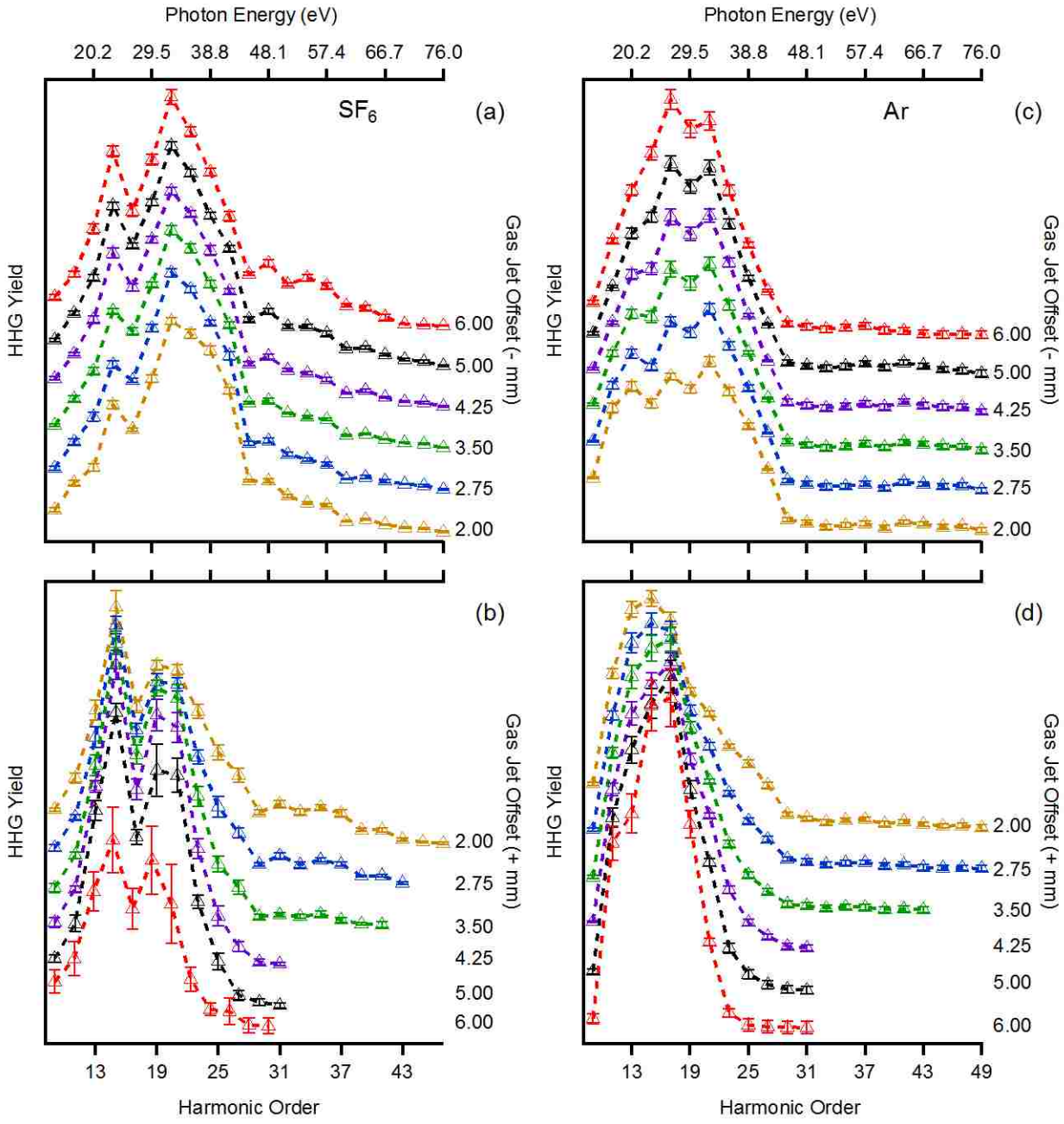

Figure 4.2: Position dependent HHG envelopes as a function of focal position for SF_6 (left column) and Ar (right column). The numbers next to each line on the right represent the distance of the focal point from the center of the gas jet as determined by the ion signal, with (-) positions in the two upper panels and (+) position in the two lower panels. The laser intensity for all plots was 4.0×10^{14} W/cm^2. The Cooper minimum is shallow in (c) and (d), but it is clear when using a log scale.

In addition to focus position, we changed the laser pulse energy by rotating a half wave plate in front of a linear polarizer. By changing the intensity in this manner, we maintain the spatial profile of the laser beam. Harmonic spectra for SF_6 [panels (a) and (b)] and Ar [panels (c) and (d)] are shown in Fig. 4.3 as a function of intensity. In the figure we plot harmonic spectra for intensities ranging from 1.7×10^{14}W/cm^2 to 4.8×10^{14} W/cm^2 with the focal point located 2.75 mm before and after the center of the gas jet. It should be noted that SF_6 and Ar have almost identical ionization energies (15.7 [91] and 15.9 [7] eV, respectively) and therefore, we anticipated that if phase mismatch plays an issue, it will affect both species in the same manner. The overall shape and the inflection point centered on H17 and the peak centered on H15 do not change with peak laser intensity at any lens position which strongly suggests the inflection and the enhancements are the result of an interaction in the photorecombination step. It is important to note that the inflection in the Ar spectra is absent and the enhancement in SF_6 spectra is diminished in the (+) lens positions, with a notable exception being the enhancement at H21 of the SF_6 spectrum at 4.8×10^{14} W/cm^2. It should also be noted that while the enhancement in (a) is maintained at all intensities, the minimum at H17 levels out as the intensity is increased.

4.3 Discussion

In previous articles comparing the photorecombination cross section to the photoionization cross section, the focus has been calculations for the wave packet to account for the phase inherent in the HHG signal [3,99,100]. Extending these calculations to polyatomic molecules such as SF_6, however, presents serious complications avoided for atomic targets. The

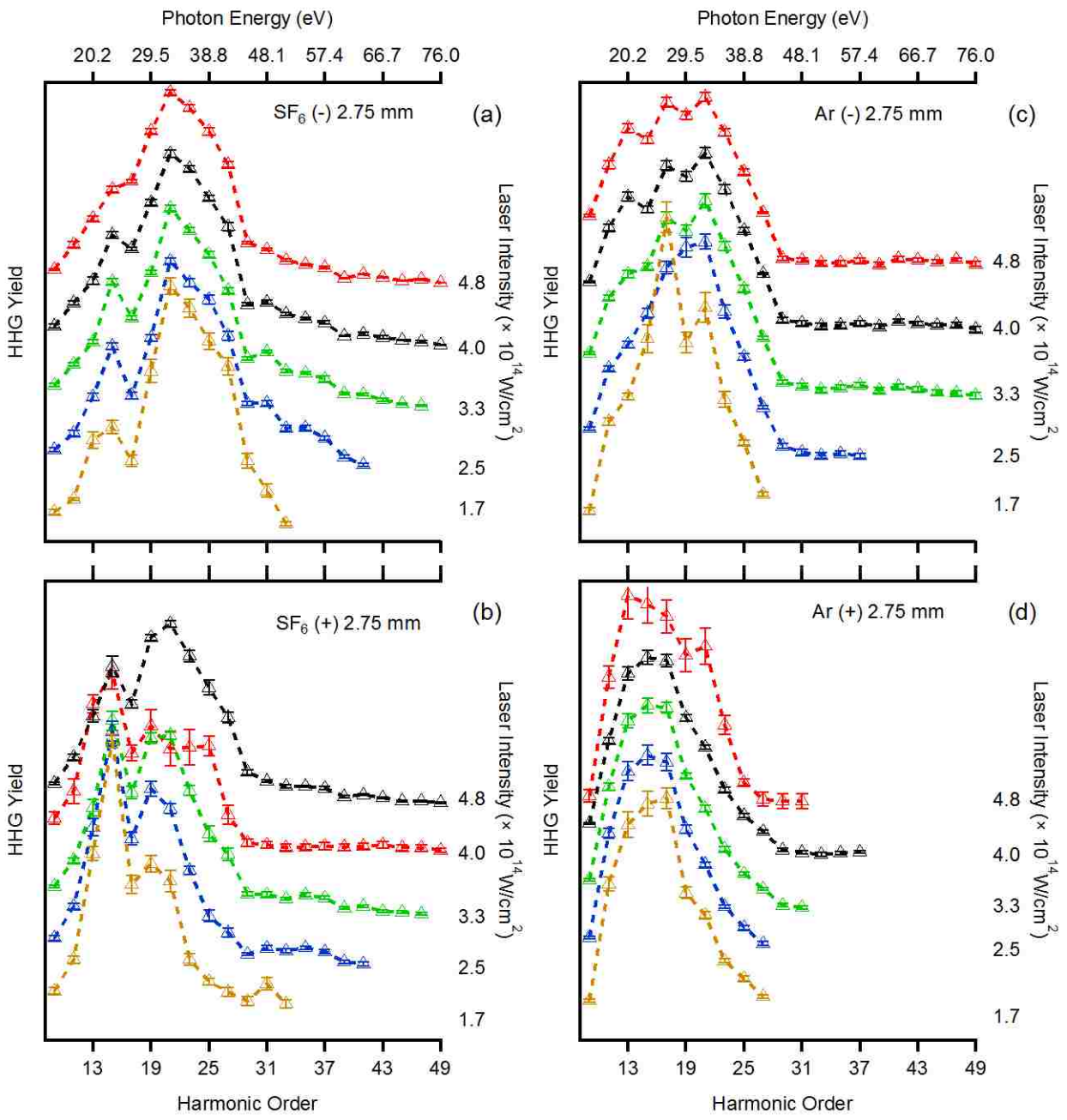

Figure 4.3: Intensity dependent HHG spectra for SF_6 (left column) and Ar (right column) with the focal position at (-) and (+) 2.75 mm relative to the center of the gas jet. Very small changes are observed in (a) and (c) save for the decrease in the harmonic cutoff. The harmonic order at which the minimum in Ar and maximum in SF_6 do not change with laser intensity and the minimum at H17 in SF_6 is present in all spectra.

effect of shape resonances on HHG, specifically, has not been determined for larger targets with a complex electronic distribution. Changes in phase matching conditions, particularly in aligned systems, can affect the yield of individual harmonics[90], complicating the aim of systematically correlating photoionization dynamics and HHG spectra. To quantify an optimal set of phase matching conditions, i.e. experimental parameters at which cross section data is most simply extracted from HHG spectra, current results for the HHG of Ar and SF_6 are compared with previous results from photoionization dynamics studies. The comparison between a raw harmonic spectrum and the total photoionization cross section of Ar[7] is shown in Fig. 4.4(a). While the overall spectrum changes very little with large changes in focal point position, the best agreement with the photoionization cross section is at (-) 2.75 mm and with a peak intensity of 4.0×10^{14} W/cm^2. Argon has a well-known Cooper minimum between 40 and 50 eV in photoionization cross section literature, shown here to be centered on H33, or 51 eV. The center of the minimum presented here for the Ar data is within 3 eV of the previously reported minima using HHG [22,52,53], results that were also blue shifted relative to results in the photoionization cross section. In Fig. 4.4(b) we also show a comparison between the partial photoionization cross section of the HOMO [43] and the harmonic yield of SF_6 under identical experimental conditions. There are two noticeable shape resonances in the partial photoionization cross section at 27 and 33 eV, the latter of which matches reasonably well with the harmonic peak. The peak at 27 eV lines up closely with the minimum observed in the harmonic spectra, but as will be discussed later in this section, the two are likely from different spectroscopic features.

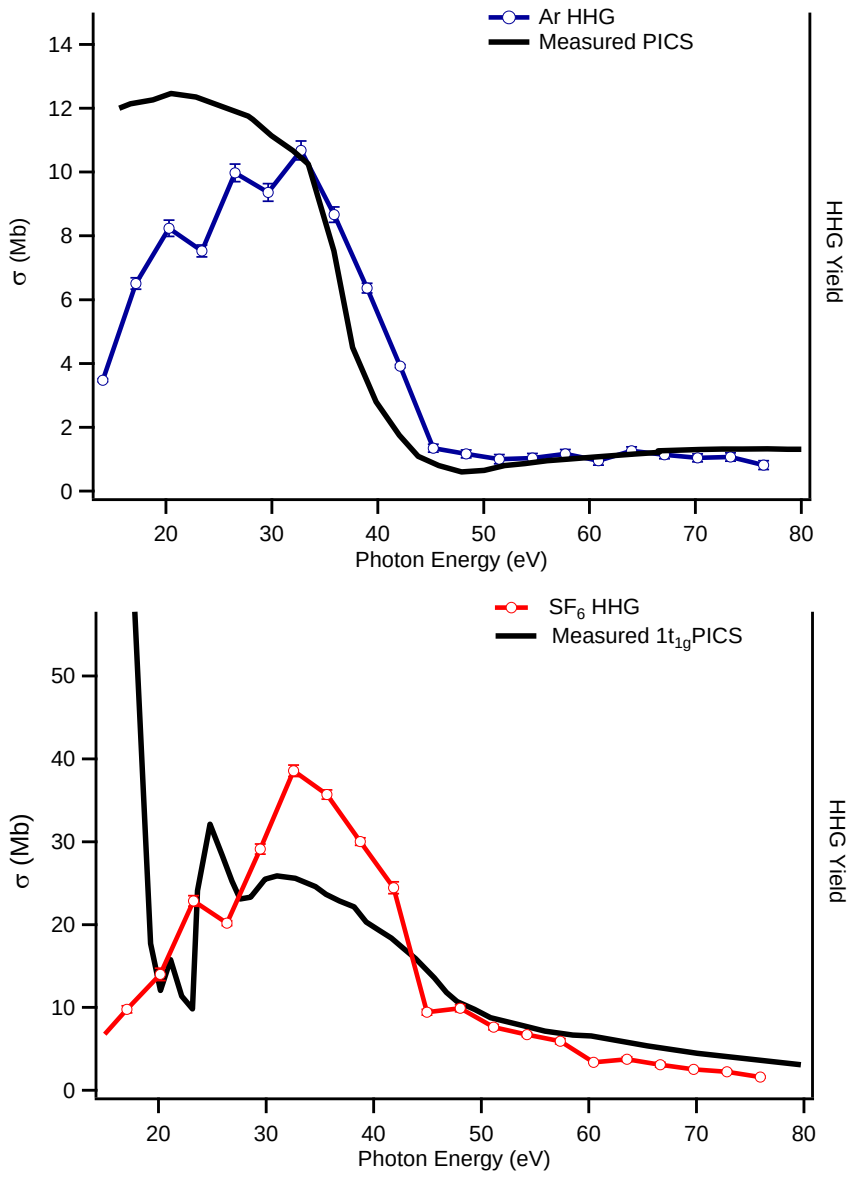

Figure 4.4: Current experimental HHG spectra of Ar and SF_6 compared to the total photoionization cross section for Ar and the partial photoionization cross section from the HOMO for SF_6. The HHG spectra were taken at a focal position of (-) 2.75 mm and an intensity of 4.0×10^{14} W/cm^2.

While it is difficult to establish a quantitative agreement between the photoionization cross section and the harmonic yield of SF_6, some conclusions can be extracted from the present data. For example, the persistence of the shape of the harmonic envelope regardless of

ionization condition, specifically the minimum centered on H17 and the peak centered at H15, suggests that the behavior is independent of changes in the ionization step and thus attributable to the recombination step. When the focus is located a few mm in front of the center of the gas jet, the single atom or molecule harmonic phase is partially cancelled by the Gouy phase near the focus of the laser [89,101], which in turn flattens the phase of the wave packet, making it less susceptible to changes in the laser intensity [87]. These are the positions at which the extraction of photorecombination dynamics from the harmonic spectra is most realistic. A focal position of (-) 2.75 mm is utilized for the remainder of this chapter for comparisons to the theoretical models. Even though the short trajectory contributions vary little with respect to changes in laser intensity, the spectra that are the easiest to compare to the current theory are at intensities bordering the point of HHG saturation (in this case 4.0×10^{14} W/cm^2).

The photoionization dynamics of SF_6 have been studied extensively [43,91-97], making a comparison to the present results straight forward. Based on the overall photoelectron spectra, the agreed upon outer valence orbitals are as follows: the HOMO is a $1t_{1g}$ orbital with an ionization energy of 15.7 eV, followed by $5t_{1u}$, $1t_{2u}$, $3e_g$, and $1t_{2g}$ orbitals with ionization energies of 16.9, 17.2, 18.3, and 19.7 eV, respectively. From these there are four commonly accessed shape resonances of a_{1g}, t_{2u}, t_{2g}, and e_g symmetries. The first of the shape resonances is consistently reported as below threshold, the last two are consistently reported above threshold, but there is some discrepancy regarding the resonance with odd parity, t_{2u}. If the resonance placed between 5 and 12 eV above threshold is designated as the t_{2g} resonance, its

presence in the partial ionization cross section from the $1t_{1g}$ orbital is indicative of a symmetry forbidden transition as observed in much of the early work on this topic [43,91-93].

In order to clarify the shape resonant effects observed in our experimental data, the effects of shape resonances on the HHG spectrum are investigated using QRS theory. The QRS calculations were performed by collaborators within the Texas A&M University Dept. of Chemistry, with Jobin Jose performing the bulk of the calculations. Theoretical photoionization cross sections were first calculated using the Schwinger variational theory within the STEX approximation and then the cross sections were used to calculate the HHG yield. The theoretical HHG yield from the HOMO ($1t_{1g}$) of SF_6, exhibits a peak centered at 36 eV (H23) reflective of a similar peak in the theoretical cross section. This behavior is attributed to the strong shape resonance present in the $1t_{1g}$ photoionization cross section. Symmetry resolved analysis (also performed by collaborators) shows that the resonance has a t_{2u} nature and enhances the HHG spectra near H23, a result that is in agreement with more recent studies [94,95,97], thus avoiding the discussion concerning a symmetry forbidden transition. This observation is in qualitative agreement with features of the experimental HHG yield, in which a peak is centered on H21.

With a laser intensity between 1.7 and 5.2×10^{14} W/cm^2, tunneling is the main mechanism for ionization[6], but multiphoton ionization also contributes. The nature of both of the processes indicates that the ionization should primarily originate from the HOMO; however, lower lying orbitals also contribute in molecules with energetically close valence orbitals. Thus in the case of SF_6, which has five valence orbitals within 5 eV of each other, multiple orbitals must be considered. In considering the resonant effects in the lower lying orbitals, the $5t_{1u}$

subshell cross section has a sharp shape resonance with e_g symmetry, which falls in the energy region of H25 (~38 eV) [43]. This resonance is less evident in the experimental photoionization cross section [91,92], therefore the e_g resonance will probably not have a significant contribution to the HHG yield. Portions of each orbital match acceptably well with the raw harmonic data.

Comparing the HHG spectra directly to photoionization cross sections is not in and of itself a satisfactory method of determining the contributions of multiple orbitals and shape resonances, however, the comparison may be useful in elucidating the impact of photorecombination dynamics from several orbitals on the total harmonic signal. In Fig. 4.5, we compare our experimental results at a lens position of (-) 2.75 mm with a laser intensity 2.0×10^{14} W/cm^2 to the calculated QRS HHG spectra at the same intensities for the HOMO, HOMO-1, HOMO-2, and HOMO-3 in order to qualitatively compare features from each orbital with the overall harmonic spectrum. The calculated photoionization cross sections based on the STEX model are included for reference. There are three distinct features in the HHG spectrum that can be used as guideposts for comparison to the theoretical results. The shape resonant effect discussed earlier at H21 is close to the shape resonance observed in the calculated results from the HOMO, with an assigned t_{1u} symmetry, while the maximum at H15 corresponds closely to a strong shape resonance with t_{2g} symmetry. The most obvious effect is the minimum at H17 that is resistant to large changes in phase matching. As shown in Figure 4.5, a similar minimum is displayed in the QRS2 results from the HOMO-3 and is confirmed as the result of a shape resonance with t_{1u} symmetry. The minimum in the experimental results is either the result of this shape resonance, or more likely, due to a non-descript minimum between

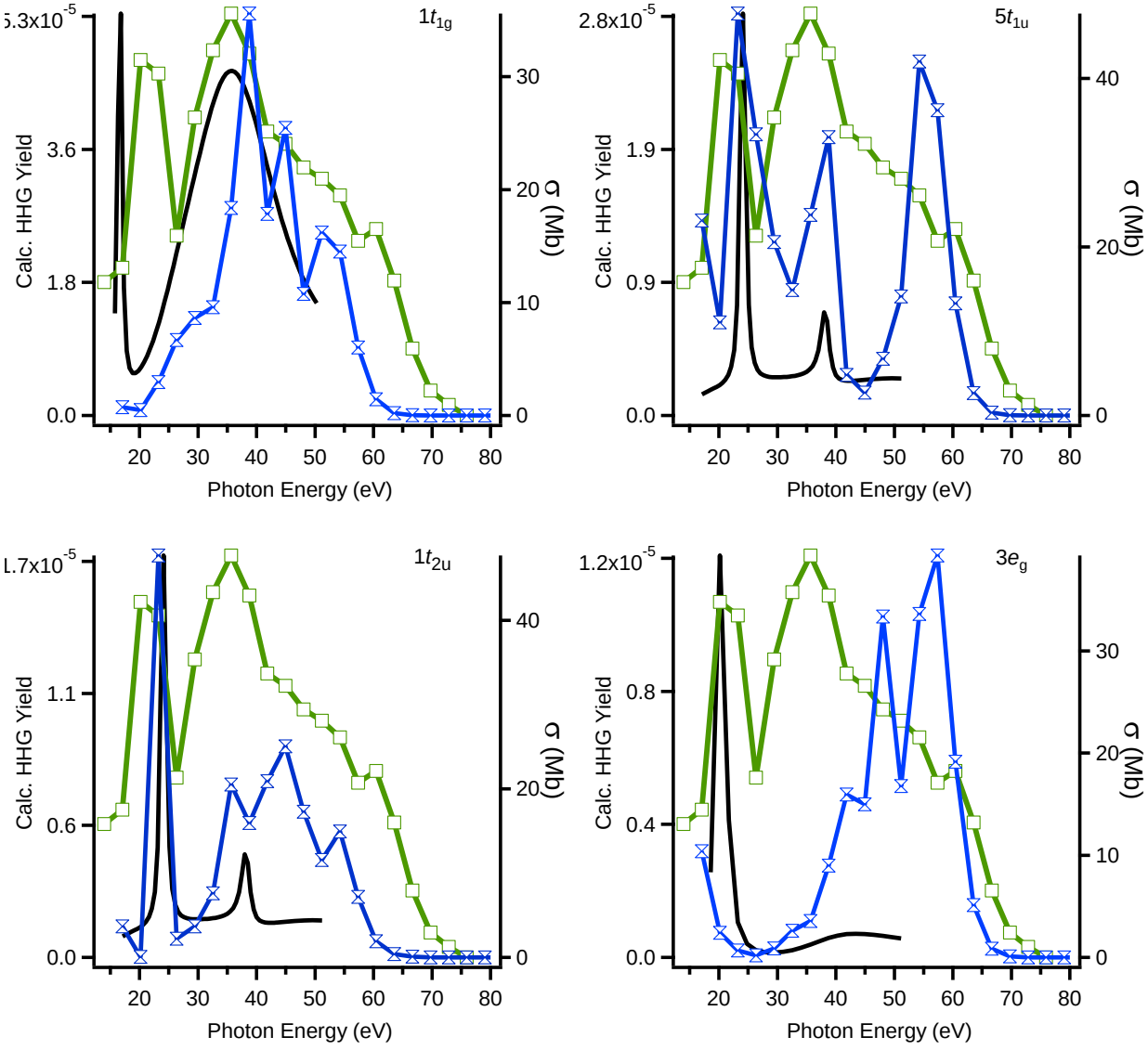

Figure 4.5: Comparison of SF_6 HHG spectra (green squares) at 2.0×10^{14} W/cm^2 to calculated HHG spectra (blue bows) from QRS2 for four valence orbitals. The PICS results from the Schwinger variational theory within the STEX approximation is presented as a solid black line for reference.

two maxima. The latter possibility is statistically more probable due to the reduced recombination cross section values present in the HOMO-3 versus the other presented valence orbitals. It is possible that a portion of the harmonic envelope stems from one orbital while the rest is a result of contribution from another orbital, as suggested in the case of SF_6 by Ferre *et*

al. [102], though the presence of the shape resonance in the higher order harmonics is more pronounced and more accurately described by the QRS theory in this case. A more accurate description of this multi-orbital phenomenon may be that each harmonic order is comprised of contributions from multiple orbitals, but strong dynamical processes in the recombination cross section of an individual orbital have a more significant impact on HHG yield at the specific energy range than structureless orbital contributions in highly symmetric molecules with closely packed orbitals. The overall strength of the HOMO contribution in the QRS theory, combined with the broad nature of the resonance from the HOMO may effectively wash out some of the resonance, preventing it from being observed at all lens positions. This is in contrast to the maximum at H15 and minimum at H17 that are observed at all combinations of lens position and laser intensity.

The nature of these resonant effects is further explored by measuring the non-normalized ratio H17 to the average value of H15 and H19 and the ratio between H21 and H15 as a function of laser intensity. The minimum at H17 is evidence of a shape resonance and as the value related to the dip at H17 increases, the shape resonant effect at H15 or the resonant effect at H17 becomes more significant. Likewise, when the ratio between H21 and H15 is greater than 1, we label the enhancement as evidence of shape resonance at H21 as the plateau behavior is clearly different from early descriptions. The maximum of these ratios as a function of laser intensity is plotted in Fig. 4.6 along with the lens position at which the corresponding maximum ratio is realized. In Fig. 4.6 (a), the ratio related to the dip at H17 is plotted versus laser intensity, and although the maximum value does not experience significant change, the lens position of the maximum value varies from (-) 3.25 mm to (+) 1 mm. Fig 4.6 (b)

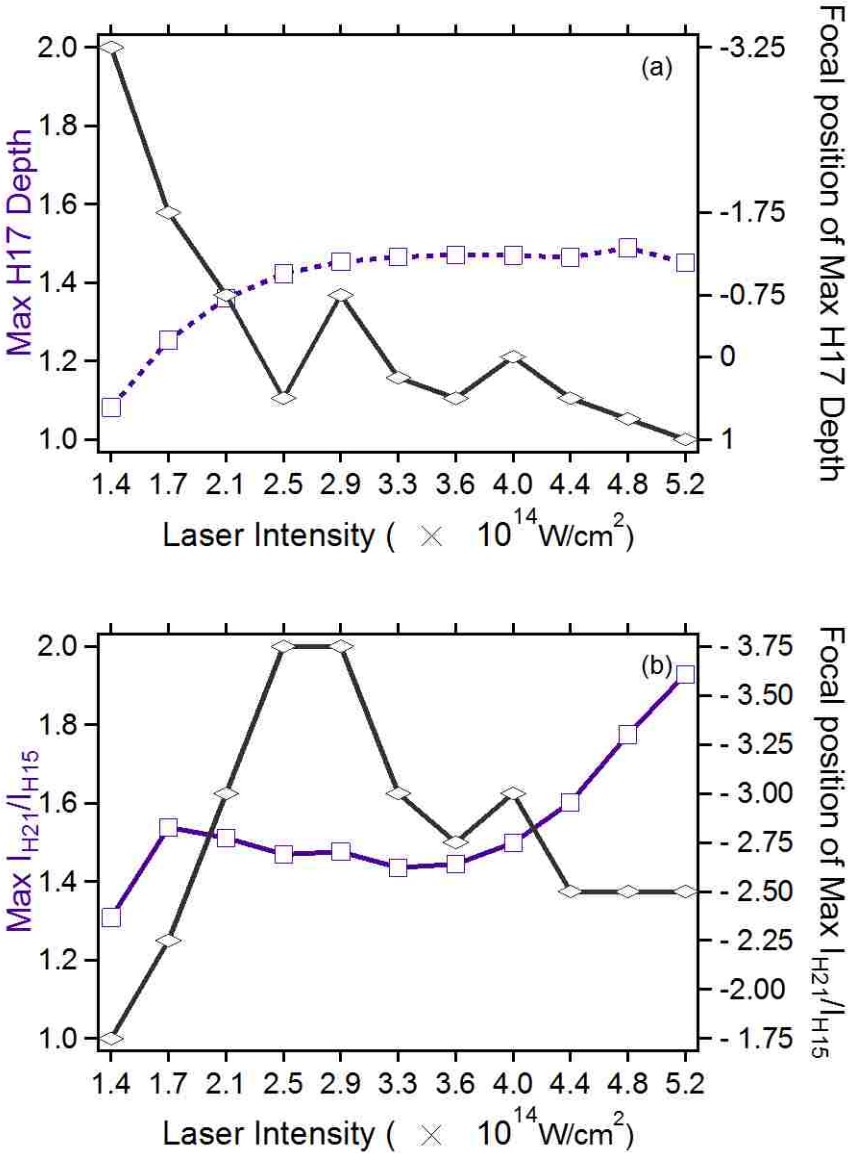

Figure 4.6: A measure of the impact of a change in phase matching conditions on the appearance of shape resonances in the SF_6 HHG spectra. The max value of the dip at H17 (a) is calculated by dividing the average intensity of H15 and H19 by the intensity of H19 while (b) plots the maximum value of the ratio of H21 to H15. The intensity dependent ratios are represented by the purple squares and the left axis while the intensity dependent locations of the maximum ratios are represented by the black diamonds on the right axis.

shows the maximum value of the ratio of H21 to H15. This lens position varies from (-) 2.25 to (-

) 3.75 mm. The position becomes stable above 4.0×10^{14} W/cm^2 even as the ratio continues to

increase. Beyond this intensity, the harmonic signal is saturated as evidenced by the fact the cutoff does not increase with intensity.

In the case of each shape resonance, the variance of the behavior can be explained by further considering the process by which a shape resonance exists in the continuum. In order for the electron to "escape" the quasi-bound state, it must tunnel through the barrier which invokes a phase shift of π [38]. If the shape resonance effect in HHG mirrors the effect in photoelectron spectroscopy, this same phase shift will occur as the electron recombines with the parent ion. Shape resonant trapping in HHG was previously described as a four-step process whereby the electron is temporarily trapped between acceleration and recombination [59]. This phase change should be evident in the phase of the generated harmonic in the region of a shape resonance and thus the resonant effect may be altered depending on the phase matching conditions. This is most clearly observed in the enhancement in the HHG spectrum at H21 that continues to increase in intensity beyond the HHG saturation limit.

Each resonance effect originates in a different orbital and has different symmetry. For this reason, each resonance may respond differently to changes in phase matching conditions. However, the apparent competition between the two effects shown in Fig. 4.6 may provide some clarity on which orbital is responsible for the harmonic signal. The shape resonances centered on H15 and H17 are narrow while the resonance centered on H21 is broad. As the intensity of the latter increases, the minimum at H17 is reduced and at higher intensities when the peak at H21 is its most intense, the maximum depth at H17 is shifted to (+) focal positions at which the enhancement is missing entirely. This is indicative of the resonance from the HOMO having a bigger impact on the overall harmonic yield than the lower energy resonances

from the lower lying orbitals. This suggests that although photorecombination dynamics from multiple orbitals contribute to the HHG from SF_6, the HOMO is the primary of source of recombining electrons.

Chapter 5: Elliptical Dependence of Molecular HHG

5.1 Introduction

The three step model of HHG accurately predicts the location of the harmonic cutoff and the characteristic behavior of harmonics; however, the theory was developed for the case of a linearly polarized driving laser. In this chapter, the discussion is extended to the case of a driving laser with small ellipticity. This provides an additional experimental "knob" with which to probe HHG in complex systems as it alters the path of the electron in the field. This chapter examines the effect of increasing ellipticity on the HHG from SF_6 at multiple focal positions and laser intensities.

In the classic three step model, the electron wave packet is associated with the electric field of the laser following tunnel ionization with zero kinetic energy in the direction parallel to the field. It is then driven away from and back to the parent ion. The theory of harmonic generation from an elliptically polarized source was addressed early with respect to the history of the HHG community [103-106] and will be described here briefly. The path of the electron wave packet is perturbed due to the partial perpendicular component of the electric field, which makes recombination with the parent ion classically forbidden. Recombination becomes possible only when there is an equally strong counter momentum in the direction perpendicular to the main axis of the laser to counter the effect of the added ellipticity. As the ellipticity of the fundamental is increased, the probability of recombination decreases owing to the Gaussian dependence of the ionization probability on the transverse velocity necessary for recombination and the modeling of the recombination suggests that there is a Gaussian decrease for recombination [107].

This exponential decrease in harmonic conversion efficiency has been utilized in the development of methods to isolate attosecond bursts through a time dependent polarization gating scheme [104,108-110]. This is accomplished by creating an ultrashort pulse with a time dependent polarization such that recombination is only statistically possible for a short section of the pulse. Since HHG is characterized as producing two attosecond pulses per laser cycle, the reduction of cycles capable of producing harmonics can isolate the attosecond bursts. The use of a elliptically polarized laser has also been utilized for the production of elliptically [110-113] and circularly [114] polarized harmonics.

This chapter examines the potential of using variable elliptical polarization as a means to probe photorecombination dynamics in polyatomic molecules. Though the single molecule response can be separated from the macroscopic effects [3], the energy dependent PRCS can only calculated or extracted from the HHG spectrum at zero ellipticity and the effect of the angular asymmetry parameter is not known [18]. Adding ellipticity to the fundamental alters the recombining angle of the electron and prevents harmonic generation in the classical sense, and requires an initial momentum counter the direction of the ellipse. The momentum required to compensate for the elliptical nature of the fundamental varies with photon energy and is dependent on the spatial symmetry of the orbital the electron originates from [18]. By measuring the elliptical dependence, we hope to establish parameters for extracting angular information related to the photorecombination process. No model has been established for the elliptical dependence of HHG from molecular targets. This work will serve as a guidepost for the development of models by examining the elliptical dependence of the overall harmonic yield and the impact of varying ellipticity on photorecombination dynamics in SF_6.

5.2 Methods

The effect of elliptical polarization on the HHG from SF_6 was probed by recording the harmonic spectrum as a function of ellipticity at seven different focal positions and three different intensities. At each combination of focal position and intensity, the ellipticity of the beam was altered by rotating a half wave plate in front of a quarter wave plate. This optical order is used to insure the axis of polarization remains unchanged throughout the experiment. As the half wave plate is turned by 1^o, the ellipticity in the beam is altered by 2^o. The degrees are converted to radians and used to characterize the ellipticity of the fundamental laser throughout this chapter. This can also by described as the ratio between the relative intensities of the two electric fields responsible for the polarization, or E_x/E_y.

5.3 Results

The elliptical dependence is shown qualitatively in Figure 5.1. This figure displays contour plots of ellipticity versus harmonic order at a focal position of (-) 2 mm. Spectra were taken at 0 ellipticity (linear polarization) and then at 27 different elliptical values in the positive and negative polarization direction. Note that data points are filled in to create a solid contour plot in order to increase the readability of the figure. From Figure 5.1, it is clear the minimum at H17 and the maxima at H15 and H21, discussed in the previous chapter, are present in the linear polarization spectra and generally persist with an increase in the ellipticity of the fundamental. For the purposes of fits that will be included in the discussion section, it is important to note that the elliptical dependences appear symmetric with regards to the sign of the elliptical polarization.

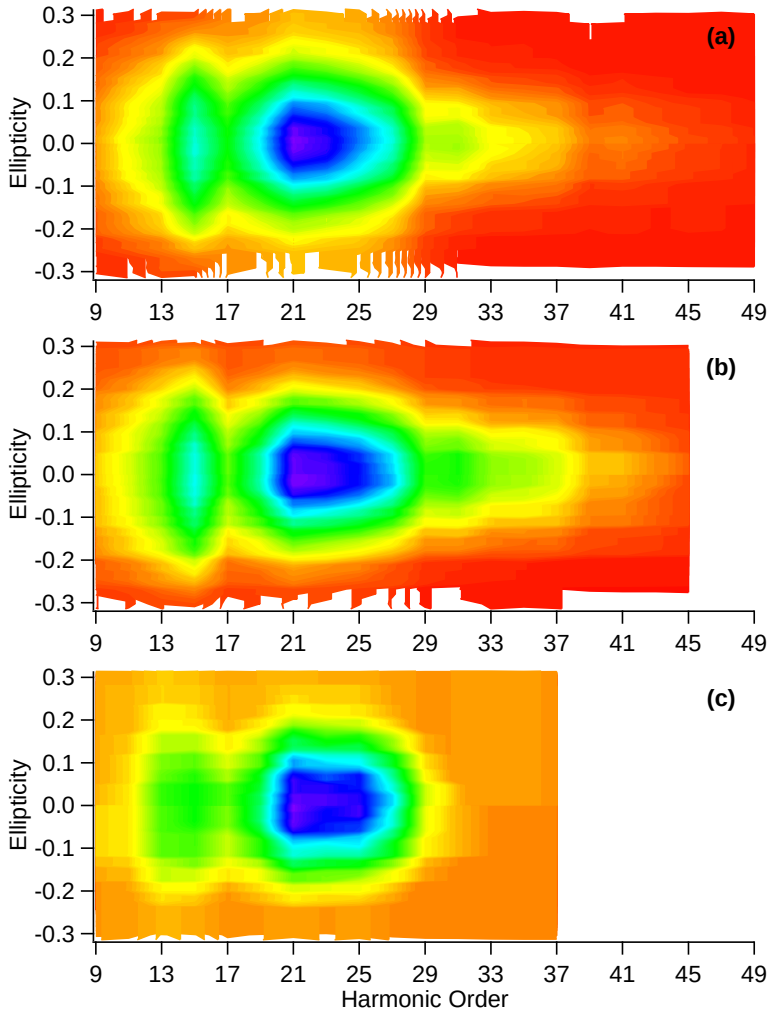

Figure 5.1: The elliptical dependence of harmonics from SF_6 at 5.2 (a), 4.0 (b) and 2.7 $\times 10^{14}$ W/cm^2 (c). All three data sets are taken from measurements when the focal point is (-) 2 mm from the center of the gas jet. The color scale is relative in each panel and set such that the features of interest are easy to observe.

Each of the horizontal slices in Figure 5.1 can be extracted and represents a harmonic spectrum at a given ellipticity. Eleven of the fifty-five total ellipticities, including zero, are displayed as harmonic spectra in Figure 5.2. Negative ellipticities are presented as hollow symbols and their positive counterparts are presented as solid symbols. Very small deviations are observed between the positive and negative portions, again confirming the symmetry in the experiment about the polarization axis. One important feature is the apparent broadening of the minimum centered on H17 as the ellipticity is increased. At the highest value of ellipticity,

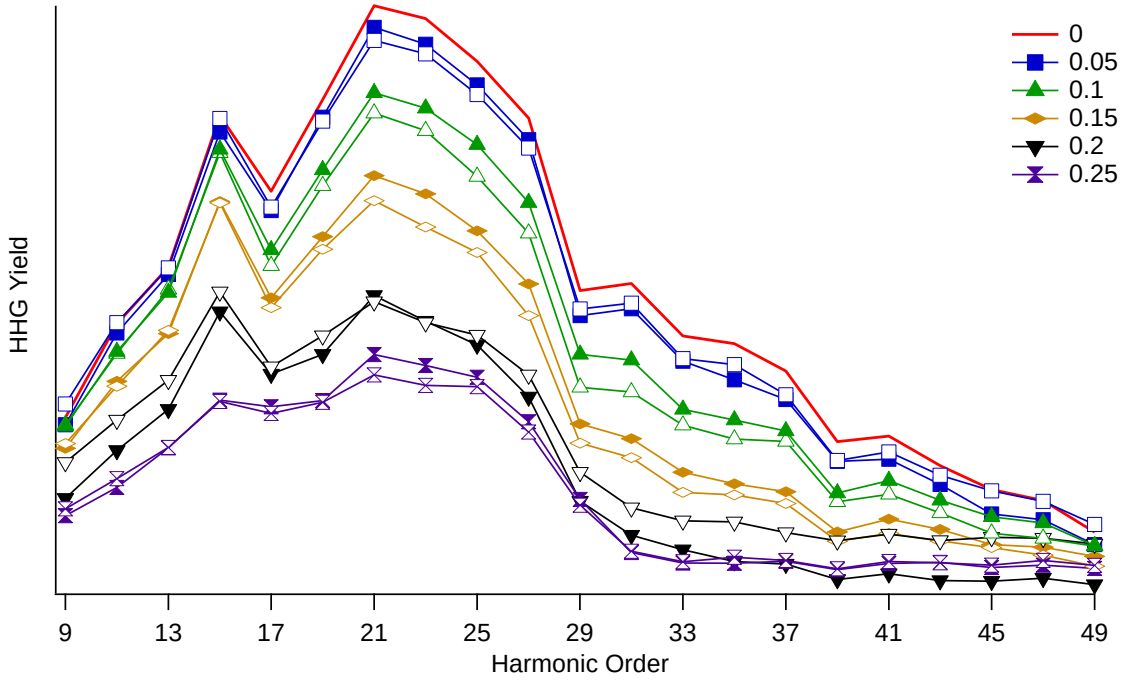

Figure 5.2: Harmonic spectra extracted from Figure 5.1 (a). Positive ellipticities are presented as solid symbols while the negative ellipticities are hollow. The relative intensities between the equal and opposite ellipticities are close enough to consider the experiment symmetric about the linear polarization condition.

for example, the minimum extends to the point that H15 is nearly equal to H19, even though the maximum at H21 remains.

The spatial distributions of individual harmonics are plotted at several elliptical values in Figure 5.3. Raw images of H13, H17, and H21 are presented at three different ellipticities. In this case and throughout this chapter, zero ellipticity will refer to conditions of linear polarization. As can be seen in Figure 5.3, as the ellipticity is increased the overall profile of the harmonics experiences very little deviation from the linear case outside of an increase in contribution of background due to lower harmonic intensity. Previous studies have concluded that large

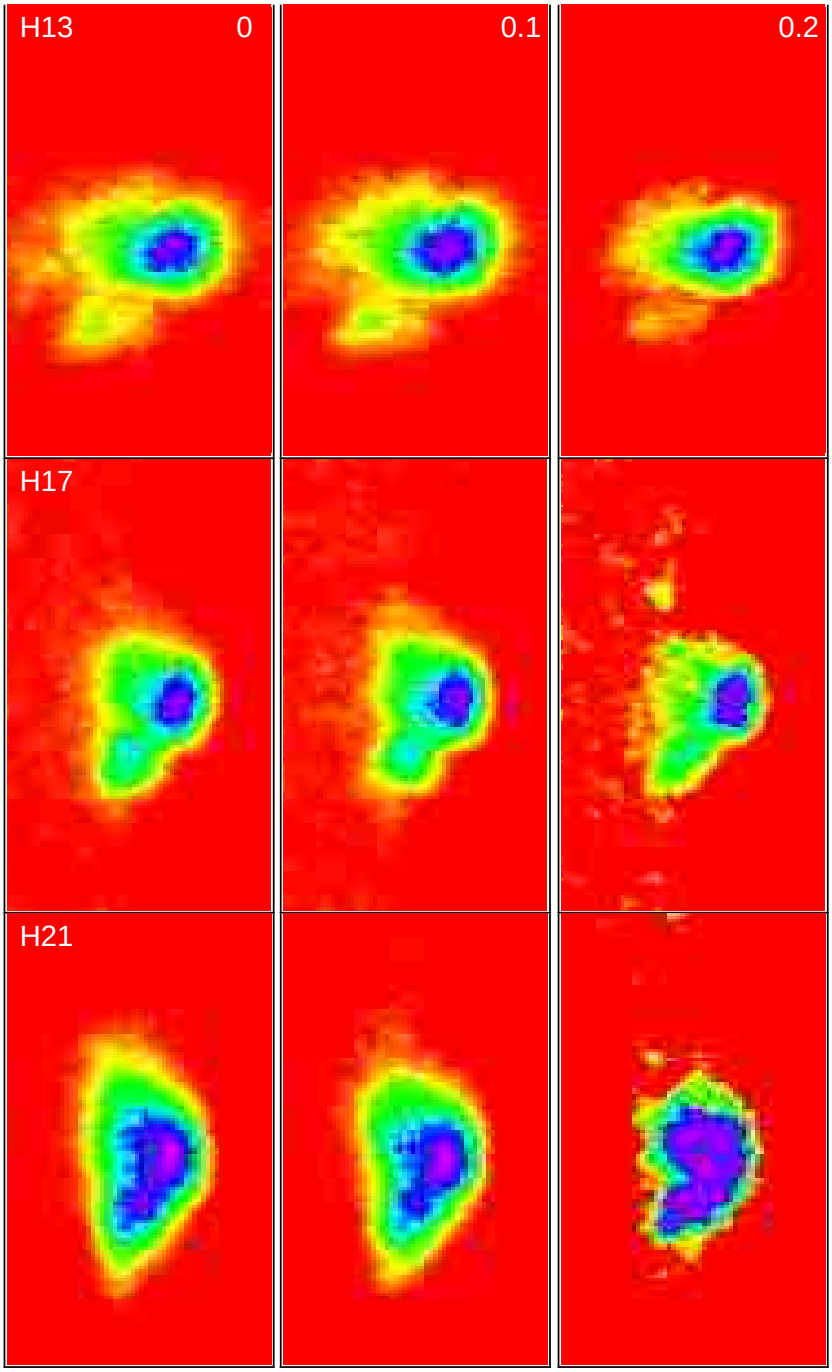

Figure 5.3: Raw images of H13, H17, and H21 from SF_6 at (-) 2 mm lens position and an intensity of 5.2×10^{14} W/cm^2 at three different ellipticities. The color scale is set such that the maximum color is 75% of the maximum pixel value and the minimum color is twice the minimum pixel value so features of interest are easy to observe. The x and y axes are pixels and each panel represents the same window size on the detector.

ellipticities favor contributions from long trajectories and the spatial profile of these harmonics is further stretched with an increase in ellipticity due to an increased spreading of the wave packet [18,115]. This may be partially explained by the observation that long and short trajectories have different ionization times which result in opposite initial transverse momenta and opposite polarizations [113]. The lack of distortion in the harmonic profile further indicates the conclusion reached in the previous chapter concerning the absence of long trajectories is valid for HHG from SF_6 and this chapter will only address the elliptical dependence of short trajectory contributions from SF_6.

5.3 Discussion

This section will discuss the elliptical dependence on photorecombination dynamics observable in SF_6, as outlined in Chapter 4 of this dissertation. From Figure 5.2, there are three dynamical effects in the harmonic spectrum of SF_6: a minimum at H17 that may be indicative of a shaper resonance and two confirmed shape resonances that present as maxima at H15 and H21. The relationship between the observation of the two resonances and changes in macroscopic properties was addressed in Figure 4.6 by measuring the change in the ratio of H21 to H15, and the ratio between H15 and H19 to H17 (the maxima and minimum, respectively). The minimum at H17 broadens as the ellipticity is increased, and while a similar effect may occur with respect to the resonances at H15 and H21, the resonances are energetically too close to isolate as they broaden. Since the minimum at H17 is evident in all combinations of focal position and laser intensity, this discussion will focus on the broadening of the minimum at H17.

The broadening of this minimum in the SF_6 spectrum is due to the change in the recombining angle of the electron. When describing recombination with a linearly polarized laser, the recombination angle of the electron with respect to the driving field is always zero because it is directly steered by the electric field. In this way, the comparison of the photorecombination cross section and the photoionization cross section is relatively simple due to the shared dipole matrix elements. The differential photoionization cross section, however, includes the photoelectron asymmetry parameter that relates the cross section to the angle between the photon source and the emitted electron. Increasing the ellipticity of the driving laser in HHG changes the recombination angle of the electron with respect to the major axis of polarization of the driving laser and may cause the asymmetry parameter to affect the photorecombination dynamics.

The Cooper minimum in Ar has been shown to broaden with an increase in driving laser ellipticity [52]. As the ellipticity is increased, contributions to the harmonic signal from dipole matrix elements at nonzero recombining angles become significant. At higher recombination angles, the center the Cooper minimum is shifted to a higher energy and thus the appearance of the minimum in the HHG spectrum is broadened as a function of ellipticity. This may be the cause of the apparent broadening of the minimum at H17 associated with a shape resonance shown in Figure 5.2.

In order to characterize the effect of this broadening and in light of the overlapping resonance centered on H21, the difference in the ratio of H17 to H19 and the ratio of H17 to H15 with respect to the linear condition is plotted as a function of ellipticity in Figure 5.4. If the value is above zero, ratio is higher than at zero ellipticity. As the ellipticity of the driving laser is

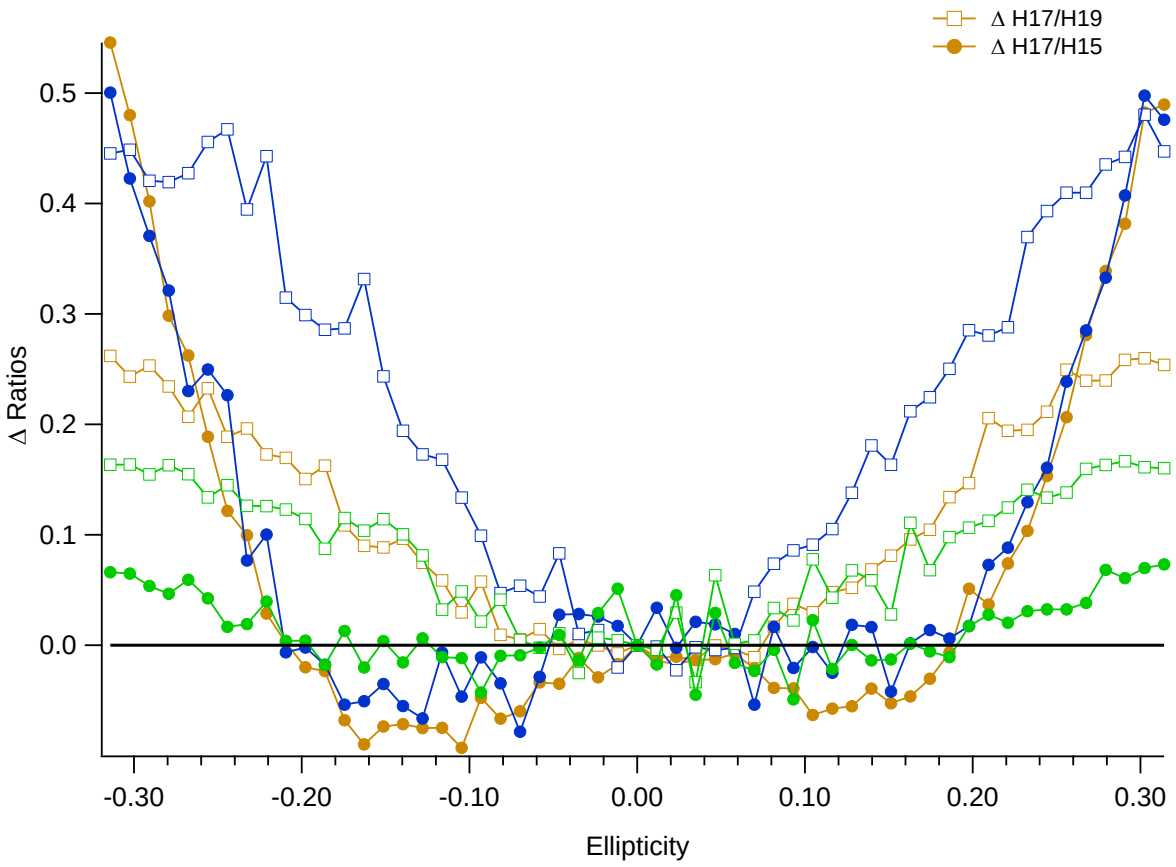

Figure 5.4: The change in the ratio of H17/H19 (squares) and H17/15 as a function of ellipticity for 5.2 (orange) 4.0 (blue) and 2.7 (green) $\times 10^{14}$ W/cm^2. The change is with respect to the ratio at linear polarization.

increased, the harmonic cutoff is decreased. As a primary result, the rate of decay increases with increasing harmonic order. It is thus expected that as the ellipticity is increased, the ratio of H17 to H19 will initially increase as the rate of decay should be greater for H19 than H17. Likewise, the ratio of H17 to H15 should decrease with ellipticity as H17 decays faster than H15. What is clear from Figures 5.2 and 5.4, however, is that at some ellipticity the broadening of the minimum at H17 causes the intensity of H15 to decay in a faster than expected manner thereby increasing the ratio of H17 to H15. This could also be interpreted as s signature of the resonance at H15 decaying as a function of ellipticity.

In order to characterize this change, the point at which the change in the ratio of H17 to H15 crosses zero (meaning that the intensity of H15 begins to decrease faster than H17) is calculated for each set of macroscopic conditions, the results of which are presented in Table 5.1. Data were taken at the focal position (+) 6 mm, but the results are omitted due to inconsistent elliptical dependencies due to poor phase matching. With a few exceptions, the positive and negative ellipticities at which the turn is centered are close to equivalent, indicating the effect is due primarily to the angle of the recombining electron. The effect is measurable at phase matching conditions at which the H21 to H15 ratio never exceeds unity, indicating the higher energy shape resonance does not dominate the signal and thus has little impact on this ratio. For example, at 4.0×10^{14} W/cm^2, the shape resonance is only measured at (-) focal positions; however, the increase in the ratio at specific ellipticities is still measurable at (+) focal positions. This confirms that the change in the ratio is due to either the broadening of the minimum at H17 or the decay of the resonance at H15 and independent of the shape resonance at H21. Given advancements in the theoretical backing of HHG, it may be possible to

Table 5.1: Elliptical values at which H15 begins to decay faster than H17 at 6 different focal positions and 3 different laser intensities. The last data point for 2.7×10^{14} W/cm^2 is omitted due to weak signal.

	5.2×10^{14} W/cm^2		4.0×10^{14} W/cm^2		2.7×10^{14} W/cm^2	
Foc. Pos.	Min Ellip	Max Ellip	Min Ellip	Max Ellip	Min Ellip	Max Ellip
4	-0.22	0.22	-0.20	0.21	-0.19	0.19
2	-0.19	0.18	-0.21	0.20	-0.19	0.19
0	-0.16	0.12	-0.20	0.19	-0.15	0.04
-2	-0.21	0.19	-0.21	0.16	-0.20	0.19
-4	-0.23	0.24	-0.23	0.22	-0.27	0.28
-6	-0.19	0.20	-0.20	0.23	N/A	N/A

interpret this effect and extract information related to the asymmetry parameter directly from HHG spectra. The ellipticity values presented in Table 5.1 indicate the point at which the minimum at H17 has approximately red shit broadened by 3 eV or at which the peak at H15 no longer impacts the overall harmonic yield.

The first part of this discussion dealt primarily in the abstract and concerned observations related to the elliptical dependence of HHG that may lead to the extraction of quantitative data. The rest of this discussion will focus on established fitting protocols that can be used to extract data presently. The dependence of HHG on the ellipticity of the beam can be considered Gaussian, such that:

$$\frac{I_{\varepsilon}}{I_{\varepsilon=0}} = \exp(-\alpha\varepsilon^2) \qquad (5\text{-}1)$$

In which Ɛ is the ellipticity and the exponential decay is with respect to the condition of linear polarization. Equation (5-1) can be used in fitting the elliptical data in order to solve for a decay rate, α. This rate of decay will vary as a function of harmonic order and the trends can be utilized in conjunction with a measurement of the polarity of the specific harmonics to confirm the existence of photorecombination dynamics. This was recently used in the case of SF_6 and Ar [102].

The goal of this chapter is to extend this discussion for SF_6 by further considering the effects which alter the rate of decay in molecules. It should be noted that all of the theory discussed in this chapter was originally intended for atomic HHG and it is not known whether or not the assumptions are valid for HHG generated from molecules in an elliptically polarized field. The rate of decay is related to the uncertainty in the momentum perpendicular to the

major polarization axis of the driving laser following tunnel ionization, $\Delta p_{\perp}^2$, which depends on the symmetry of the orbital and the ionization time, t_i. These terms are defined in equations (5-2) and (5-3), respectively[115].

$$\Delta p_{\perp}^2 = \frac{E\cos(\omega t_i)}{\sqrt{2I_p}}, \quad (5\text{-}2)$$

$$t_i = \frac{1}{\omega}\arctan\frac{1-\cos\omega\tau}{\omega\tau-\sin\omega\tau}, \quad (5\text{-}3)$$

In the preceding equations, τ is the total excursion time, showing the uncertainty of the perpendicular momentum corresponds to the duration of the wave packet in the electric field. For this reason, it is possible that the short and long trajectories will respond differently to changes in the ellipticity of the fundamental. Due to the longer excursion times, long trajectories are impacted by the ellipticity to a greater extent than the short trajectories. This can lead to disproportionate suppression of the long trajectories resulting in a slight increase in harmonic yield as a function of ellipticity[115]. The lack of long trajectories in the current work should prevent such discrepancies.

From the above equations, the cutoff ellipticity for harmonic with kinetic energy, U_{kin}, can be solved for as [115]:

$$\varepsilon_{cut} = \omega\tau\frac{\sqrt{\Delta p_{\perp}^2/4+1/(\tau^2\Delta p_{\perp}^2)}}{\sqrt{2U_{kin}}+\tau E\cos(\omega t_i)}. \quad (5\text{-}4)$$

This has been shown to quantitatively agree with experimental results and shows that the cutoff ellipticity will decrease as the harmonic order increases.

In addition to considering the uncertainty in the momentum perpendicular to the polarization axis, the cutoff ellipticity can be considered as a function of the initial perpendicular velocity required of each harmonic for recombination. This required velocity can be expressed as [107]:

$$\upsilon_{\perp} = \frac{-\beta F \varepsilon \lambda}{2\pi c}. \qquad (5\text{-}5)$$

In which *F* is the amplitude of the electric field, λ is the laser wavelength, and *c* is the speed of light. In this equation, β is a parameter that depends on the harmonic order and thus the trajectory of the recombining electron and is described as [107]:

$$\beta = \frac{\sin \omega t_r - \sin \omega t_i}{\omega \tau} - \cos \omega t_i . \qquad (5\text{-}6)$$

Equation (5-6) introduces a new term t_r that represents the return time of the electron. Thus by measuring the elliptical dependence of individual harmonics, it should be possible to extract information directly related to the perpendicular velocity required for recombination at any given ellipticity and the ionization and recombination times.

The parameter defined in equation (5-6) can thus be used in the equation describing the Gaussian dependence of HHG on driving field ellipticity. A more detailed version of equation (5-1) is [107]:

$$\frac{I_{\varepsilon}}{I_{\varepsilon=0}} \approx \exp\left(-\frac{\beta^2 \sqrt{2 I_p I}}{4\pi^2 c^2} \lambda^2 \varepsilon^2\right) \qquad (5\text{-}7)$$

With the exception of β, every parameter in (5-7) is a constant or measurable. This equation is thus used as a fitting function for the elliptical dependence of HHG normalized to HHG with

linear polarization and β is solved for directly for each harmonic order. An additional term is used to describe the accuracy of the fit, χ^2, which is calculated for every fit and equal to:

$$\chi^2 = \sum_i \left(\frac{y - y_i}{\sigma_i}\right)^2 \quad (5\text{-}8)$$

In which the top part of the quotient represents the difference between the fit line and the experimental data and σ is an approximated standard deviation calculated by IgorPro.

The models outlined in the above equations were developed for atomic systems. Figure 5.5 shows the application of equation (5-7) to HHG from SF_6 for three different harmonics, at a focal position of (-) 2 mm, and a laser intensity of 5.2×10^{14} W/cm^2. The annotation in each of the graphs shows the calculated β and χ^2 of the three harmonics shown. The fitting parameter increases generally with an increase in harmonic order, as can be seen from the increasing deviation of the fit (blue line) and experimental points (black circles).

The overall profile of these parameters as a function of harmonic order is shown in Figure 5.6 for three focal positions and three intensities. A feature that persists in all of the

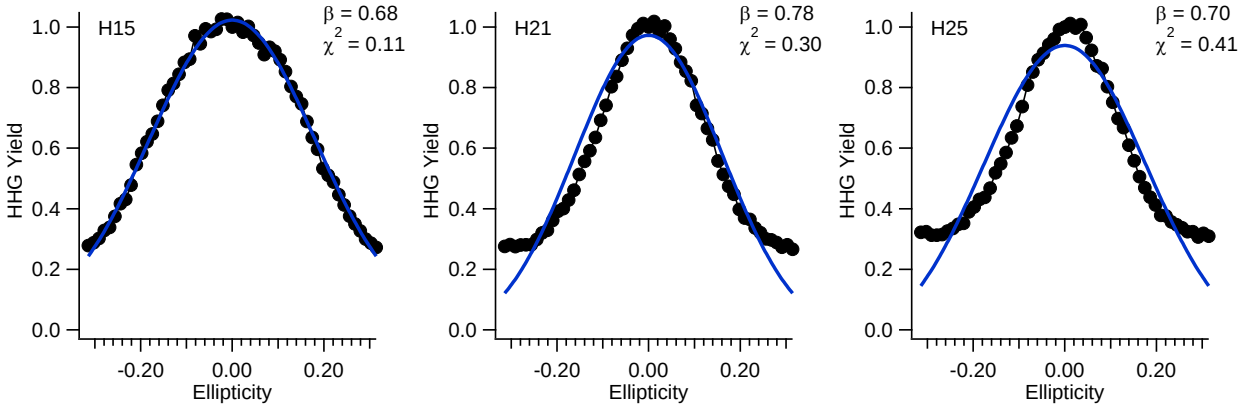

Figure 5.5: Elliptical dependence fittings for H15, H21, and H25 at (-) 2 mm and 5.2×10^{14} W/cm^2. The experimental data is show as black circles and the fits are solid blue lines.

spectra in Figure 5.6 (d-f) is the general increase of the χ^2 parameter as a function of harmonic

spectra in Figure 5.6 (d-f) is the general increase of the χ^2 parameter as a function of harmonic order. The exception to this is the lowest ordered harmonics in each spectrum. The final ellipticity probed in these experiments was not high enough to significantly hinder the recombination process for the lower ordered harmonics, resulting in a poor Gaussian fit for the HHG decay. The first harmonic that experiences a sufficient decay for a measurable Gaussian is H15, which has the lowest χ^2 value at each experimental condition. After H15, the fitting parameter jumps significantly before gradually increasing with harmonic order. This initial jump in the fitting parameter is indicative of the poor fit to the Gaussian model, likely due to the alteration of the electron trajectory associated with the resonance.

In Figure 5.6 (a-c), the calculated β parameters are presented, all of which correspond to the χ^2 plots directly below them. The first trend to note is the independence of the β parameter with respect to χ^2, indicating that the features observed in (a-c) are unique to the elliptical dependence of the probed molecule and not artifacts of the fitting procedure. There is no trend relating the relative value of the β parameter to the laser intensity. The elliptical dependence was expected to increase with an increase in laser intensity because the amplitude of the electric field is proportional to the initial kick out of the plane of the laser induced by the beam ellipticity [116]. Thus, the lack of correlation between the beam intensity and the β values suggests the trend may be due to the phase dependence of the photorecombination dynamics inherent in the HHG spectrum of SF_6.

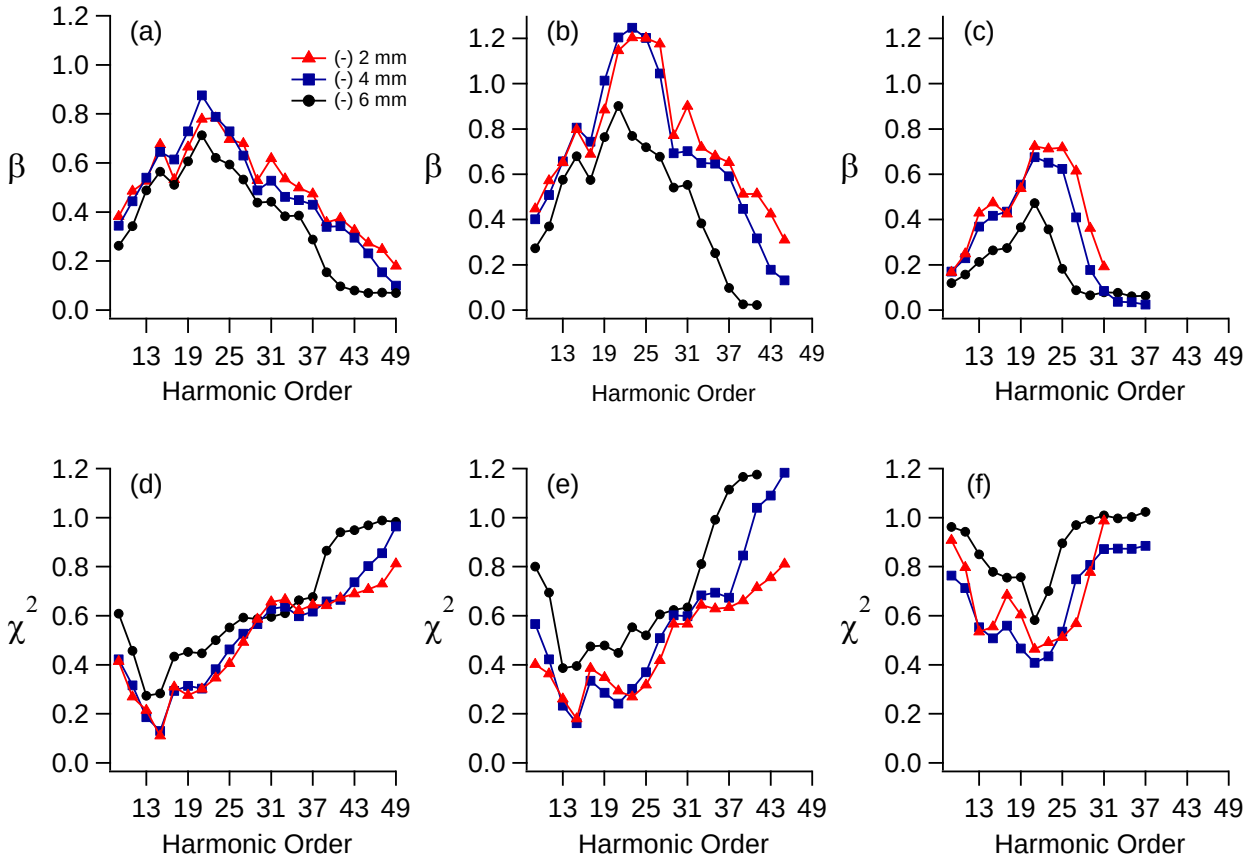

Figure 5.6: Fitting parameters (a-c) and goodness of fit coefficients (d-f) for SF_6 at three focal positions and three laser intensities. The intensities are: 5.2 (a, d) 4.0 (b, e), and 2.7 (c, f) $\times 10^{14}$ W/cm^2. χ^2 generally increases with harmonic order, showing the features observed in the fitting parameter curves are not due to fitting anomalies.

The obvious consequence to these plots is that features in the linear HHG spectrum are reproduced in the β parameter. At every combination of lens position and laser intensity, there is a deep minimum at H17, a feature that may be attributed to a shape resonance and a peak at H15, a feature confirmed as a shape resonance. At most combinations of lens position and laser intensity, there is a peak centered on H21, another feature previously attributed to a shape resonance. The presence of these dynamical processes in the β parameter is emblematic of the shape resonant process in HHG. As the wave packet returns to the parent ion, it is temporarily

trapped for a duration related to the energetic width of the resonance [59]. This trapping is independent of the ionization time, t_i, but will affect the recombination time, t_r, in equation (5-6), directly leading to the observation of the shape resonances in the β parameter.

The appearance of the shape resonances in the β parameter is further examined by calculating the ratio of H21 to H15 and the ratio of H19 and H15 to H17 to determine the relative increase in intensity and depth of the minimum, respectively. These ratios are calculated at all seven focal positions and three laser intensities and presented in Table 5.2 along with the same values taken from the HHG spectrum at the linearly polarized condition. Comparing the two values should indicate whether the shape resonant effects are more or less likely to proliferate in the extracted β parameter versus the direct HHG spectrum. For each

Table 5.2: Values of the two ratios addressed in section 4.3 of this thesis as they appear in the linearly polarized HHG data in this chapter and the calculated β parameter at 7 focal positions and 3 laser intensities.

	5.2×10^{14} W/cm^2				4.0×10^{14} W/cm^2				2.7×10^{14} W/cm^2			
	H21/H15		(H15+H19)/ H17		H21/H15		(H15+H19)/ H17		H21/H15		(H15+H19)/ H17	
Foc Pos	HHG	β	HHG	β	HHG	β	HHG	β	HHG	β	HHG	β
6	1.18	1.28	2.73	2.27	0.98	1.09	2.21	2.24	0.99	0.81	2.00	1.84
4	1.06	1.15	2.51	2.26	0.77	1.16	2.69	2.32	0.92	0.73	2.11	2.47
2	0.95	0.88	2.79	2.55	0.65	0.93	2.79	2.26	0.97	0.97	2.12	2.09
0	1.04	0.81	2.97	2.84	0.78	0.91	2.86	2.38	0.99	1.07	2.19	2.13
-2	1.46	1.15	2.67	2.52	1.37	1.43	2.95	2.44	1.56	1.53	2.32	2.38
-4	1.27	1.36	2.66	2.24	1.45	1.49	2.73	2.45	1.6	1.62	2.32	2.23
-6	1.25	1.26	2.71	2.29	1.37	1.33	2.54	2.54	1.00	1.79	2.03	2.30
avg	1.17	1.13	2.72	2.42	1.05	1.19	2.68	2.38	1.15	1.22	2.16	2.21
σ	0.17	0.21	0.14	0.22	0.34	0.23	0.25	0.11	0.30	0.42	0.13	0.21

intensity, the average ratio is calculated across all lens positions as well as the standard deviation associated with the average.

At nearly every experimental combination, the depth of the minimum at H17 is deeper in the case of linearly polarized HHG than the corresponding β parameter. For both instances, the average depth of the minimum increases with laser intensity and the standard deviation reaches a minimum at 4.0×10^{14} W/cm^2. The ratio of H21 to H15 is often higher for the β parameter than the linearly polarized HHG and is greater than 1 at lens positions the shape resonant effect is not observed in the HHG signal. These values generally decrease with an increase in laser intensity while the standard deviation follows the inverse trend. The only intensity at which the standard deviation is lower for both β ratios than the HHG ratios is 4.0×10^{14} W/cm^2. For our system, this intensity is approximately the intensity at which the HHG signal is saturated and the same intensity at which the linearly polarized HHG spectrum is most resilient to changes in the position of the focal point.

This set of data suggests there are experimental conditions at which the presence of a shape resonance is more easily observed in the extracted β parameter than the standard HHG spectrum and that the observation of the shape resonances with this method is possibly less influenced by changes in the position of the focal point than the corresponding linear HHG spectra. Beyond the consistency of the observation of the spectroscopic feature, the nature and definition of the β parameter should allow the extraction of quantitative data regarding the temporal and possibly spatial extent of the shape resonance. Further theoretical work is necessary to fully realize these possibilities.

Chapter 6: Conclusions and Outlook

This dissertation has examined the experimental conditions necessary to extract photorecombination dynamics from molecular HHG spectra and probed shape resonances to determine the effect of changes in macroscopic properties. The spatial distribution of harmonics can change drastically based on the position of the focal point with respect to the center of the gas jet. Chapter 3 showed that by using a source medium, in this instance a cw jet with a medium length an order of magnitude shorter than the Rayleigh length of the driving laser, the spatial profiles of the harmonics are more consistent over a large range of focal positions. This led to a more consistent location and appearance of the Cooper minimum in Ar than similar studies utilizing a pulsed, supersonic jet with a larger aperture. These results are more in tune with former studies using a gas cell than a pulsed gas jet and potentially show an easier method of obtaining this desired consistency in measurements.

The investigation of photorecombination dynamics was extended to observation of shape resonances in SF_6 in Chapters 4 and 5. Chapter 4 showed possible evidence of three shape resonances in the HHG spectrum of SF_6 that present as a maximum at H15, a minimum at H17, and a maximum at H21. The features were shown to be the result of photorecombination dynamics due to their independence of phase matching conditions. Each feature was attributed to a shape resonance due to presentations in the calculated harmonic spectra utilizing the QRS theory, though the minimum at H17 may be better described as a local minimum between the two maxima. The three features were shown, however, to originate from different molecular orbitals. This demonstrates the harmonic spectra from a molecule with energetically close valence orbitals can best be described as a superposition of multiple orbital contributions with

strong photorecombination dynamics from one orbital disproportionately influencing the overall harmonic signal in the energy region of the dynamical process. The shape resonances were shown to change in intensity based on the phase matching conditions utilized in the harmonic generation, a signature of the phase change inherent in the shape resonance process.

A convenient experimental knob was then used to probe the shape resonances and determine the possible influence of the photoelectron asymmetry parameter on HHG. Harmonic spectra were taken at multiple ellipticities of the driving laser and the overall change in the harmonic spectrum was recorded and then fitted to a model previously developed for atomic harmonic spectra from elliptically polarized light. The shape resonance that presents as a minimum at H17 in SF_6 was shown to broaden as the ellipticity increased, showing the effect of multiple recombination angles on the harmonic spectrum. The normalized data was used to calculate a β parameter related to the time an electron spends in the electric field and the same features observed in the harmonic spectrum from a linearly polarized driving laser are reproduced in the energy dependent β parameter. Further theoretical work is needed in order to determine if these extracted values can be used to calculate angular dependent information from the harmonic spectrum.

Future work on this project will heavily depend on the high power OPA system that has thus far been used sparingly in generating extended harmonic spectra. The applications are vast, but a simple and valuable experiment would be to reproduce the results in this dissertation at multiple, especially longer wavelengths. One hindrance in Chapter 5 of this dissertation is the lack of precision is measuring the broadening of the minimum centered on H17 in the SF_6 harmonic spectrum. One reason this lack of precision exists is the resolution of

HHG, which in the current work is limited to odd orders of the fundamental (3 eV). If the wavelength is adjusted to 2000 nm at a sufficiently high intensity, not only will the harmonic spectrum extend beyond 100 eV, the resolution will improve to 1.24 eV. This would also improve the study in Chapter 4 of this dissertation by giving us a more accurate energy range of the photorecombination dynamics.

The OPA can also be utilized in a pump-probe experiment to initiate vibrational and electronic excitations prior to the generation of a harmonic spectrum. The OPA can be tuned to selectively pump vibrational excitations in molecules that alter the behavior of photorecombination dynamics. A BBO crystal can be utilized to generate the second harmonic of the fundamental in order pump an electronically excited state in the molecule prior to harmonic generation. This would be intrinsically interesting, but would also serve to isolate the harmonic yield from the excited state as opposed to observing a superposition of harmonic contributions from lower lying molecular orbitals.

References

[1] K.J. Schafer, B. Yang, L.F. DiMauro, K.C. Kulander, Physical Review Letters 70 (1993) 1599.

[2] P.B. Corkum, Physical Review Letters 71 (1993) 1994.

[3] A.-T. Le, R.R. Lucchese, S. Tonzani, T. Morishita, C.D. Lin, Physical Review A 80 (2009) 013401.

[4] H. Niikura, D.M. Villeneuve, P.B. Corkum, Physical Review Letters 94 (2005) 083003.

[5] A. Scrinzi, M.Y. Ivanov, R. Kienberger, D.M. Villeneuve, Journal of Physics B 39 (2005) R1.

[6] L.V. Keldysh, Soviet Physics JETP 20 (1965) 1307.

[7] J.A.R. Samson, W.C. Stolte, Journal of Electron Spectroscopy and Related Phenomena 123 (2002) 265.

[8] K.C. Kulander, J. Cooper, K.J. Schafer, Physical Review A 51 (1995) 561.

[9] C. Cohen-Tannoudji, D. Guery-Odolin, Advances in Atomic Physics, World Scientific Publishing Co. Pte. Ltd., Singapore, 2011.

[10] T. Pfeifer, C. Spielmann, G. Gerber, Reports on Progress in Physics 69 (2006) 443.

[11] M. Bellini, C. Lyngå, A. Tozzi, M.B. Gaarde, T.W. Hänsch, A. L'Huillier, C.G. Wahlström, Physical Review Letters 81 (1998) 297.

[12] P. Salieres, A. L'Huillier, M. Lewenstein, Physical Review Letters 74 (1995) 3776.

[13] E. Cormier, M. Lewenstein, European Physical Journal D 12 (2000) 227.

[14] Y. Oishi, M. Kaku, A. Suda, F. Kannari, K. Midorikawa, Opt. Express 14 (2006) 7230.

[15] I.J. Kim, C.M. Kim, H.T. Kim, G.H. Lee, Y.S. Lee, J.Y. Park, D.J. Cho, C.H. Nam, Physical Review Letters 94 (2005).

[16] E. Frumker, C.T. Hebeisen, N. Kajumba, J.B. Bertrand, H.J. Woerner, M. Spanner, D.M. Villeneuve, A. Naumov, P.B. Corkum, Physical Review Letters 109 (2012).

[17] M. Lewenstein, P. Salières, A. L'Huillier, Physical Review A 52 (1995) 4747.

[18] M.V. Frolov, N.L. Manakov, T.S. Sarantseva, A.F. Starace, Physical Review A 86 (2012) 063406.

[19] P. Balcou, P. Sali`eres, A. L'Huillier, M. Lewenstein, Physical Review A 55 (1997) 3204.

[20] B.G. Mette, L.T. Jennifer, J.S. Kenneth, Journal of Physics B: Atomic, Molecular and Optical Physics 41 (2008) 132001.

[21] B. Philippe, S.D. Anne, B.G. Mette, L.H. Anne, Journal of Physics B: Atomic, Molecular and Optical Physics 32 (1999) 2973.

[22] J.P. Farrell, L.S. Spector, B.K. McFarland, P.H. Bucksbaum, M. Guhr, M.B. Gaarde, K.J. Schafer, Physical Review A 83 (2011) 023420.

[23] C. Winterfeldt, C. Spielmann, G. Gerber, Reviews of Modern Physics 80 (2008) 117.

[24] M.B. Gaarde, J.L. Tate, K.J. Shafer, Journal of Physics B 41 (2008) 132001.

[25] A.D. Shiner, B.E. Schmidt, C. Trallero-Herrero, H.J. Worner, S. Patchkovskii, P.B. Corkum, J.-C. Kieffer, F. Legare, D.M. Villeneuve, Nature Physics 7 (2011) 464.

[26] H.J. Worner, J.B. Bertrand, D.V. Kartashov, P.B. Corkum, D.M. Villeneuve, Nature 466 (2010) 604.

[27] C. Jin, J.B. Bertrand, R.R. Lucchese, H.J. Worner, P.B. Corkum, D.M. Villeneuve, A.T. Le, C.D. Lin, Physical Review A 85 (2012) 013405.

[28] M.B. Gaarde, F. Salin, E. Constant, P. Balcou, K.J. Schafer, K.C. Kulander, A. L'Huillier, Physical Review A 59 (1999) 1367.

[29] L. Lynch D, K.V. Mc, R. Lucchese R, Resonances, American Chemical Society, 1984, p. 89.

[30] D.C. Yost, T.R. Schibli, J. Ye, J.L. Tate, J. Hostetter, M.B. Gaarde, K.J. Schafer, Nature Physics 5 (2009) 815.

[31] K.C. Kulander, K.J. Schafer, J.L. Krause, International Journal of Quantum Chemistry (1991) 415.

[32] M. Lewenstein, P. Balcou, M.Y. Ivanov, A. L'Huillier, P.B. Corkum, Physical Review A 49 (1994) 2117.

[33] S. Haessler, J. Caillat, P. Salieres, Journal of Physics B 44 (2011) 203001.

[34] J.W. Cooper, Physical Review 128 (1962) 681.

[35] V. McKoy, T.A. Carlson, R.R. Lucchese, The Journal of Physical Chemistry 88 (1984) 3188.

[36] J.L. Dehmer, The Journal of Chemical Physics 56 (1972) 4496.

[37] M.N. Piancastelli, Journal of Electron Spectroscopy and Related Phenomena 100 (1999) 167.

[38] L. Dehmer J, Resonances, American Chemical Society, 1984, p. 139.

[39] R.R. Lucchese, G. Raseev, V. McKoy, Physical Review A 25 (1982) 2572.

[40] I. Markus, D. Sascha, G. Leif, S. Frank, S. Jörn, W. Peter, V. Jens, Journal of Physics B: Atomic, Molecular and Optical Physics 45 (2012) 225102.

[41] J. Cooper, R.N. Zare, in: S. Geltman, K.T. Mahanthappa, W.E. Britten (Eds.), Lectures in Theoretical Physics, Gordon and Breach, New York, 1969, p. 317.

[42] S.T. Manson, A.F. Starace, Reviews of Modern Physics 54 (1982) 389.

[43] D.M.P. Holland, M.A. MacDonald, P. Baltzer, L. Karlsson, M. Lundqvist, B. Wannberg, W.v. Niessen, Chemical Physics 192 (1995) 333.

[44] J.L. Krause, K.J. Schafer, K.C. Kulander, Physical Review Letters 68 (1992) 3535.

[45] A. McPherson, G. Gibson, H. Jara, U. Johann, T.S. Luk, I.A. McIntyre, K. Boyer, C.K. Rhodes, Journal of the Optical Society of America B 4 (1987) 595.

[46] M. Ferray, A.L. Huillier, X.F. Li, L.A. Lompre, G. Mainfray, C. Manus, Journal of Physics B: Atomic, Molecular and Optical Physics 21 (1988) L31.

[47] X. Li, A. L'Huillier, M. Ferray, L. Lompré, G. Mainfray, Physical Review A 39 (1989) 5751.

[48] N. Sarukura, K. Hata, T. Adachi, R. Nodomi, M. Watanabe, S. Watanabe, Physical Review A 43 (1991) 1669.

[49] J.K. Crane, R.W. Falcone, M.D. Perry, S. Herman, Optics Letters 17 (1992) 1256.

[50] D.S. Steingrube, T. Vockerodt, E. Schulz, U. Morgner, M. Kovačev, Physical Review A 80 (2009) 043819.

[51] K. Miyazaki, H. Sakai, Journal of Physics B: Atomic, Molecular and Optical Physics 25 (1992) L83.

[52] J. Higuet, H. Ruf, N. Thiré, R. Cireasa, E. Constant, E. Cormier, D. Descamps, E. Mével, S. Petit, B. Pons, Y. Mairesse, B. Fabre, Physical Review A 83 (2011) 053401.

[53] H.J. Worner, H. Niikura, J.B. Bertrand, P.B. Corkum, D.M. Villeneuve, Physical Review Letters 102 (2009) 103901.

[54] J.B. Bertrand, H.J. Worner, P. Hockett, D.M. Villeneuve, P.B. Corkum, Physical Review Letters 109 (2012) 143001.

[55] M.C.H. Wong, A.T. Le, A.F. Alharbi, A.E. Boguslavskiy, R.R. Lucchese, J.P. Brichta, C.D. Lin, V.R. Bhardwaj, Physical Review Letters 110 (2013).

[56] A. Rupenyan, P.M. Kraus, J. Schneider, H.J. Wörner, Physical Review A 87 (2013) 033409.

[57] X. Ren, V. Makhija, A.-T. Le, J. Troß, S. Mondal, C. Jin, V. Kumarappan, C. Trallero-Herrero, Physical Review A 88 (2013) 043421.

[58] V. Strelkov, Physical Review Letters 104 (2010) 123901.

[59] M. Tudorovskaya, M. Lein, Physical Review A 84 (2011) 013430.

[60] R. Velotta, N. Hay, M.B. Mason, M. Castillejo, J.P. Marangos, Physical Review Letters 87 (2001) 183901.

[61] R.d. Nalda, E. Heesel, M. Lein, N. Hay, R. Velotta, E. Springate, M. Castillejo, J.P. Marangos, Physical Review A 69 (2004) 031804.

[62] M. Machholm, The Journal of Chemical Physics 115 (2001) 10724.

[63] J. Itatani, D. Zeidler, J. Levesque, M. Spanner, D.M. Villeneuve, P.B. Corkum, Physical Review Letters 94 (2005) 123902.

[64] F. Rosca-Pruna, M.J.J. Vrakking, The Journal of Chemical Physics 116 (2002) 6567.

[65] W. Li, X. Zhou, R. Lock, S. Patchkovskii, A. Stolow, H.C. Kapteyn, M.M. Murnane, Science 322 (2008) 1207.

[66] M. Spanner, J. Mikosch, A.E. Boguslavkiy, M.M. Murnane, A. Stolow, S. Patchkovskii, Physical Review A 85 (2012) 033426.

[67] A. Ferré, D. Staedter, F. Burgy, M. Dagan, D. Descamps, N. Dudovich, S. Petit, H. Soifer, V. Blanchet, Y. Mairesse, Journal of Physics B: Atomic, Molecular and Optical Physics 47 (2014) 124023.

[68] N.L. Wagner, A. Wuest, I.P. Christov, T. Popmintchev, X. Zhou, M.M. Murnane, H.C. Kapteyn, PNAS 103 (2006) 13279.

[69] H.J. Worner, J.N. Bertrand, B. Fabre, J. Higuet, H. Ruf, A. Dubrouil, S. Patchkovskii, M. Spanner, Y. Mairesse, V. Blanchet, E. Mevel, E. Constant, P.B. Corkum, D.M. Villeneuve, Science 334 (2011) 208.

[70] R. Torres, N. Kajumba, J.G. Underwood, J.S. Robinson, S. Baker, J.W.G. Tisch, R.d. Nalda, W.A. Bryan, R. Velotta, C. Altucci, I.C.E. Turcu, J.P. Marangos, Physical Review Letters 98 (2007) 203007.

[71] M. Lein, Journal of Physics B 40 (2007) R135.

[72] J. Itatani, J. Levesque, D. Zeidler, H. Niikura, H. Pepin, J.C. Kieffer, P.B. Corkum, D.M. Villeneuve, Nature 432 (2004) 867.

[73] Z. Chang, C. Li, E. Moon, Method and apparatus for controlling carrier envelope phase in U.S.P. Office (Ed.). Kansas State University Research Foundation, United States, 2008.

[74] G. Cerullo, S. De Silvestri, Review of Scientific Instruments 74 (2003) 1.

[75] M. Young, Optics and Laser, Springer-Verlag, New York, 1977.

[76] D. Irimia, D. Dobrikov, R. Kortekaas, H. Voet, D.A. van den Ende, W.A. Groen, M.H.M. Janssen, Review of Scientific Instruments 80 (2009).

[77] U. Even, J. Jortner, D. Noy, N. Lavie, C. Cossart-Magos, Journal of Chemical Physics 112 (2000).

[78] Atomic and Molecular Beam Methods, Oxford University Press, New York, 1988.

[79] J. Ladislas Wiza, Nuclear Instruments and Methods 162 587.

[80] W.W. Piper, Phosphor Screen in U.S.P. Office (Ed.). General Electric, United States, 1955.

[81] S.Baker, J.S. Robinson, C.A. Haworth, H. Teng, R.A. Smith, C.C. Chirila, M. Lein, J.W.G. Tisch, J.P. Marangos, Science 312 (2006) 424.

[82] P. Salieres, T. Ditmire, M.D. Perry, A.L. Huillier, M. Lewenstein, Journal of Physics B: Atomic, Molecular and Optical Physics 29 (1996) 4771.

[83] C. Lyngå, M.B. Gaarde, C. Delfin, M. Bellini, T.W. Hänsch, A. L' Huillier, C.G. Wahlström, Physical Review A 60 (1999) 4823.

[84] E. Brunetti, R. Issac, D.A. Jaroszynski, Physical Review A 77 (2008) 023422.

[85] H. Xu, H. Xiong, Z. Zeng, Y. Fu, J. Yao, R. Li, Y. Cheng, Z. Xu, Physical Review A 78 (2008) 033841.

[86] X. He, M. Miranda, J. Schwenke, O. Guilbaud, T. Ruchon, C. Heyl, E. Georgadiou, R. Rakowski, A. Persson, M.B. Gaarde, A. L'Huillier, Physical Review A 79 (2009) 063829.

[87] H.J. Wörner, H. Niikura, J.B. Bertrand, P.B. Corkum, D.M. Villeneuve, Physical Review Letters 102 (2009) 103901.

[88] K. Ba Dinh, H. Vu Le, P. Hannaford, L. Van Dao, Journal of Applied Physics 115 (2014).

[89] M.V. Frolov, N.L. Manakov, T.S. Sarantseva, M.Y. Emelin, M.Y. Ryabikin, A.F. Starace, Physical Review Letters 102 (2009) 243901.

[90] B.A. Sickmiller, R.R. Jones, Physical Review A 80 (2009) 031802.

[91] T. Gustafsson, Physical Review A 18 (1978) 1481.

[92] J.L. Dehmer, A.C. Parr, S. Wallace, D. Dill, Physical Review A 26 (1982) 3283.

[93] B.M. Addison-Jones, K.H. Tan, B.W. Yates, J.N. Cutler, G.M. Bancroft, J.S. Tse, Journal of Electron Spectroscopy and Related Phenomena 48 (1989) 155.

[94] A.J. Yencha, D.B. Thompson, A.J. Cormack, D.R. Cooper, M. Zubek, P. Bolognesi, G.C. King, Chemical Physics 216 (1997) 227.

[95] L. Yang, H. Agrena, V. Carravettab, O. Vahtras, L. Karlsson, B. Wannberg, D.M.P. Holland, M.A. MacDonald, Journal of Electron Spectroscopy and Related Phenomena 94 (1998) 163.

[96] A.P.P. Natalense, R.R. Lucchese, Journal of Chemical Physics 111 (1999) 5344.

[97] M. Stener, D. Toffoli, G. Fronzoni, P. Decleva, Journal of Chemical Physics 124 (2006).

[98] J. Jose, R.R. Lucchese, T.N. Rescigno, Journal of Chemical Physics 140 (2014) 204305.

[99] A.-T. Le, R.R. Lucchese, C.D. Lin, Physical Review A 87 (2013) 063406.

[100] A.-T. Le, R.R. Lucchese, C.D. Lin, Physical Review A 88 (2013) 021402.

[101] A. Rupenyan, J.B. Bertrand, D.M. Villeneuve, H.J. Wörner, Physical Review Letters 108 (2012) 033903.

[102] A. Ferré, A.E. Boguslavskiy, M. Dagan, V. Blanchet, B.D. Bruner, F. Burgy, A. Camper, D. Descamps, B. Fabre, N. Fedorov, J. Gaudin, G. Geoffroy, J. Mikosch, S. Patchkovskii, S. Petit, T. Ruchon, H. Soifer, D. Staedter, I. Wilkinson, A. Stolow, N. Dudovich, Y. Mairesse, Nat Commun 6 (2015).

[103] W. Becker, S. Long, J.K. McIver, Physical Review A 50 (1994) 1540.

[104] P.B. Corkum, N.H. Burnett, M.Y. Ivanov, Optics Letters 19 (1994) 1870.

[105] P. Antoine, A. L'Huillier, M. Lewenstein, P. Salières, B. Carré, Physical Review A 53 (1996) 1725.

[106] M.Y. Ivanov, T. Brabec, N. Burnett, Physical Review A 54 (1996) 742.

[107] M. Moller, Y. Cheng, S.D. Khan, B. Zhao, K. Zhao, M. Chini, G.G. Paulus, Z. Chang, Physical Review A 86 (2012) 011401.

[108] F. He, C. Ruiz, A. Becker, Optics Letters 32 (2007) 3224.

[109] G. Sansone, Physical Review A 79 (2009) 053410.

[110] V.V. Strelkov, A.A. Gonoskov, I.A. Gonoskov, M.Y. Ryabikin, Physical Review Letters 107 (2011) 043902.

[111] Y. Li, X. Zhu, Q. Zhang, M. Qin, P. Lu, Opt. Express 21 (2013) 4896.

[112] W. Becker, A. Lohr, M. Kleber, M. Lewenstein, Physical Review A 56 (1997) 645.

[113] D. Shafir, B. Fabre, J. Higuet, H. Soifer, M. Dagan, D. Descamps, E. Mével, S. Petit, H.J. Wörner, B. Pons, N. Dudovich, Y. Mairesse, Physical Review Letters 108 (2012) 203001.

[114] K.-J. Yuan, A.D. Bandrauk, Physical Review Letters 110 (2013) 023003.

[115] V.V. Strelkov, M.A. Khokhlova, A.A. Gonoskov, I.A. Gonoskov, M.Y. Ryabikin, Physical Review A 86 (2012) 013404.

[116] H. Xu, H. Xiong, B. Zeng, W. Chu, Y. Fu, J. Yao, J. Chen, X. Liu, Y. Cheng, Z. Xu, Optics Letters 35 (2010) 472.

Vita

Benjamin Parker Wilson was born in Dallas, TX in 1986. He grew up in Indianapolis, IN and Weatherford, TX before graduating from James Martin High School in Arlington, TX in 2004. He earned his B.S. in Chemistry from Abilene Christian University in 2008. He enjoys cycling, running, and theology. In May of 2008, he will receive the degree of Doctor of Philosophy.